DESIGN AND DEVELOPMENT OF AN ENDOSCOPIC OPTICAL COHERENCE TOMOGRAPHY (OCT) IMAGING SYSTEM

Carlos Reyes

117227481

Thesis submitted for the degree of
Doctor of Philosophy

University College Cork

College of Science, Engineering and Food Science
Tyndall National Institute

June 2021

Supervisor: Brendan Roycroft

Supervisor: Brian Corbett
Head of the Department: Dr Fatima Gunning

Declaration

I, Carlos Reyes, certify that this work is my own and has not been submitted for another degree, either at University College Cork or elsewhere. All external references and sources are clearly acknowledged and identified within the contents. I haven read and understood the regulations of University College Cork concerning plagiarism.

Dated: June 2021

Carlos Reyes: _____

Table of Contents

List of Figures

List of Tables

Abstract

Optical coherence tomography (OCT) has been established as a noninvasive medical optical imaging modality that is capable of generating cross sectional images with a high axial resolution (1-10 μm) and a penetration depth of 2 mm in tissue. OCT imaging can be combined with conventional white-light endoscopes through an imaging probe capable of providing micro structural information of tissue samples based on backscattered light. This allows the study in internal hollow organs including the gastrointestinal (GI) tract.

In this thesis a novel swept-source OCT endoscopy using a fibre-cantilever piezotube (PZT) scanner has been developed with a linear field-of-view of 0.5 mm and axial resolution of 10 μm at 1300 nm. The achieved A-scan rate is 200 kHz as defined by the swept source, and a B-scan rate of 1.4 kHz given by the fibre resonance frequency. The tradeoff between faster scanning speed and fewer A-scans/B-scan was compensated by an interleaving algorithm where three consecutive B-scans are acquired and then interleaved, increasing the sampling density hence improving image quality. This process emulates a resonance frequency of 460 Hz without having to add extra-weight to the fibre.

The imaging probe can be integrated into the working channel of a commercial endoscope and has a diameter $\varnothing$ = 2.5 mm, rigid length of 25 mm and a total length of 2.2 meter to allow mobility for in-vivo imaging. OCT images of ex-vivo rat colon samples and human finger are presented. The main target users of the developed endoscope OCT probe are gastroenterologists since the presented OCT system provides value in cancer tissue analysis for applications where imaging of ex-vivo resected tissue samples is required to provide immediate structural diagnosis and can be made compatible with in-vivo measurement.

Finally, this thesis presents a new heterodyne method to characterize akinetic all-semiconductor sampled-grating distributed Bragg reflector lasers that can be the core of a swept source. This method provides opto-electronic characterization in the form of DC and AC tuning maps that represents the current combinations needed to obtain the desired linear tuning profile as needed by swept-source applications.

Acronyms and symbols

Acronyms

AC-RMS Alternate Current Root Mean Square

APC Angle Polished Connector

AC Alternating Current

BM Back Mirror

CRC Colorectal Cancer

CT Computed Tomography

DAQ Data Acquisition

DBR Distributed Bragg Reflector

DC Direct Current

DCFC Double-Clad Fibre

DCFC Double-Clad Fibre Coupler

ECL External Cavity Laser

FDML Fourier Domain Mode-Locked Laser

FD-OCT Fourier Domain Optical Coherence Tomography

FFT Fast Fourier Transform

FM Front Mirror

FOV Field of View

FSR Free Spectral Range

FWHM Full Width Half Maximum

GI Gastrointestinal

GIN Gastrointestinal Intraepithelial Neoplasia

GRIN Gradient-index Optics

MEMS Micro Electronic Mechanical System

MPT Multi-Photon Tomography

MRI Magnetic Resonance Imaging

MZI Mach-Zehnder Interferometer

NA Numerical Aperture

OCT Optical Coherence Tomography

OD Outer Diameter

OF Optical Fibre

OPD Optical Path Difference

OSA Optical Spectrum Analyzer

PBS Phosphate Buffered Saline

PC Polarization Controller

PCB Printed Circuit Board

PCLI Partially Coherent Light Interferometry

PD Photodetector

PET Positron Emission Tomography

PMT Photomultiplier Tube

PSF Point Spread Function

PZT Piezo-tubular

RIN Relative Intensity Noise

SD-OCT Spectral Domain Optical Coherence Tomography

SG-DBR Sampled Grating Distributed Bragg Reflector

SMF Single Mode Fibre

SMSR Side-Mode Supression Ratio

SNR Signal-to-Noise Ratio

SOA Semiconductor Optical Amplifier

SPS Samples per Second

SS-OCT Swept Source Optical Coherence Tomography

TD-OCT Time Domain Optical Coherence Tomography

TEC Thermo Electric Controller

TLS Tunable Laser Source

VCSEL Vertical Cavity Surface Emmiting Laser

WDM Wavelength Division Multiplexing

Symbols

$\lambda_\mathbf{c}$ - Central wavelength

$\mathbf{\Delta}\lambda$ - Sweep Range

$\mathbf{f}$ - Sweep Repetition Rate

Δz - Axial Resolution

Δx - Lateral Resolution

b - Depth of Focus

z_{max} - Maximum Imaging Depth

$\delta\lambda$ - Instantaneous Linewidth

l_c - Coherence Length

n - Refractive Index

n_g - Group Index

Δt - Detector's Sampling Time

$k = 2\pi/\lambda$ - Wavenumber/Spatial Frequency

ω - Temporal Frequency

δk - Narrow Optical Bandwidth

α - Reflection Coefficient

E - Electric Field

I_D - Photocurrent

ρ - Responsivity of Photodetector

r_s - Electric Field Reflectivity

R_s - Power Reflectivity

Σ - Sensitivity

σ^2_{noise} - Noise Variance

σ^2_{shot} - Shot Noise

ν - Optical Frequency

E_ν - Photon Energy

l_{range} - Linear Scanning Range

Publications

Journal Papers - In Preparation

- **C. Reyes**, B. Corbett, S. Butler, D. Alfieri, M. Marchetti, R. Cicchi, J. Bote, J. F. Ortega, B. Glover, B. Roycroft, ”Forward scanning optical coherence tomography probe for clinical endoscopy” Submitted to IEEE Photonics Journal (2021)

Conference Talks

- **C. Reyes**, B. Corbett, B. Roycroft ”Linear sweep of telecoms lasers for optical coherence tomography (OCT) applications”, presented at Photonics Ireland, Cork, Ireland, September 2018.

- **C. Reyes**, T. Piwonski, B. Corbett, B. Roycroft, ”Automated heterodyne method to characterize semiconductor based akinetic swept lasers”, presented at the European Conference on Biomedical Optics, Munich, Germany, session A0CTT, 23rd-25th June 2019.

- **C. Reyes**, B. Corbett, B. Roycroft, ”Endoscopic optical coherence tomography imaging system”, to be presented at Photonics Ireland 2021, Virtual Conference, 14th-16th June 2019.

Conference Posters

- **C. Reyes**, B. Corbett, B. Roycroft, ”Large lateral scanning range fiber-based swept-source optical coherence tomography system”, Biophotonics Congress: Biomedical Optics 2020, Virtual Conference, session Optical Tomography and Spectroscopy, 20th-23rd April 2020.

- **C. Reyes**, B. Corbett, B. Roycroft, ”Colorectal neoplastic polyps imaged by fibre-based optical coherence tomography”, to be presented at the European Conference on Biomedical Optics, Munich, Germany, Virtual Conference, 20th-24th June 2021.

Acknowledgements

Jesus spoke: *"I am the light of the world. Whoever follows me will not walk in darkness, but will have the light of life" - John 8:12* . These last four years have been a great journey exploring the amazing world of photonics. As I discover more from the light, I've come to realize that Jesus is the light that enlightens my life. Thank you Jesus for being the light of my life.

First and foremost, I would like to express my sincerest gratitude to my supervisors Brendan Roycroft and Brian Corbett. Brendan, thank you for your guidance, patience and encouragement, you've been a very good friend for me. Brian, thank you for teaching how to work with discipline, dedication and persistence, you are a great example to all young researchers. I will always be grateful to both of you for giving me the opportunity to come to Ireland and for your support throughout my PhD.

To my family, thank you for your love, encouragement and support. To my mom, Liz, thank you for all your kind words and teaching me to trust God above everything, may God cover you with His love. To my dad, Salomón, thank you for loving me and being there always to provide for our family, I thank God for your life. To my brother, Alberto, thank you for being the best brother, always supportive and taking good care of me. I could have never accomplished this PhD without all your support and love.

To the Gason family. Thank you Alex for welcoming me into your family giving me sense of belonging. Linda, thanks for all your advice and support all this time. Liana, you are great source of joy and encouragement to me. Joshua, you are my best little buddy and have been always been a great support to me. To the White family. Matthew, you are my best friend and you have always been there for me. Jackie, thank you for encouragement and support. You've both been a huge source of joy to me. To my friend Krystell, thank you for you being a supportive friend to me. May God bless you all.

To my colleagues who helped me along this journey. Tomasz, Sharon, Abdulaziz, Michael and Rory. I've enjoyed learning a lot from all of you. A special thanks to Myriam from the canteen, your sarcasm is very much appreciated. Finally, I would like to thank the European Union's Horizon2020 PICCOLO project and IPIC center for funding this research.

Chapter 1

Introduction

Optical coherence tomography (OCT) is a non-invasive, high-resolution (1-10 μm) medical optical imaging technology capable of providing cross-sectional and three-dimensional images to visualize the structure of biological samples as well as internal body organs with a penetration depth of 1-2 mm[1]. OCT fills a gap between confocal microscopy and ultrasound in terms of sample penetration with a high resolution (Fig. 1.1), opening new diagnosis and research opportunities for clinicians and researchers.

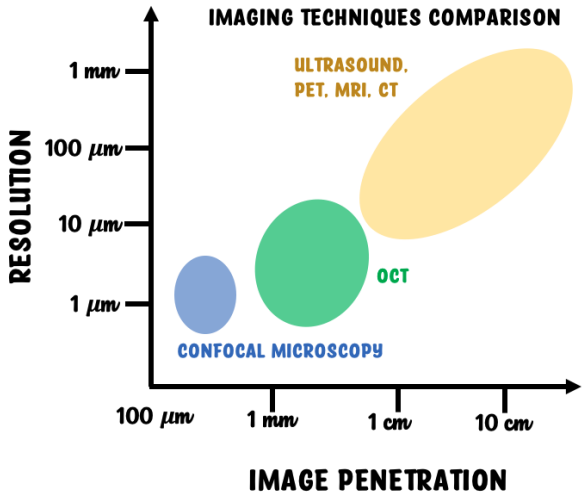

Figure 1.1: Confocal microscopy achieves sub-μm resolution but its penetration is limited. Ultrasound has a much deeper penetration, but with a reduced resolution. OCT fills the gap by providing an axial resolution between 1-15 μm and deeper penetration than confocal microscopy. Redrawn from [1].

1.1 Optical coherence tomography as a medical imaging modality

OCT has become one of the most important imaging and diagnostic tools in areas like ophthalmology [2, 3], cardiology[4, 5], dermatology[6, 7], intraoperative[8], oncology[9] and endoscopic applications[10, 11] such as gastroenterology[12, 13] and urologic oncology[14]. Gastroenterology includes OCT research tools to image the gastrointestinal (GI) tract covering the esophagus, stomach, small intestine and colon while urologic oncology includes research on the bladder, upper urinary tract, kidney and prostate.

One of the main advantages of OCT as an imaging modality is its capability of performing an in-vivo 'optical biopsy' to visualize subsurface image data representing internal microstructures as well as different pathologies without the need of tissue removal or external agents[15]. OCT creates image contrast by collecting backscattered light from different tissue structures with different optical properties and tissue boundaries providing sub-layer image information.

This feature allows OCT to be applied in cases where excisional biopsy can be a risk for a patient[16], to reduce the sampling error by guiding excisional biopsies[1] and for guidance of surgical procedures[17]. However, one of the limitations of OCT its the imaging depth of ≈ 2 mm in most tissues due to light that is highly scattered as well as light attenuation. A solution for this is to integrate the OCT imaging with medical imaging devices such as commercial endoscopes by using fibre-based imagined probes that allow access to internal organs, e.g., the GI tract. This particular field is known as OCT endoscopy.

1.2 OCT systems

OCT has evolved from Time Domain (TD-OCT)[18] to Fourier Domain OCT (FD-OCT) techniques: Spectral Domain OCT (SD-OCT) [19, 20, 21] and Swept Source OCT (SS-OCT) [22, 23, 24, 25]. Both SD-OCT and SS-OCT obtain depth profiles (A-scans) by Fourier transforming a wavelength dependent reflectivity profile, however the profile is obtained in different ways. SD-OCT uses a broadband light source with short coherence length and a spectrometer with a camera, where the main speed limitation is the readout time

of the camera. SS-OCT compensates this limitation by using a swept source that is able to rapidly tune/sweep individual narrow wavelengths with long coherence length over a large wavelength range and using a single balanced photodetector on the receive side [26]. A further advantage of SS-OCT is that the instantaneous output power per wavelength has small variations over the wavelength sweep range. In addition to the power, wavelength-tuning speed, tuning range, linewidth and single-mode operation are critical factors in SS-OCT. The different OCT types are shown in Fig. 1.2.

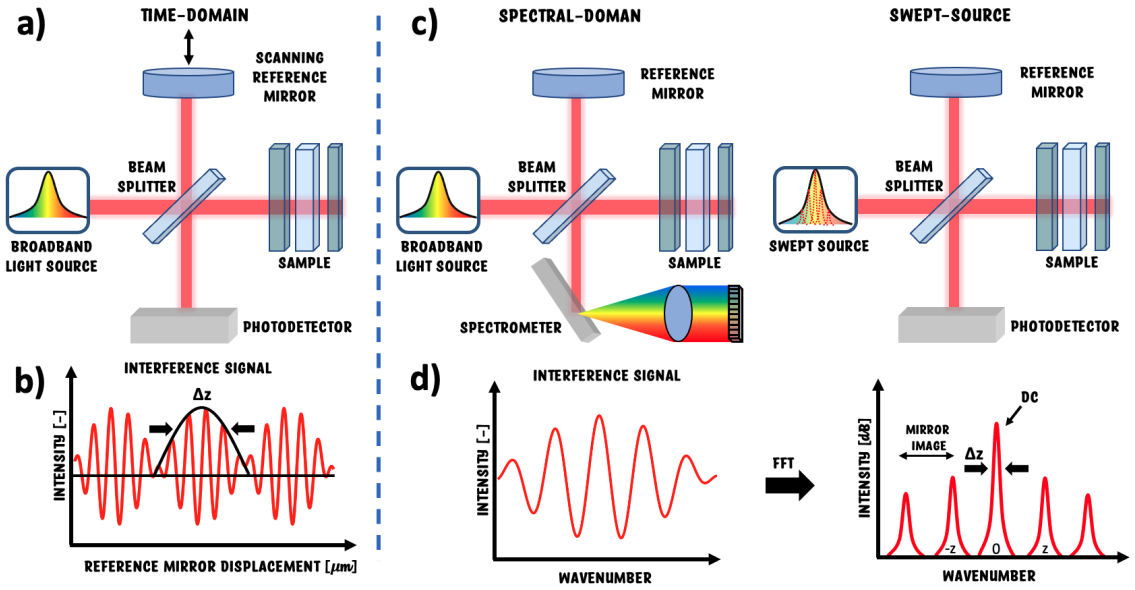

Figure 1.2: Different OCT types and respective measurements. a) Time-domain OCT setup. b) Interference signal measured by a TD-OCT system. c) Spectrometer and swept-source OCT systems. d) Measured interference signal and corresponding Fourier transform to obtain a depth profile.

FD-OCT systems measure an interference pattern that is then Fourier transformed to obtain reflectivity depth profiles. This is the basic building block of OCT known as A-scan, which represents an axial measurement of the optical backscattering properties of a sample. Cross-sectional images are created by stacking consecutive A-scans next to one another, this is defined as a B-scan and can be acquired by transverse scanning of the optical beam across the sample. These cross-sectional images are visualized in a gray scale and different internal structures can be observed as shown in Fig. 1.3.

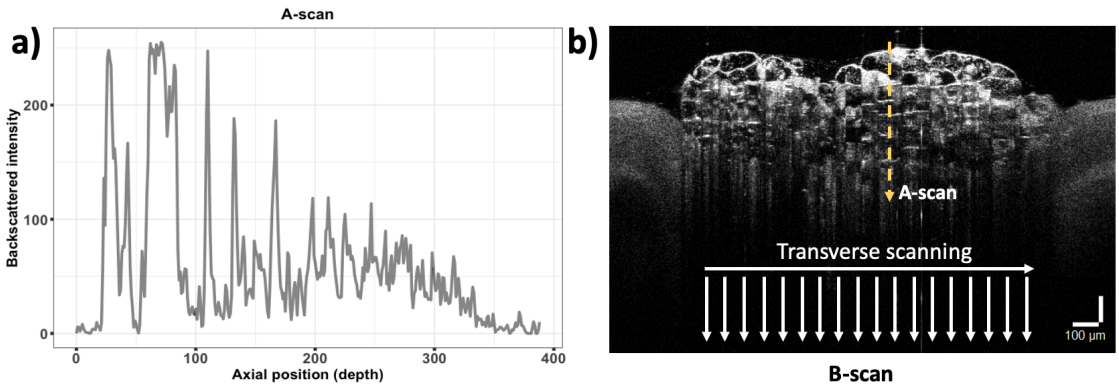

Figure 1.3: a) Axial scan representing a depth profile defined as A-scan. b) Cross-sectional image formed by stacking consecutive A-scans seen as a gray scale image

1.3 Need for OCT endoscopy

One research priority within conventional endoscopy is the prevention of colorectal cancer (CRC), which is the third most common cause of cancer death, and about 10% of all cancer cases[27, 28, 29]. Early and accurate diagnosis and precise intervention can increase cure rate[30, 31]. Hence, improved diagnostic techniques with superior sensitivity and specificity are required to allow in situ assessment, safe characterization and resection of lesions during interventions.

The vast majority of CRC arises from adenomatous polyps, premalignant lesions which develop over a period of years. The gold standard for the clinical identification of polyps is by colonoscopy, an endoscopic examination with direct visualization of the colonic mucosal surface[32] (Fig. 1.4). During this examination, detected polyps can be removed by endoscopic polypectomy for further histological assessment, preventing further development to cancer, however such a process is invasive. Conventional endoscopy does not provide sufficient image data[11] of small polyps ($<$5 mm) hence there is a miss rate between 15% and 26%[33, 34, 35]. Furthermore, flat polyps are easily missed and additionally the images do not provide sub-layer information. OCT endoscopy is a solution for this by producing images of tissue below the visible surface with micron resolution, and that can be combined with conventional endoscopic procedures.

Hence there is currently an unmet need for a technique that could produce images

of tissue below the visible surface with a micron resolution, either at the point of endoscopy prior to polypectomy or immediately after. It is proposed that such a technique could allow rapid diagnosis without the need for microscopic examination. This may reduce healthcare costs[36], reduce diagnosis time, patient anxiety and could prevent harm from unnecessary polypectomy, such as bleeding and perforation[37]. This is where OCT-endoscopy provides an 'optical biopsy' of lesions including subsurface polyp image information regarding structural information of mucosal layers with micron resolution and optical backscattering properties of tissue. This subsurface structural data may guide clinicians to detect more accurately small and flat polyps when combined with the standard endoscopic procedure. Furthermore, endoscopic OCT imaging is a valuable tool for gastroenterologists, with one major goal being the guidance of excisional biopsy to reduce sampling error and false negative rates associated with the procedure.

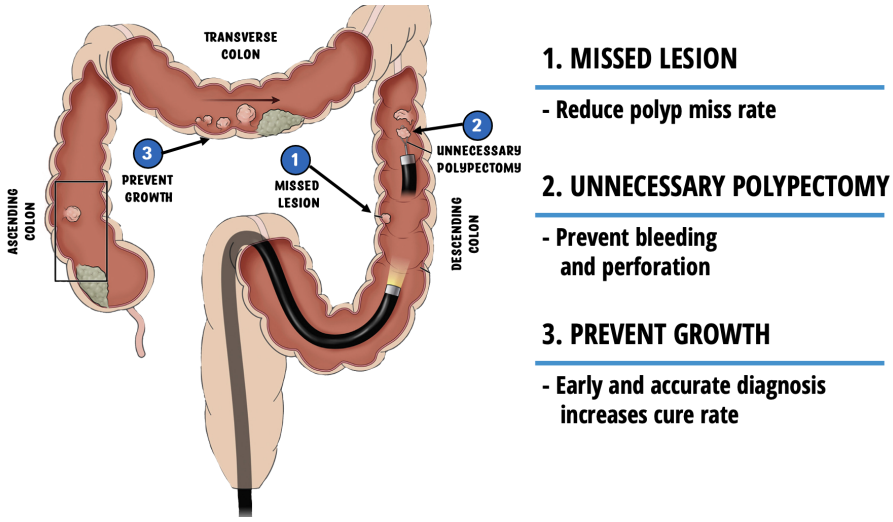

Figure 1.4: Endoscopic procedure. 1) Conventional endoscopy can miss small polyps (< 5 mm) and flat polyps. 2) Unnecessary polypectomy can cause bleeding and perforation. 3) Early diagnosis increases cure rate. Image taken from [38].

1.4 OCT endoscopy imaging probes

An OCT endoscope is a critical component for enabling OCT imaging of internal organs. Its basic function is to deliver and focus a light beam into the tissue sample, scan the beam, collect the backscattered light and transmit it to the OCT interferometer. This probe can then be inserted inside the working channel of an endoscope to enable cross-sectional imaging depth-resolved images of tissue structure. For this purpose, endoscopic devices have been assembled using forward- and side-viewing scanning mechanisms as shown in Fig. 1.5.

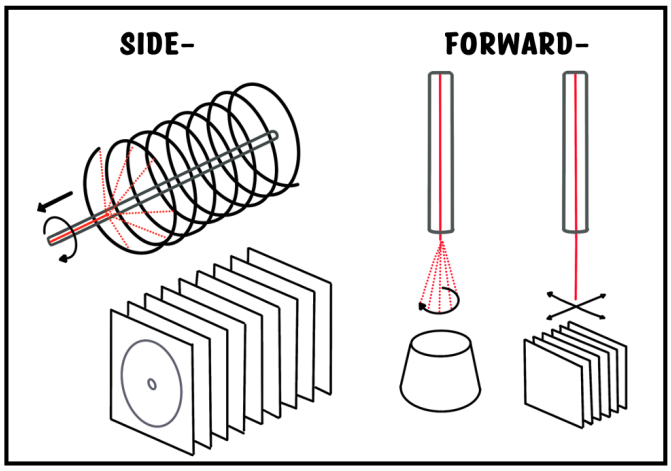

Figure 1.5: Comparison between side- and forward- scanning probes. Side-viewing probes rotates the light beam perpendicularly to the longitudinal axis. Forward-viewing probes scan the light beam parallel to the longitudinal axis of the probe. Image redrawn from [13].

Side-viewing endoscope probes are designed to image areas of luminal organs with tubular structures[39, 40, 41]. For these probes, the direction of the imaging beam is perpendicular with respect to the longitudinal axis of the probe accomplished by using optics like glass rods, GRIN lenses and beam reflectors to deflect the beam. To accomplish this, optical rotary junctions are required as well as driveshafts to translate the probe along the axis while rotating at the same time. Side-viewing endoscopes are divided into proximal-[42, 43, 44, 45] and distal-[46, 47, 48, 49] end probes depending on the location of the beam scanning device. Proximal-end devices use a fiber-optic rotary joint to couple light from

a stationary source fiber to the rotating endoscope. In the case of distal-end, a micro-reflector deflects and scans the imaging beam obtaining a higher imaging speed.

Forward-viewing endoscope probes are required for cases where the tissue is located in front of the probe as well as for image guidance of biopsies and device placement where larger space between the OCT probe and sample surface is required, e.g., hollow organ imaging including the colon, bladder and stomach. Compared to side probes, forward probes eliminate the need of mechanically actuating either the rotational fibre optic-coupler or the entire endoscope head. For this reason, distal probes are more complex to assemble since the scanning device is placed at the distance end limiting the dimensions of the scanner and imaging optics.

Several scanning methods including MEMS scanners and piezo-tubular (PZT) scanners have been proposed. MEMS scanners[50, 51, 52] generate a stable scanning pattern in the order of few kHz range, however a folded path to guide the beam is needed so a larger probe diameter in the range of 4-5.8 mm is required, hence its integration into an endoscope is more complex[11]. PZT scanners induce a resonant scanning mode of a fibre-optic cantilever when the PZT actuator is driven at the mechanical resonant frequency of the cantilever. Scanning speeds in the range of few kHz can be obtained. Table 1.1 presents a summary of the PZT forward- probes presented in the literature.

The design of an endoscopic OCT imaging probe is defined by the mechanical and optical parameters from Table 1.1. The mechanical parameters determine the dimensions of the probe and are crucial if the probe is to be integrated into the working channel of a conventional endoscope. These include the outer diameter (OD), limited to the minimum diameter of the imaging lens and the mechanical housing, and the rigid length which is the required length by the PZT and the optical lens. A shorter rigid length is desired for easy access to internal organs with specific curvatures.

The optical parameters include the imaging lens and the performance of the swept source. The axial and lateral resolutions Δz, Δx are decoupled from each other, the axial resolution Δz is defined by the centre wavelength λ_c and sweep range $\Delta\lambda$ of the swept source while the lateral resolution Δx is defined by centre wavelength λ_c and the NA of the lens (Sect. 3.1.4). The image depth is a combination between the confocal parameter of the lens, defined by its numerical aperture (NA), the sweep repetition rate of the swept

Table 1.1: Comparison of forward scanning probes. OD: Outer diameter; f_{res}: Fibre resonant frequency; FOV: field-of-view; Δz: Axial resolution; Δx: Lateral resolution; λ_c: Centre wavelength; $\Delta\lambda$: Sweep range

Type	**OD/ rigid length (mm)**	f_{res}	**FOV/ image depth (mm)**	$\Delta z/$ Δx μm	$\lambda_c/\Delta\lambda(nm)$	**A-scan rate**	**B-scan rate**
PZT SD-OCT [53]	2.4 / 32	1.4 kHz	2.5 lateral scanning/ 1.3	25 / 16	1290 / 31	-	6 frames/s (1.3 mm depth)
PZT SS-OCT [54]	2.4 / -	62.5 Hz	Circular diameter of 2/ 1.78	9.7 / 13	1310 / 100	40 kHz	62.5 frames/s 652 x 2048 pixels (1.78 mm depth)
PZT SD-OCT [55]	3.2 / 31	63 Hz	Circular diameter of 2.2 / 2.1	11.2 / 18	1310	47 kHz	-
PZT SS-OCT [56]	3.2 / 25	338 Hz	Circular diameter of 1.2 / 2.5	8 / 6	1315 / 95	240 kHz	1 frame/s 338 cycles/ frame 710 A-scans/ cycle (2.5 mm depth)
PZT SS-OCT [57]	1.07 / 24.6	200 Hz	Circular diameter of 1.1 expandable to 19 x 10.4 through mosaicking / 0.7	8.9 / 10	1060	100 kHz	1400 concentric circles
PZT SS-OCT [58]	3.3 / 20	1.8 kHz	Circular diameter of 0.9 / -	9 / 5	1310	1 MHz	1800 Hz Circular scan
PZT SS-OCT [59]	2.5 / 15	-	Circular diameter of 1.65 / 1.5	24 / 43	1340 / 32	142 kHz	Spiral
PZT SS-OCT [60]	4 / 11.3		Circular diameter of 1.3 / -	12 / -	1300 / 90	174 kHz	Spiral 360 Hz
PZT SS-OCT Presented probe	**2.5 / 25**	**1.4 kHz**	**Linear scanning of 1/1**	**10/22**	**1300 / 80**	**200 kHz**	460 Hz

source, the coherence length and the number of sampling points per A-scan (Sect. 3.1.5). The magnification of the imaging lens defines the field-of-view (FOV) along with the resonance movement of the optical fibre (Sect. 3.3.2). The combination of all these parameters determines the ultimate performance of the imaging probe in terms of mechanical scanning range and speed, B-scan rate and axial and lateral resolutions. Trade-offs have to be considered when designing the probe in order to integrate it into an endoscope.

The design, assembly and integration of the OCT endoscopic imaging probe has been a complex procedure requiring knowledge of several technical disciplines including mechanics, optics and electronics. To accomplish this, the probe design was broken into individual design blocks and were then put together. One design block was the optomechanical placement of the optical elements which required precise alignment to avoid damaging the optics. The second block was optimization of the OCT system to acquire A-scans. These blocks were then integrated together through precise electronic synchronization that would allow the acquisition of OCT B-scans.

1.5 Thesis structure and original contributions

This thesis has the following chapter structure:

1. **Chapter 2 - Swept sources**
   The first half of this chapter presents a **review of the background material** by defining what a swept source is in terms of central wavelength, wavelength range, sweep frequency and optical power. The swept source is the key element to accomplish the required imaging speed as well as a micron axial image resolution (Sect. 2.1 - Sect. 2.3).

   The second half of the chapter presents the **original contributions to the field of akinetic swept sources**. These include a heterodyne DC/AC measurement setup (Sect. 2.4.3 and Sect. 2.4.4), characterization of telecoms lasers as swept sources including multi-section slotted lasers processed in-house (Sect. 2.4.5 and Sect. 2.4.6) and commercial tunable telecoms sampled grating distributed bragg reflectors (SG-DBR) lasers (Sect. 2.4.7 and Sect. 2.4.8) and finally wavelength tuning dictionaries to obtain a linear sweep needed for swept sources are obtained (Sect. 2.5).

2. **Chapter 3 - Optical Coherence Tomography**
   The opening section of this chapter (Sect. 3.1) presents the **review of the background material** by defining the mathematical and physical concepts of light interferometry, which is the base to acquire OCT images. Theoretical definitions of interference pattern and its Fourier transform are given to define the basic building block of OCT which is an A-scan.

   The following sections of the chapter present the **original contributions to the field of endoscopic SS-OCT**, which include a novel SS-OCT system using a multimodal interferometer with double-clad fibres (Sect. 3.2), a dispersion compensation algorithm (Sect. 3.1.6), two scanning mechanisms (Sect. 3.3) including a translation stage and a piezo-tube (PZT) fibre-tip cantilever endoscopic probe and finally an original interleaving algorithm that increases the density of A-scans per B-scan hence improving image quality.

3. **Chapter 4 - OCT imaging results**
   The first half of this chapter defines what colonic polyps as well as the proposed imaging procedure (Sect. 4.1 - Sect. 4.3). The second part presents **original contributions** including B-scans of ex-vivo colon samples using the translation stage (Sect. 4.4) and using the endoscopic OCT probe (Sect. 4.5.1). Additionally, images of human tissue are presented (Sect. 4.5.2).

4. **Chapter 5 - Conclusions**
   The most important results of the thesis are summarised and recommendations for further development of the OCT system are made.

5. **Appendix (A.1)**
   The appendix includes the Scilab codes for dispersion compensation and interleaving as well as the developed LabView codes.

The original contributions of this thesis as mentioned before were accomplished through several building blocks (Fig. 1.6):

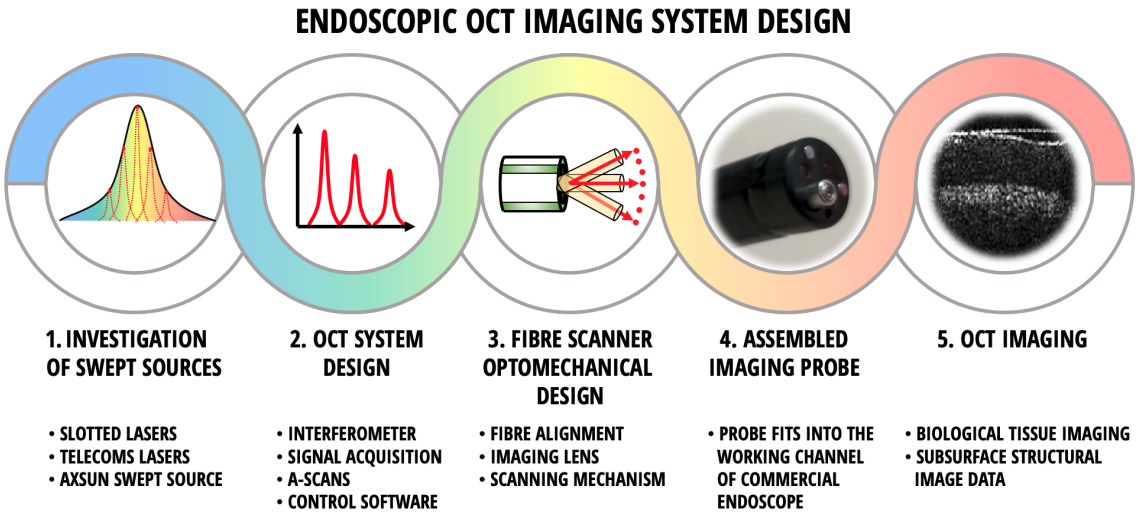

Figure 1.6: OCT endoscopic imaging probe design and assembly. 1) Investigation of swept sources including telecoms lasers and Axsun source. 2) OCT system design comprised of interferometer, signal acquisition, A-scan optimization and control software. 3) Fibre scanner optomechanical design including fibre alignment with the imaging lens and scanning mechanism. 4) Assembled imaging probe to be fit into the working channel of a commercial endoscope. 5) OCT imaging of biological tissue to obtain subsurface structural image data.

1. **Investigation of swept sources** using the heterodyne DC/AC measurement setup to characterize multi-section slotted lasers processed in-house and tunable telecoms lasers (SG-DBR). For the SS-OCT setup, a commercial swept source (Axsun, Excelitas Technologies, MA, USA) with a 200 kHz A-scan rate and 80 nm tunning range at 1300 nm was used to obtain an axial resolution of $10\mu m$ in air.

2. **OCT system design.** The first design block is an optical interferometer at 1300 nm with low insertion losses in order to create the interference pattern including the option to integrate with other imaging modalities such as Multi-Photon Tomography (MPT). The second design element includes detection optics and electronics. A balanced photodetector is used to detect the OCT signal which is sampled by an electronic acquisition card. The third element is control software to synchronize and post-process the OCT images as well as dispersion compensation and interleaving algorithms. This software includes LabView, Scilab and Matlab codes.

3. **Fibre scanner optomechanical design.** This includes a scanning mechanism in order to acquire cross-sectional images (B-scans). This thesis presents two mechanisms, one using a translation stage referred to as stand-alone system and the second one using an endoscopic probe referred to as PICCOLO probe.

4. **Assembled imaging probe**. With the previous three design blocks, assembly of the imaging probe was accomplished by precise electronic timing synchronization, micron alignment of the optical elements, scanning of the optical fibre and control software.

5. **OCT imaging**. Once a solid imaging probe is available acquisition of B-scans of biological tissue is performed to observe subsurface structural image data.

Chapter 2

Swept Sources

2.0.1 Review of background material

Swept sources have become the main element for SS-OCT to be able to provide higher sensitivity and scan speeds of up to 200,000 A-scans/sec without loss of image quality as well as reduction of image artifacts. This has been accomplished by the use of swept sources that sweep a wavelength range allowing the acquisition of interference signals at individual wavelengths measured with a balanced photodetector. The optical properties of a swept source are defined as the starting point in Sect. 2.1. Sect. 2.2 discusses the types of swept sources including several tuning mechanisms as well as the available commercial sources. The Axsun swept source used in this thesis is described in terms of its optical and electrical signals in Sect. 2.3.

2.0.2 Contributions to the field

A major factor for the development of the SS-OCT are akinetic laser swept sources. These sources allow fast speed OCT imaging with higher sensitivities as well as being cost-effective due to the wafer-scale laser manufacturing technology. For such reason, three original contributions to this field are presented in Sect.2.4:

1. **Heterodyne DC/AC measurement setup** (Sect. 2.4.3 and Sect. 2.4.4). An opto-electronic setup capable of characterizing akinetic tunable laser sources in terms of wavelength, side-mode suppression ratio (SMSR), and electric currents is presented. This also includes the required software for data acquisition and post-processing.

2. **Characterization of telecoms lasers as swept sources**. These include DC and AC optical characterization using the heterodyne measurement setup of multi-section slotted lasers processed in-house (Sect. 2.4.5 and Sect. 2.4.6) and commercial tunable telecoms sampled grating distributed bragg reflectors (SG-DBR) lasers (Sect. 2.4.7 and Sect. 2.4.8).

3. **Wavelength tuning dictionaries**. The final output of the characterization of the akinetic tunable lasers sources is a tunning dictionary containing the necessary current combinations to obtain a linear sweep. With this tunning dictionary it is possible to determine the capabilities of a tunable laser to be used as a swept source. Finally discussion and conclusions are presented in Sect. 2.5.

2.1 Optical properties of a swept source

A swept source laser is a light emitting device that produces an optical signal over a wide wavelength range with instantaneously narrow spectral width. A swept source is able to produce light of a single wavelength, and then sweeping the wavelength in a continuous fashion producing a time-average broad spectrum. Also, an ideal source, shall produce continuous tuning without gaps in the spectrum or considerable discontinuities. This continuous tuning must be repeatable without time variations with sweep rates between 50 kHz up to 1 MHz. These sources have been critical to develop new OCT applications as they provide advantages for real-time in-vivo diagnostics and high sensitivities[61].

An ideal swept source is able to sweep individual wavelengths along the bandwidth with a low intensity noise (RIN), it must have high phase repeatability between consecutive wavelength sweeps, a long term operation, clean imaging performance to provide narrow point spread function (PSF) peaks without sidelobes or secondary peaks and an adequate coherence length creating a time-averaged broad band spectrum[62]. The properties of a swept laser are shown in Fig. 2.1:

- **Center wavelength/Wavelength region** λ_c: The selection of the center wavelength λ_c depends on the scattering and absorption properties of the biological sample. The 840 nm window is use for retinal imaging due to low water absorption through the eye length and high scattering in retinal layers. The 1,060 nm window provides a high penetration in retinal layers. The 1,310 nm window is useful for imaging of anterior chamber of the eye as well for samples that require deeper tissue penetration due to its low scattering[61].

- **Output power:** the ideal power profile of a swept source is flat for all lasing wavelengths with each spectral region outputting the same power (Fig. 2.1a). This profile depends on the laser cavity, sweep frequency, and on the gain of the optical gain chip.

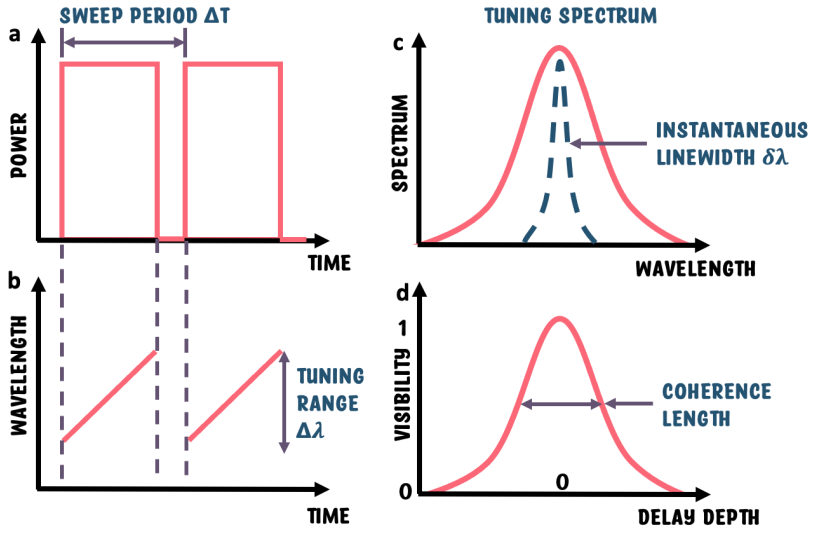

Figure 2.1: Optical properties of a swept source. a)Power profile b) Tuning curve c) Optical spectrum d) Coherence length. Image taken from [62].

- **Tuning curve:** is the output wavelength as a function of time. The curve is a well defined and continous linear tuning, unidirectional and going from shorter to longer wavelength (Fig. 2.1b). Ideally, the wavenumber, $k = 2\pi/\lambda$, is tuned linearly over time instead of the wavelength with the purpose of sampling the interference pattern uniformly and then calculating the Fourier transform to obtain a depth profile.

- **Sweep repetition/A-scan rate, f:** is the reciprocal of the sweep period ΔT and determines sweep frequency of the tuning curve. Faster sweep rates require electronics with faster acquisition rates in the order of 500 MSPS - 2 GSPS. The sweep repetition rate is a crucial parameter for OCT endoscopy. For a standard swept source OCT, the position of the imaging probe is assumed fixed, while the wavelength is swept through its cycle. Following movement to the next position a matrix of wavelength vs position is acquired in the manner shown in Fig. 2.2a. However, for a forward scannning PZT probe, a fibre is oscillated at a fast rate of 1.4 kHz. Considering a 200 kHz A-scan rate, one obtains only approx. 70 distinct points per

half oscillation cycle, and due to non-uniform velocity of the fibre, a maximum spatial separation between the B-scan points of 4 μm at the centre of the oscillation which is at the limit of acceptability since this distance is comparable with the lateral resolution hence distorting image quality. This causes several problems - there are only a few vertical traces displayed in the image, providing little information, and due to fibre movement within an A-scan,Fig. 2.2b, the start of the interferogram and the end of the interferogram will be sampling different tissue, which will seriously degrade the Fourier transform, and hence the OCT image. The problem of fibre movement during an A-scan is made worse for larger physical sweep range. Hence, swept sources with greater than 200 kHz A-scan rate are required.

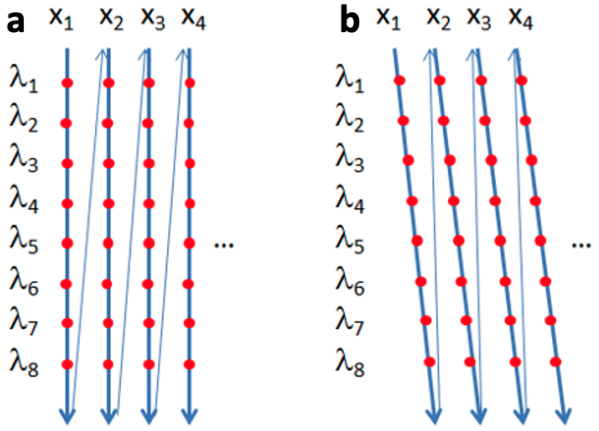

Figure 2.2: a) Ideal OCT sweep - the probe position is held at position x1, and the wavelengths λ are swept in that position. Then the probe position is moved to position x2 and so on. b) If the probe position is moving during a scan, the wavelengths are probing different sample positions. Filled circles show data acquisition moments.

- **Tuning/sweep range** $\Delta\lambda$: The spectral bandwidth defines the axial imaging resolution. Assuming a Gaussian spectrum (Fig. 2.1c), the tuning range goes from edge to edge at -3dB full width at half maximum level (FWHM). For a Gaussian spectrum with a tuning range $\Delta\lambda$ the axial resolution is given by:

$$\Delta z \approx 0.75 \frac{\lambda_c^2}{\Delta\lambda} \tag{2.1.1}$$

- **Instantaneous linewidth** $\delta\lambda$: During a wavelength sweep the laser emits a finite linewidth ($\delta\lambda$) spectrum instantaneously. This leads to a sensitivity fall-of with imaging depth. For a Gaussian-shaped linewidth, the coherence length, z_c is related to the instantaneous linewidth by:

$$z_c \approx \frac{2ln2}{\pi} \frac{\lambda_c^2}{\delta\lambda} \tag{2.1.2}$$

  The coherence length is defined as the optical path length difference (OPD) over which the coherence function drops from its maximum to 50% (Fig. 2.1d).

- **Intensity noise (RIN)**: an ideal swept source laser output must not present intensity fluctuations associated with laser gain and the cavity as this produces image artifacts. The intensity variations are produced by the internal tuning mechanisms and intracavity components.

- **Output polarization**: the desired output polarization is linear polarization, however the optical components such as the splitters, optical fibres can change the polarization state hence creating a polarization-dependent delay in the interferometer.

2.2 Types of swept sources

Several tuning mechanisms have been developed in order to meet the defined optical properties including sweep repetition rate, sweep range, instantaneous linewidth. In particular, swept-source OCT requires sources with fast repetition rates in the order of kHz up to 1 MHz as well as large sweep range between 40-100 nm. Different configurations

to fulfill these requirements include an external cavity semiconductor laser[22], semiconductor optical amplifier gain sections[63], frequency comb swept lasers using of fibre ring cavities[64] and Fourier domain mode-locked lasers (FDMLs)[65, 66]. Swept sources based on external cavity lasers using micro electro-mechanical systems (MEMS) filters have become a commercially available option due to their compact size, power and optimum output power[67, 68]. Vertical-cavity surface emmiting laser (VCSELs) swept sources have also proven to generate stable single-mode lasing and long coherence lengths[69, 70]. Akinetic swept sources remove the mechanical tuning mechanism by using laser diodes electronically controlled using distributed Bragg reflectors (DBRs) providing longer coherence length and customization for the sweep profiles [71].

Different commercial swept source technologies are available in the market[72, 73], each one having particular advantages in terms of sweep repetition rate, tuning range, center wavelength and output power depending on the application. These sources are provided by Axsun Technologies (MEMS tunable filter)[74], EXALOS (MEMS tunable filters)[75], NTT (External resonator) [76], Santec (Polygon Scanners) [77], Thorlabs (VCSEL) [78], Superlum (Acousto-Optical Tunable Filter)[79], Optores (FDML Laser)[80] and Insight Photonic Solutions (Akinetic Semiconductor Laser)[81]. A summary of the swept sources is given in Table 2.1.

In contrast to the swept sources based on mechanical movements, akinetic semiconductor technology based on wafer-scale lasers are flexible, compact and can potentially reduce the price of swept sources due to high-volume manufacturing of telecoms suppliers[72]. OCT imaging capabilities with such akinetic all-semiconductor swept sources have been proven[82, 83, 84] at different sweep rates from 20-200 kHz with different axial resolutions between 10 μm to 20 μm at 1060, 1310 and 1550 nm. With increasing applications of akinetic swept sources it is important to have new characterization techniques to compare the performance of these sources. For this reason a heterodyne method that is able to create DC and AC tuning maps of tunable telecoms lasers is presented in Sect. 2.4.3.

Table 2.1: Summary of commercial swept sources; f: sweep repetition rate; λ_c: center wavelength; $\Delta\lambda$: sweep range; Δz: Axial resolution

Company	f	**Laser type**	**Filter Type**	λ_c	$\Delta\lambda$	Δz	**6 dB roll-off**	**Output power**
	kHz			nm	nm	μm	mm	mW
Axsun[74]	200	Short Cavity	MEMS FP-TPF	1310	100	8	5	18
Exalos[75]	20	Short Cavity	MEMS	1310	150	6	6	25
NTT[76]	200	Short Cavity	Electro-optic	1310	100	9	7	17
Santec[77]	100	Short Cavity	MEMS FP-TF	1310	100	9	13	
Thorlabs[78]	200	VCSEL	MEMS	1310	100	9	50	25
Optores[80]	1500	FDML	FFP-TF	1310	110	7	10	
Insight Photonics[81]	180	VT-DBR	Vernier	1310	90	9		30

2.3 Axsun swept source

The final swept source optical coherence tomography (SS-OCT) system in this thesis uses an Axsun swept source. The Axsun laser has a tuning mechanism based on a semiconductor external cavity laser (ECLs) and micro electromechanical systems (MEMS) as filters and reflectors[85, 86]. The basic structure of an ECL is to replace one high-reflectivity side of the laser diode for an external mirror. This provides flexibility to adjust the cavity parameters, hence reducing the mode spacing of the laser output[87]. A second advantage of ECLs is that extra cavity elements can be inserted such as spectral filters or wavelength selective elements to achieve tunability to provide stable narrow linewidths[88]. In terms of requirements for a swept source, ECLs are able to provide large sweep ranges, fast repetition rates while keeping low linewidths.

The basic optical elements of the Axsun swept source are a broadband 1300 nm gain chip, a reflective MEMS tunable Fabry-Pérot filter that serves as the frequency tuning mechanism[89], and a fiber reflector that forms the other end of the laser cavity and used

as the output coupler as shown in Fig. 2.3. These elements are combined into a short cavity ECL that fits in a 14-pin optical butterfly package.

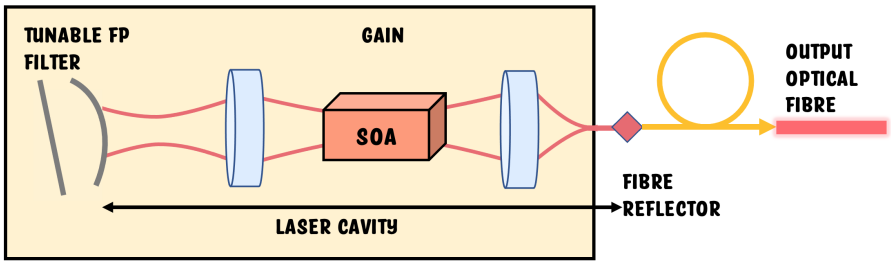

Figure 2.3: External cavity laser with reflective Fabry-Perot MEMS tunable filter [90].

Frequency tuning is achieved with the MEMs tunable Fabry-Pérot. The filter is designed such that it matches the output laser mode emitted by the SOA gain chip. With the introduction of an angular offset between the optical axis of the laser and the filter cavity, a spectrally filtering retro-reflector effect can be obtain. This is equivalent to an optical passband filter design to have a large free spectral range (FSR) and low bandwidth filter function[89]. Therefore, it is possible to operate the filter in a reflective operating regime, hence creating a tunable reflection peak that can be changed by driving the voltage on the MEMS filter which tunes the center frequency of the passband filter.

With the previous elements combined, the swept source operation is illustrated in Fig. 2.4. Longitudinal modes that have enough gain from the laser medium are formed in the ECL, these are standing waves within the cavity. The wavelength of these waves is an integer multiple of the optical cavity length:

$$m\lambda = 2nL \tag{2.3.1}$$

m is a positive integer, n is the refractive index of the cavity and L is the cavity length. The frequency spacing (FSR) δf is then defined as:

$$\delta f = \frac{c}{2nL} \tag{2.3.2}$$

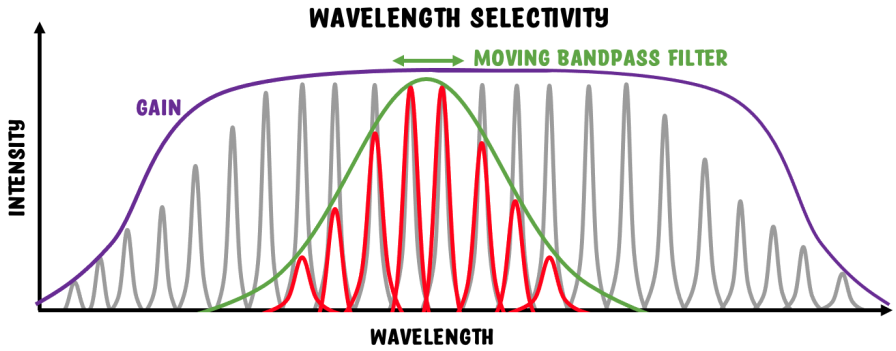

Figure 2.4: Intra-cavity filter ECL swept source operation with a moving band-pass filter (green) and gain curve (purple). The grey modes represent the cavity modes, the red modes are the lasing modes being filtered.

The bandpass filter can moved around the different modes in order to allow only specific number of modes to be able to lase either in single or multi-mode. As the filter selects the following mode, the laser 'mode-hop' to the next mode close to the central wavelength of the filter. The approximate cavity length including the fibre extension is about 104 mm. This sets a requirement to design the interferometer such that stray reflections are not separated by intervals of half cavity length (steps of 52 mm) as this introduces image artifacts.

2.3.1 Optical spectrum and control signals

The optical spectrum defines the wavelength content of the output laser. This can be measured with an optical spectrum analyzer (OSA), which is not the instantaneous wavelength due to the low speed of the OSA, but the average optical power. The sweep range of a swept source is specified as the range over which the spectral power drops -10 dB relative to the peak value. The measured spectrum of the Axsun laser is shown in Fig. 2.5a.

The laser spectrum is over 100 nm wide from 1240 to 1345 nm with a center wavelength at ≈ 1310 nm. Notice the two spikes at the beginning and end of the sweep, this is due to the mechanical slowing down of the filter. In practice, only the wavelengths of the center of the sweep contribute to the axial resolution hence having a sweep range of ≈ **80 nm**, **therefore the expected axial resolution of the OCT system is ≈ 10 μm in air**.

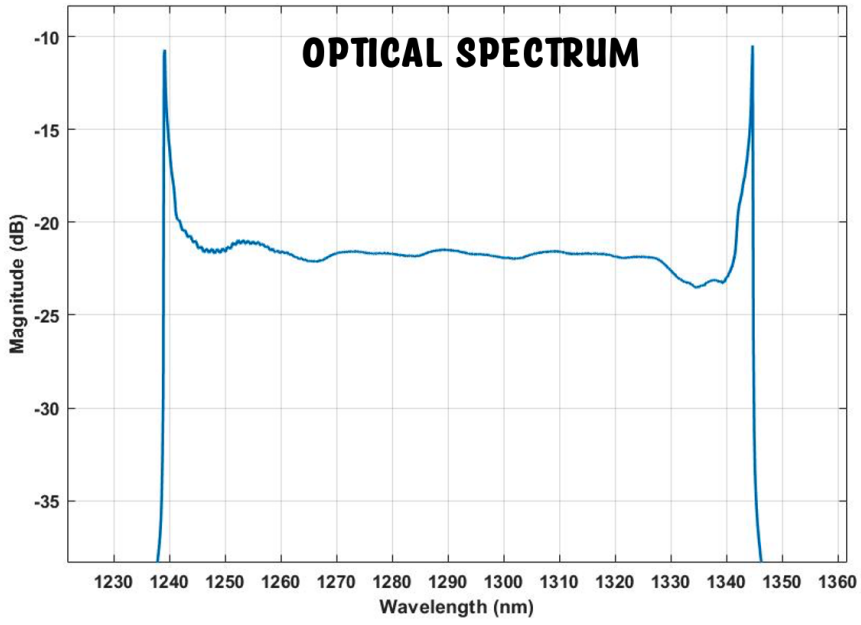

Figure 2.5: Measured optical spectrum of the Axsun swept source showing a wavelength sweep from 1240-1345 nm. The useful tuning range is from ≈ 1250-1335 nm.

Three main signals are generated with the Axsun laser, the optical laser output and two electronic signals, λ-trigger and k-clock. Such signals are shown in Fig. 2.6. The trigger signal indicates the start of a sweep and can be used as an A-scan trigger for the acquisition card. The k-clock is a signal generated using an internal fiber-based Mach-Zehnder interferometer (MZI) which functions as a real-time uniform k-space external clock in order to enable uniform data sampling in k-space[91], so that a Fourier transform can be directly performed on the spectral interferogram. This allows signal synchronization between the acquisition card and wavelength sweep. Due to the high frequency of

the k-clock (500 MHz), the acquisition card must be able to sample at least at 1 GHz. The sweep rate or A-scan rate is 200 kHz, meaning that a complete sweep is performed every $5\mu s$. The specifications of the laser are shown in Table 2.2.

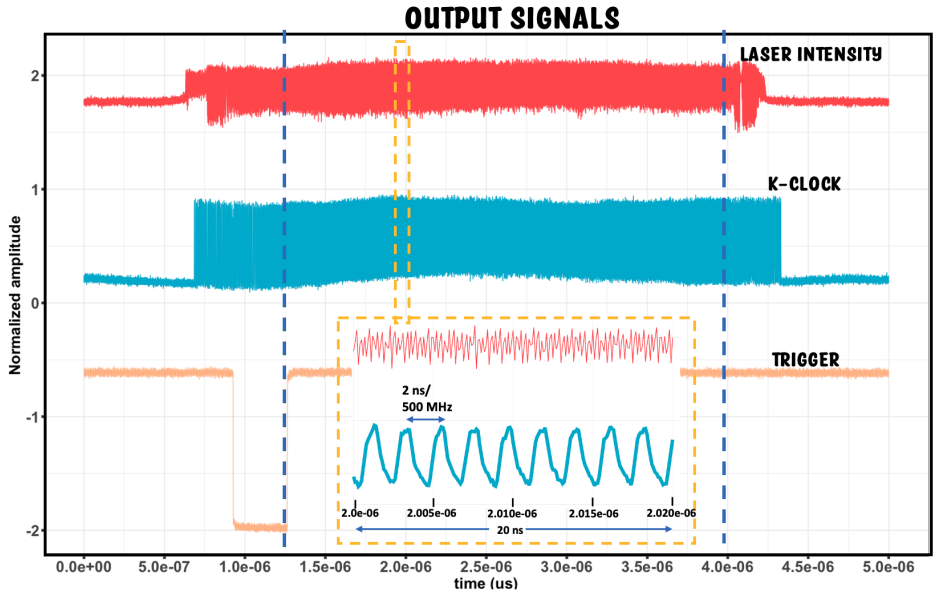

Figure 2.6: Measured output signals of the Axsun swept source. Laser intensity (red), K-clock (blue) with a frequency of 500 MHz and λ-trigger (orange) to indicate the start of the wavelength sweep. The useful tuning range is enclosed within the dashed blue lines.

2.3.2 Signal synchronization

When using the Axsun swept source one must consider the non-linear relationship between time and optical frequency in order to properly synchronize the interference signal with the acquisition electronics. Ideally the swept source should reproduce every sweep equally, however in practice there are variations per every sweep, hence creating uncertainties in the measured spectral interferogram such as out-of-phase interferograms. In order to synchronize the swept source with the data acquisition, the k-clock is generated as a common time reference and is also used as an acquisition trigger or sampling clock for the digitizer card. If the timing signal is delayed with respect to the acquisition of the OCT

Table 2.2: Axsun laser specifications.

Parameter	Units	Value
Sweep Rate	kHz	200.32
Center wavelength	nm	1300 nm
Wavelength Tuning range	nm	104.71
Average Power	mW	26.158
Coherence Length	mm	16.32
MZI path length difference	μm	83.85
External Clock Min Frequency	MHz	316.3
External Clock Max Frequency	MHz	542.7
Sampling clocks	count	1066

interferogram then the sampling will not be synchronized. Such delays can be caused by coaxial cables as well as resistive and capacitive elements. The proposed synchronization method consists of three main signals (Fig. 2.7):

1. **OCT signal f(t)**: OCT interference pattern sampled with N points.

2. **K-clock g(t)**: This signal is used to sample the OCT signal at linearly spaced sampling points in k-space ($k = 2\pi/\lambda$).

3. λ **− trigger h(t)**: This signal is produced every time the laser starts a full sweep. This can be used as an A-scan trigger.

Real swept sources have sweep instabilities producing timing jitters in signals $f(t)$, $g(t)$ and $h(t)$. The first case is the OCT signal with respect to the k-clock: $f(t) - g(t)$. The second case is the time delay between the k-clock to the λ-trigger. In order to balance the time delays, optical fibres and coaxial must be either added or removed as well as modifying the internal delay of the swept source.

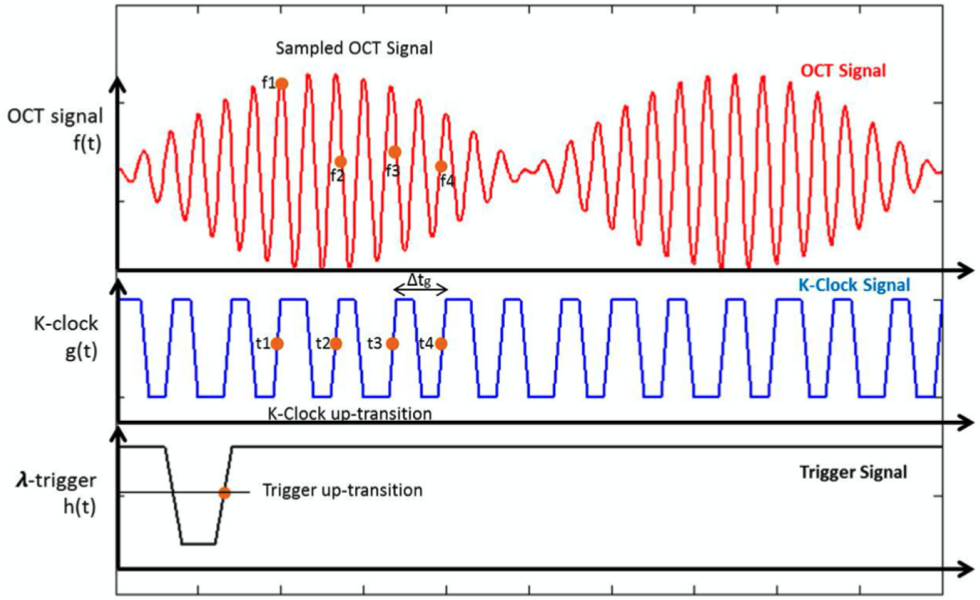

Figure 2.7: Signals include the OCT interferogram, k-clock and λ-trigger signals.

2.4 Akinetic semiconductor swept sources

Akinetic all-semiconductor technology based on wafer-scale laser fabrication can potentially reduce the price of swept sources due to high-volume manufacturing of telecoms suppliers. The only akinetic swept source commercially available (Insight Photonic Solutions[81]) is based on a Sampled Grating Distributed Bragg Reflector (SG-DBR)[92]. Despite such advantages, SG-DBR lasers have insufficient functionality for OCT applications, e.g., invalid points in the sweep, poor quality of the point spread function (PSF) and large stitching noise [93]. In order for akinetic swept sources to be established as the future core technology of SS-OCT these limitations have to be well understood.

Additionally, the potential of multi-section slotted tunable lasers processed in-house to be the core of a swept source has also been studied. The limitations of both multi-section and SG-DBR lasers can be understood by a DC and AC characterization. DC characterization provides a broad understanding of the behavior of the laser in terms of its tuning

range, center wavelength, average power and SMSR. SS-OCT requires swept sources to be tuned dynamically, hence it is necessary to perform AC/dynamic lasing wavelength characterization. This was achieved with the proposed automated heterodyne method which yields a 'tuning dictionary' containing different current combinations that will control the output lasing, ideally linearly spaced in k-space. This automated heterodyne method will be a useful tool for swept source researchers in order to characterize tunable lasers in terms of electronic switching speed, electric noise, mode-hopping and tuning range providing a broader understanding of the output lasing wavelength, side-mode supression ratio (SMSR) and output power.

2.4.1 SG-DBR lasers

The core laser of akinetic swept sources is an all-semiconductor SG-DBR monolithic tunable laser diode centred around 1310 or 1550 nm at a fast wavelength tuning speed ($\approx$ 5 ns per wavelength). Lasing is obtained by applying an electric current through the sections of a semiconductor structure: back mirror (BM), phase, gain, front mirror (FM) and semiconductor optical amplifier (SOA), as shown in Fig 2.8. The injection of electric carriers to each section produces a change in the refractive index, hence a change of the effective optical path length. Each section has a specific purpose. The gain section provides an amplification region for continued lasing in order to obtain stimulated emission. The FM, BM and phase sections control the output wavelength for ideal continuous frequency ramps required by SS-OCT. The FM and BM are sampled grating distributed Bragg reflectors (SG-DBR) that provide broad semi-continuous wavelength tuning (with mode-hopping), whereas the phase section provides fine tuning over a narrow range of continuous tuning, such effect is obtained by modulating the overall effective cavity length. The SOA allows power leveling of the output light, hence it can be used to modulate the output power as desired and is also used as a switch to shutter the output light.

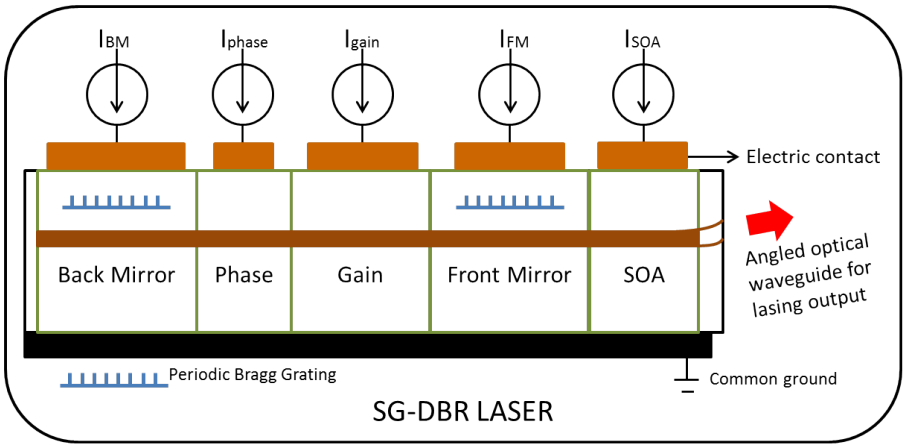

Figure 2.8: Cross-sectional view of a SG-DBR laser. The laser is composed of five sections: Back Mirror (BM), Phase, Gain, Front Mirror (FM) and Semiconductor Optical Amplifier (SOA). The combination of different values of currents I_{BM}, I_{phase}, I_{gain}, I_{FM} and I_{SOA} determine the lasing wavelength, optical power and side-mode suppression ratio (SMSR).

Continuous tuning range $\Delta\lambda$ is limited to $\approx$ 15 nm as defined by $\Delta\lambda \approx \Delta n/n_g$, where n is the index change and n_g the group index of the tuning sections; such tuning range can be extended by using two or more control variables. These control variables are the front and back mirrors whose structure is a Bragg reflector, an alternating periodic structure of two different optical materials, hence creating a periodic variation of the refractive index and high reflectance at specific wavelength values[94]. Sampled gratings create frequency dependent reflectivity spectra, where the spacing between the peaks is defined by the grating separation. Injection of carriers to both mirrors modifies the mirror spacing through a change in index of refraction, hence producing different wavelength dependent reflectivity profiles. It is this Vernier tuning mechanism on both mirrors that can be used in combination to select the available wavelengths across the tuning band. Due to different periodicity in the reflectivity spectrum only one alignment of the FM and BM peaks will occur[94]. The tuning mechanism is illustrated in Fig. 2.9.

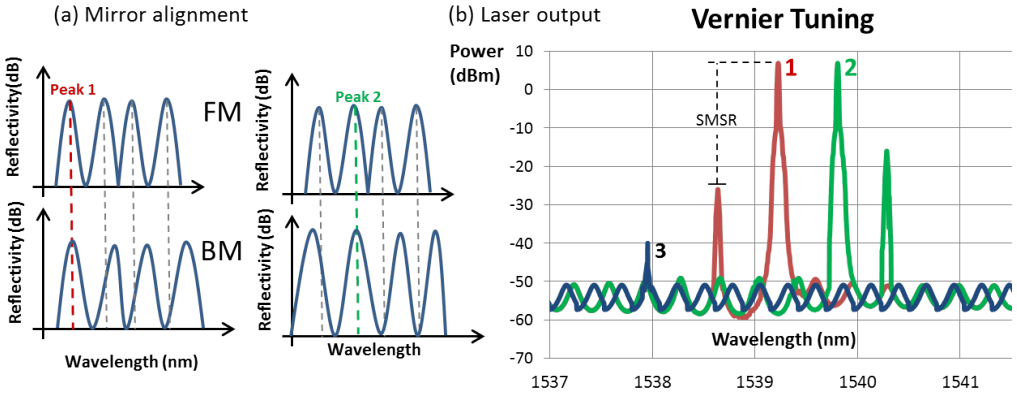

Figure 2.9: a) Reflectivity spectra defined by the grating spacing. Both spectra can be shifted by injecting carriers in order to obtain different peak alignments. b) The resulting main peaks have a given value of side-mode suppression ratio (SMSR), which is the relation of power between the center peak with the nearest higher order mode.

2.4.2 Slotted lasers

Tunable single semiconductor lasers have been used in optical networks, e.g., in wavelength division multiplexing (WDM) where single wavelength can be replaced by widely tunable lasers. Distributed-feedback (DFB)[95] and Sampled Grating Distributed Bragg Reflector (SGDBR)[92] lasers have provided useful single longitudinal and tranverse mode laser emission required by the telecomm applications. One advantage of DFB and DBR lasers is that they provide the optical feedback through a series of small refractive-index perturbations (no cleaving required), compared to conventional Fabry-Pérot (FP) lasers.

Another tunable configuration consists on etching a ridge waveguide in a Fabry-Pérot cavity, which produces a single transverse mode[96]. Nevertheless, the structure operates with multi-longitudinal modes. These multi-modes are then perturbed by etching a sequence of low-loss shallow slots (reflective defects produced by standard photolithography) into the active ridge waveguide, such slot sequence provides the necessary reflectivity for the laser operation independent of a cleaved facet, therefore creating single-modes. The control variables of the slots are the depth, position of the slot relative to the cavity

length and slot number. By accurately optimizing these variables, lasing with high Side Mode Supression Ratio (>30 dB) can be achieved.

Multi-section slotted tunable lasers[97] processed in-house include design device geometry parameters such as number of slots, depth, width, respective separation (period). Standard III-V laser fabrication steps were used to achieve high quality slotted sections since accurate slot dimensions and shape of the slot profile have a major impact on the device performance as a single mode tunable source. Fabrication of the high quality 1 μm slots in narrow ridge waveguide structure required a two-step UV lithography process. A multi-section slotted laser is shown in Fig. 2.10a, Fig. 2.10b shows an examples of etched slots.

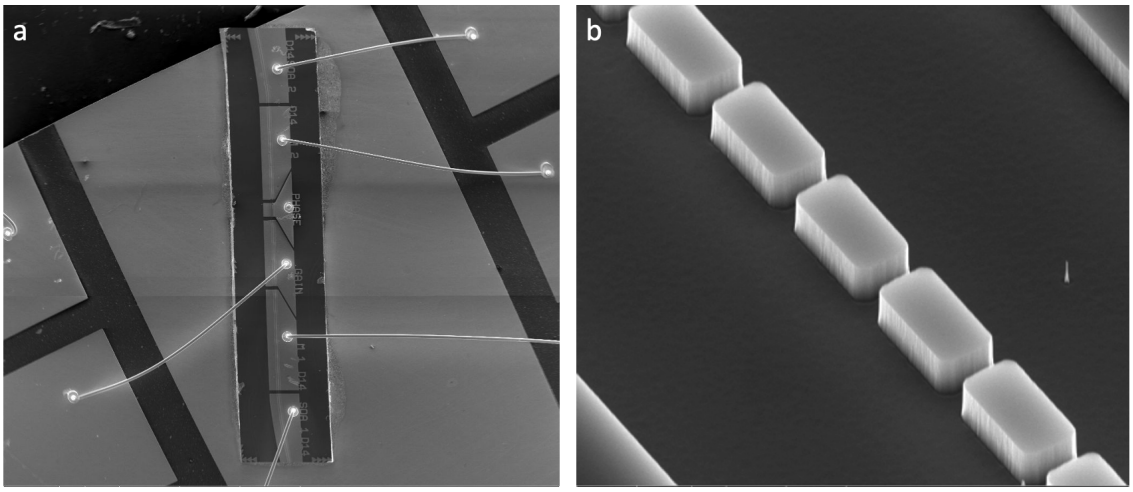

Figure 2.10: a) SEM image of the multi-section slotted laser showing the gain, soa, phase and mirror sections. b) SEM image of the slotted section of the lasers. The design and manufacturing of the slotted lasers is not work of this thesis, only their characterization.

2.4.3 Heterodyne DC/AC measurement setup

Tunable lasers can be characterized in DC and AC operation. The most basic characterization is to measure the lasing output wavelength, side-mode suppression ratio (SMSR)

and output power in DC operation as a function of the FM and BM currents while keeping the rest of the sections biased under a constant current. This output plot is called the tuning map of the laser[98, 99]. AC characterization is more complicated as the laser sections have to be dynamically tuned. In order to obtain both measurements a commercial telecoms SG-DBR laser (TLDM-6S Widely Tunable Laser Mode, JDSU Agile) and multi-section slotted lasers were used in the proposed electro/optical setup (Fig. 2.11) which is composed of two main blocks: DC characterization and AC characterization.

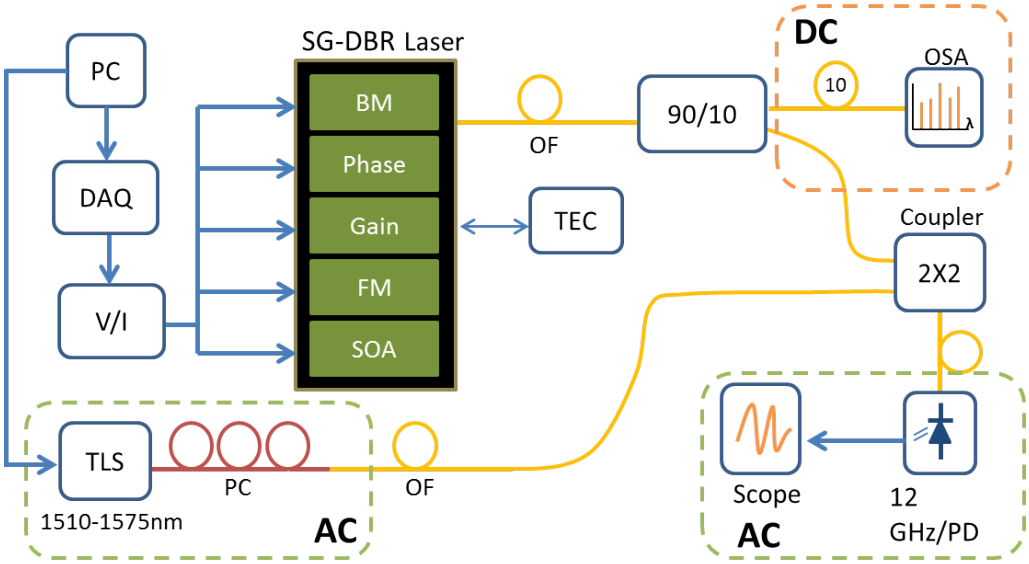

Figure 2.11: Heterodyne experimental setup. DAQ (Digital-to-Analog); V/I (Voltage-to Current converter); SOA (Semiconductor Optical Amplifier); OSA (Optical Spectrum Analyzer); TLS (Tunable Laser Source); PC (Polarization Controller); OF (Optical Fibre); PD (Photodetector); TEC (Thermo-electric controller).

For the DC characterization setup, a computer controls a Digital-to-Analog converter (DAQ National Instruments, PCI-6733) which generates a signal between 9 and 6 volts. The voltage signal is converted to a current signal through a Voltage-to-Current (V/I) converter, which is then injected to the laser. The SG-DBR laser is fiberized and 10% of its power is connected directly to an Optical Spectrum Analyzer (OSA). The temperature is regulated with a thermo-electric controller (TEC). The results are mapped to two different

tuning maps where the output wavelength and SMSR ratio are graphically represented as a function of the current combinations of the mirrors respectively. Such a map can be represented as a matrix (Fig. 2.12) where the size is determined by the number of steps in both BM and FM, $N_{steps_{BM}}$ and $N_{steps_{FM}}$. The number of steps is defined as $(I_{max} - I_{min})/I_{step}$. DC characterization provides an insight of the laser's behavior, however SS-OCT applications require fast sweeping rates (orders of kHz). Dynamic laser tuning modifies its optical behavior due to limited electronic bandwidth, hysteresis and increase in temperature. For such reason four elements are added to obtain the heterodyne/dynamic characterization: a reference tunable laser source (TLS, 1510-1575 nm), a 2x2 coupler, a 12 GHz photodetector and a fast scope (Tektronix, DP07000 100Gs/s). The TLS and slotted/SG-DBR laser outputs are combined at the 2x2 coupler; if their optical lasing frequency difference is less than the bandwidth of the photodetector (12 GHz), a beating signal is obtained, allowing the dynamic measurement of the lasing wavelength. Each current combination can be produced at a maximum speed of 10 μs per sample.

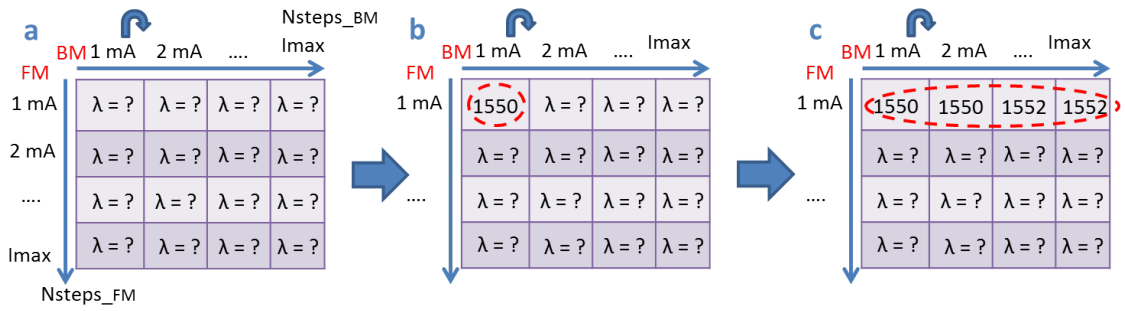

Figure 2.12: Raster current scanning. a) The tuning map starts as an empty matrix. b) The first FM, BM current combination is set and the lasing wavelength and SMSR are measured. c) The next column is measured until the matrix is filled.

2.4.4 Heterodyne measurement

The heterodyne/dynamic wavelength measurement is achieved by combining the TLS and tunable laser in a 2x2 coupler. The TLS provides a constant reference wavelength value, while the tunable laser is being dynamically tuned with a raster scanning pattern (Fig. 2.12). If at one moment in time it happens that the optical frequency ($f = c/\lambda$) difference between the TLS and the tunable laser is within the bandwidth of the photodetector (12 GHz) an oscillating beating signal will be measured by the scope. With this beating signal, the automatic heterodyne method is able to provide time resolved optical spectrum analysis of fast laser wavelength switching where the wavelength range is determined by the TLS. The addition of a polarization controller is used to align the polarization of the TLS electric field with the tunable laser field as two conditions must be met in order to obtain the beating signal: The spatial distributions must overlap and must not be orthogonal, while the polarization states must also not be orthogonal. The electronic signal is then recorded by a sampling oscilloscope. The electric field of the wavelength switched laser is defined as an addition of N laser modes [100, 101]:

$$E_s = \sum_{n=1}^{N} a_s^n(t) e^{j2\pi \int_0^t \nu_s^n(\tau) d\tau + \phi_s^n} \tag{2.4.1}$$

where $\nu_s(t)$ is the time-dependent frequency, $a_s(t)$ the time dependent amplitude, and phase $\phi_s(t)$. The electric field of the TLS reference laser can be approximated by a single delta function at frequency ν_{lo}:

$$E_{lo} = a_{lo} e^{j2\pi\nu_{lo} + \phi_{lo}} \tag{2.4.2}$$

The electric field incident on the photodetector is $E = E_s + E_{lo}$ and its intensity is $I = EE^*$. Assuming the TLS and the frequency of one of the laser modes of the tunable laser are within the bandwidth of the photodetector then the intensity of the beating signal is defined as:

$$I(t) = 2a_s(t)a_{lo}cos(\psi) + a_{lo}^2 + \sum_{n=1}^{N} a_s^n(t)^2 \tag{2.4.3}$$

where the beat signal phase, ψ, depends on the instantaneous frequency of the tunable laser ($\nu_s(\tau)$) and is defined as:

$$\psi = 2\pi\Big(\int_0^t \nu_s(\tau)d\tau - \nu_{lo}t\Big) + \phi_s(t) - \phi_{lo} \tag{2.4.4}$$

The term $a_{lo}a_s(t)$ depends on the tunable laser mode and determines the time varying envelope of the beat signal. In the setup of Fig. 2.11, the scope measures such an envelope from the photodetector while disregarding the phase of the beat signal. The bandwidth of the photodetector determines the allowable optical frequency differences that can be measured. The conversion from frequency to wavelength depends on the center wavelength according to:

$$\Delta\nu = \frac{c}{\lambda^2}\Delta\lambda \tag{2.4.5}$$

A beating signal can be measured according to the following experimental parameters: The DAQ is configured to have a sample rate of 100 kHz (sample/current combination produced every $t_{sample} = 10\mu s$), the total number of current combinations is given by $N_{stepsFM}{}^{*}N_{stepsBM}$ and the total matrix sweep time, $t_{sweep} = N_{stepsFM}{}^{*}N_{stepsBM} * t_{sample}$. For $N_{stepsFM} = N_{stepsBM} = 100$; $t_{sweep} = 100ms$. The beating signal is an oscillating signal whose frequency depends on the optical frequency difference of the signals as illustrated in Fig. 2.13a. Once a beating signal is obtained, its signal quality is measured by calculating its AC- Root Mean Square Voltage (AC-RMS), which can be directly obtained from the scope according to:

$$AC - RMS = \sqrt{\frac{\int_{start}^{end}(Waveform(t))^2 dt}{(End - Start) * SampleInterval}} \tag{2.4.6}$$

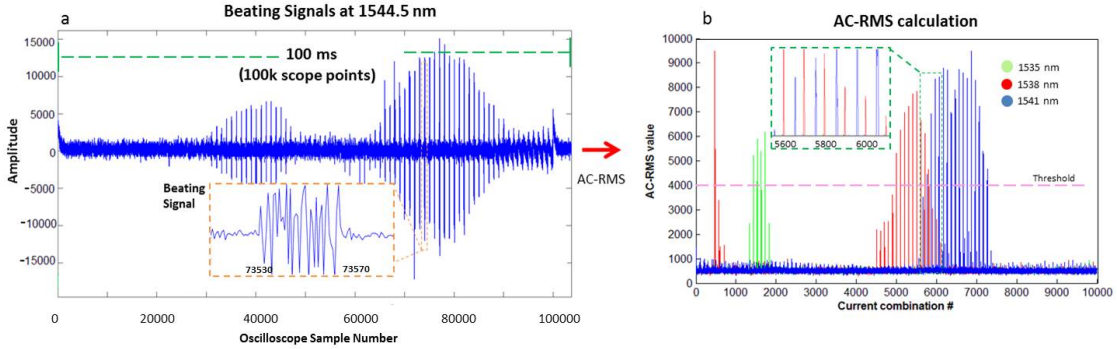

Figure 2.13: Beating signal AC-RMS of SG-DBR laser. a) TLS set to lase at 1544.5 nm. Several beating signals are measured at the photodetector in an window of 100 ms and 100k sampling points. b) The AC-RMS is calculated for every 10 points of the scope for a total of 10000 current combinations (x-axis) in order to quantify the quality of the oscillating signal. Those that are above the reference threshold are remapped to a matrix.

In order to characterize the tunable laser in its full tuning range, the TLS is tuned in steps of 0.1 nm, while the laser is being dynamically tuned. The AC-RMS per current combination is calculated for all reference wavelengths and then compared against a reference threshold level (Fig.2.13). If the AC-RMS value is above the threshold then the tunable laser is lasing at an optical frequency difference of less than 12 GHz with respect to the TLS. All the current combinations that are above the threshold are then remapped to a matrix representing the pairs of current combinations as in Fig. 2.12 and are the combinations that make the tunable laser lase at the reference wavelength. The following process is to select the adequate current combination per wavelength.

2.4.5 Multi-section slotted laser DC results

The multi-section slotted laser has five tunable currents, three of which are usually set at fixed operating points. The remaining two currents are labelled Mirror 1 and Mirror 2, which are varied from 0 to 250 mA. Fig. 2.14 show the DC characterization. The colour map (Fig. 2.14a) refers to the peak wavelength of emission as a function of two tuning

currents. Wavelengths are found to be between 1525 and 1610 nm. For an OCT system, the laser needs to have a single peak, but all semiconductor lasers emit over a range of wavelengths, so the further requirement is that wavelengths away from the main peak have a power factor of 1000 below the main peak. This ratio (Fig. 2.14b)is known as side-mode-supression-ratio (SMSR). Colours noted in yellow orange and red have SMSR $>$ 30 dB, which is an acceptable value. A histogram for wavelength values with SMSR $>$30 dB is shown in Fig. 2.14c. Finally, the tuning range for single mode is shown in Fig. 2.14b.

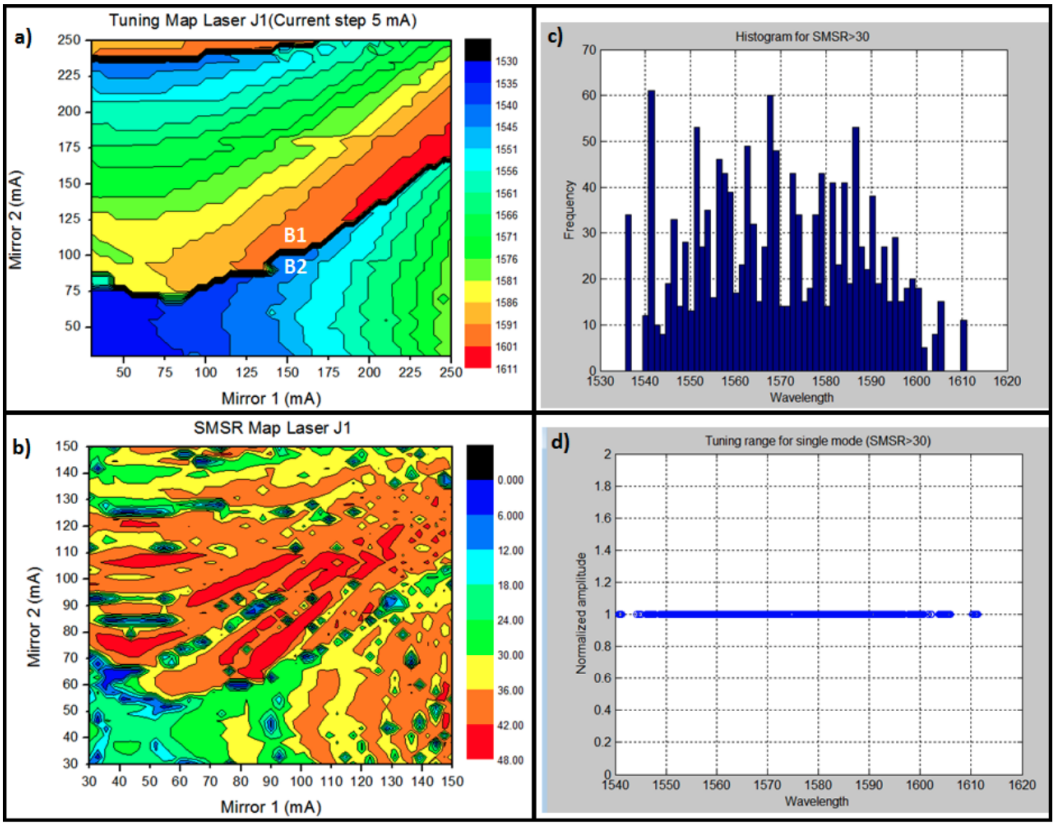

Figure 2.14: Multi-section slotted laser DC tuning map. a) Tuning wavelength map with tuning areas B1 and B2. b) SMSR Map. Laser configuration: Gain = 50 mA; Phase = 20 mA; SOA1 = OFF; SOA2 = 10 mA; Current sweep: M1 = M2 = 30 -150 mA (5 mA steps); TEC = 21° OSA resolution = 0.1 nm. c) Histogram for values with SMSR $>$ 30. d) Tuning range for values with SMSR $>$ 30; notice the gaps in the tuning range, ideally these should be filled by fine-tuning the phase section.

Experimental results have demonstrated single mode operation of the lasers at CW powers exceeding 4.5 mW. A broad tuning range of the order of 60 nm has been obtained for the ascribed design confirming the development of the highly accurate fabrication process of these multi-section laser devices. The dimensions of this laser is approximately 2 x 0.2 mm^2.

2.4.6 Multi-section slotted laser AC results

A dynamic AC tuning map was obtained with the heterodyne setup as shown in Fig. 2.15. The colour bar in the tuning maps represents the wavelength. The yelowish colour that covers most of the area of the map means that either there was no beating signal detected or the quality of the signal was too noisy to decide if there was a beating signal. The DC tuning map (Fig. 2.14) presented clear tuning maps, however when increasing the tuning frequency the performance was not as expected as no clear tuning paths were identified. This is a clear indication that the lasing wavelength depends on the sample rate at which the currents are produced as the laser is highly sensitive to noise on the input signals. A second reason were power fluctuations observed when the laser sections were at constant bias. Because the power is not constant, the proposed method will not provide accurate information, hence one of the main conclusions from this characterization is that the design of slotted laser needs to provide constant optical power for constant bias at the laser sections to use the proposed characterization technique.

2.4.7 SG-DBR DC results

DC characterization of the SG-DBR laser in terms of its lasing wavelength and SMSR was performed with the setup shown in Fig. 2.11. The wavelength tuning map (Fig.2.16a) relates the lasing wavelength as a function of both the BM and FM currents, for constant values of gain and phase.

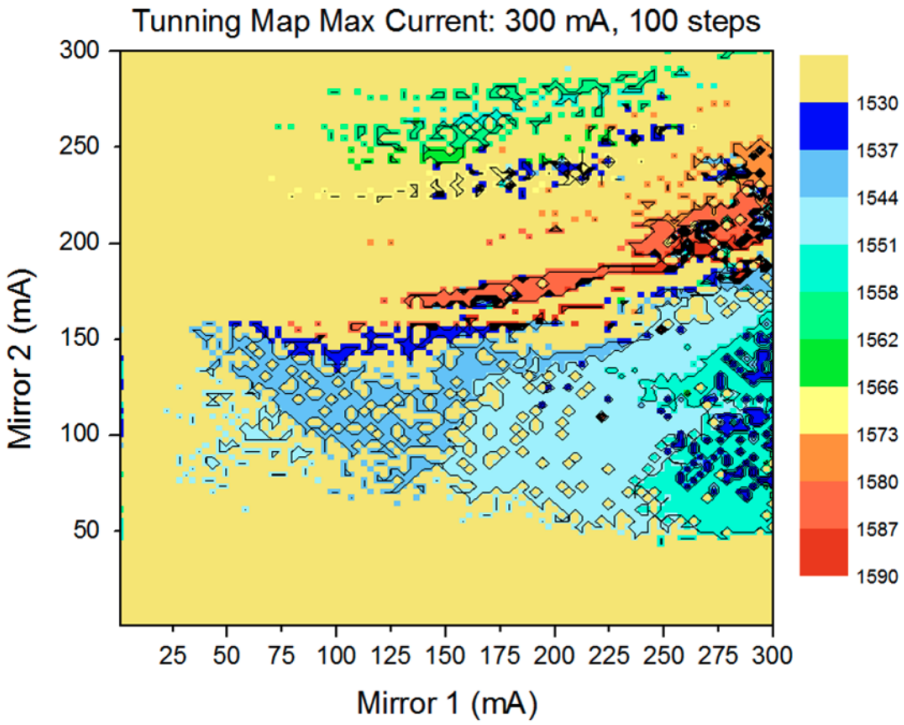

Figure 2.15: Slotted laser dynamic tuning map for a max current of 300 mA per mirror.

Three tuning sections can be identified: C1-3. Section C1 and C3 are limited in their tuning range and have very narrow tuning paths, hence they are discarded as it is not convenient to operate the laser in these sections. In contrast, C2 is the main tuning region which covers the whole tuning range and has a 'fanlike' shape where several wider tuning paths can be identified. With this pattern it is possible to find a tuning path with increasing wavelength in order to avoid being close to the borders of the neighboring paths and therefore reduce mode hopping. Such effect degrades the swept source lasing quality due to unexpected lasing wavelengths, hence this must be avoided. Notice, however, that for small current combinations the tuning paths are closer to each other, therefore increasing the probability of mode hopping. This effect can be minimized by increasing the DAQ resolution and decreasing the electronic noise in the connections through electronic filtering and by placing the laser in a printed circuit board (PCB) where the impedance of

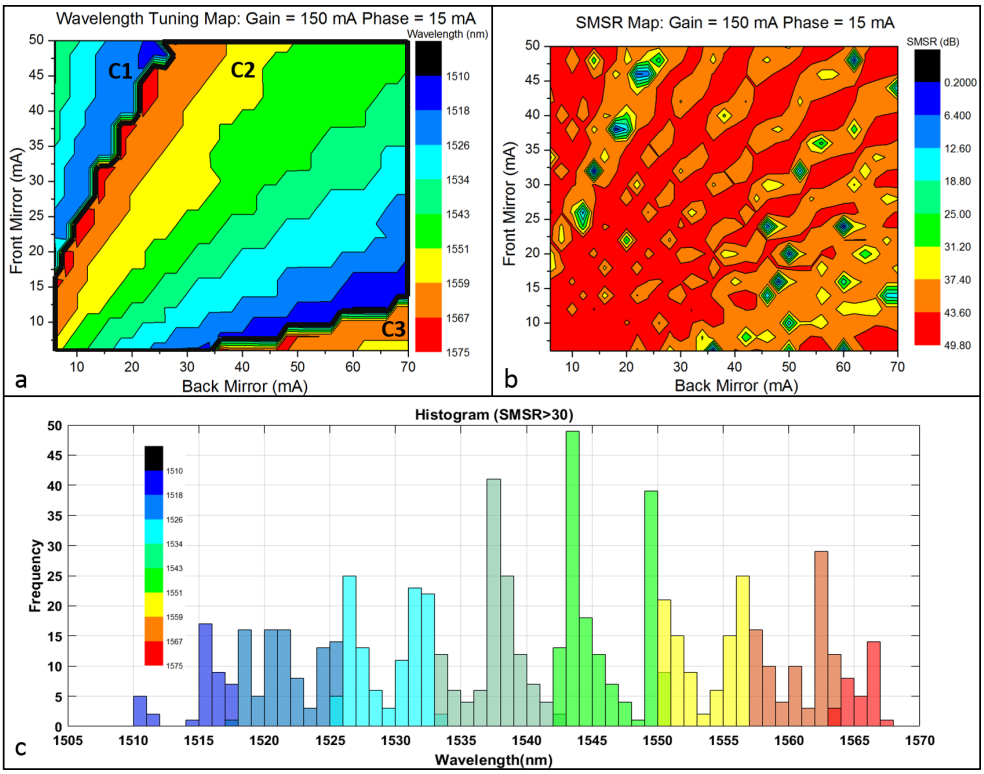

Figure 2.16: a) Wavelength Tuning Map with three tuning sections (C1-3). Tuning region C2 has clearly defined tuning paths. b) Side-mode supression ratio (SMSR) map. c) Wavelength histogram for values of SMSR>30. Laser configuration: Gain = 150 mA; Phase = 15 mA. FM: 6-50 mA (2 mA step); BM: 6-70 mA (2 mA step). OSA resolution: 0.1 nm

each trace matches the electric impedance of each section of the laser. The SMSR Map (Fig. 2.16b) shows that the laser had a remarkable single-mode operation (SMSR $>$ 30 dB) in region C2 as required for SS-OCT. With these maps, it was experimentally found that the laser had a useful tuning range of $\approx$ 60 nm (Fig. 2.16c) at a center wavelength λ_c = 1540 nm and an average lasing power of 10 mW.

In order to study how the laser operates at different current combinations including the gain and phase, the SG-DBR laser was set to 27,000 different optical states using the same setup (Fig. 2.11). Each different optical state was obtained by combining the five input variables: BM (6-70, 2 mA step), FM (6-50, 2 mA step), phase (10-20, 2 mA step),

gain (100-150 mA, 10 mA step) and SOA (100 mA). With this approach the data analysis is simplified as the system can be considered as a black box with five inputs and two outputs. Such results are shown in Fig. 2.17.

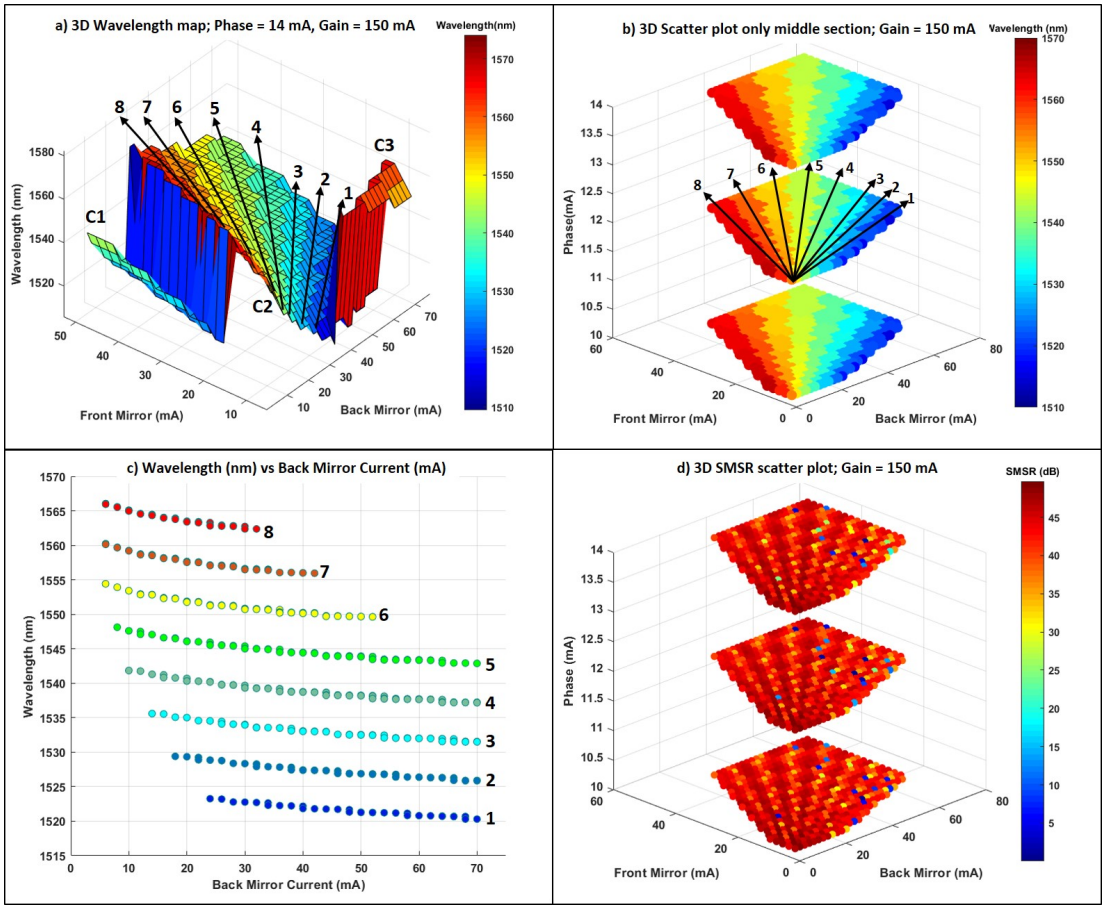

Figure 2.17: a) 3D wavelength surface plot. Phase = 14 mA; Gain = 150 mA b) 3D scatter plot at three phase levels (10-14, 2 mA step) with only C2 middle tuning region. Eight main tuning paths can be identified. c) Wavelength in nm as a function of BM current. Eight tuning paths are also identified. d) 3D SMSR scatter plot at three phase levels (10-14, 2 mA step).

Fig. 2.17a is a 3D surface plot that relates the wavelength as a function of the FM and BM currents. The same regions as well as the tuning paths are identified as in Fig. 2.16a. In order to cover each tuning path and obtain a linearly increasing wavelength, the

BM current has to be increased significantly up to its maximum value compared to the FM current. Once the end of the tuning path has been reached both currents have to be changed abruptly (Fig. 2.17b). Such a condition can affect the performance of the laser by creating discontinuities in the output wavelength because the electronic transition can trigger several modes in between as the laser is fast enough to respond to fast current changes (≈ 5 ns). After having an abrupt current change the laser needs time to stabilize and therefore a crucial design parameter is to have electronics that are fast enough to transition from a high to a low value of current with the least possible noise and current spikes. The quality of the optical signal can be preserved by using the SOA as an optical shutter so that the light is absorbed in such section during the transition. Fig. 2.17c,d show three wavelength and SMSR tuning maps of region C2 at three different phase levels. Wavelength fine tuning is achieved by stepping the phase current at small intervals (< 1 mA).

2.4.8 SG-DBR AC results

DC characterization provided a complete understanding of how the laser behaves as a function of the input currents. However, SS-OCT requires swept sources to be swept in orders of 100-200 kHz, hence AC dynamic characterization is required in order to know how stable is the instantaneous lasing wavelength, how repetitive are the wavelength sweeps and what current combinations are necessary to tune to laser in a linearly increasing way. AC characterization of the SG-DBR laser in terms of its lasing wavelength was performed with the setup shown in Fig. 2.11. The results are shown in Fig. 2.18, Fig. 2.19 and Fig. 2.20.

Fig.2.18 is a dynamic tuning map measured at 100 kHz (10 μs per current combination). Notice that its behavior is similar to its DC version (Fig.2.16) as three tuning regions are

identified, where the central region (C2) contains several tuning paths in linearly increasing wavelength. Despite their similarity, the AC characterization is completely necessary as it was experimentally observed that the laser has a hysteretic behavior, meaning that in order to reproduce the same tuning map it is required to follow the same tuning conditions in terms of sweeping speed, current steps, maximum currents and temperature. When such conditions were not fully met, different dynamic tuning maps were obtained.

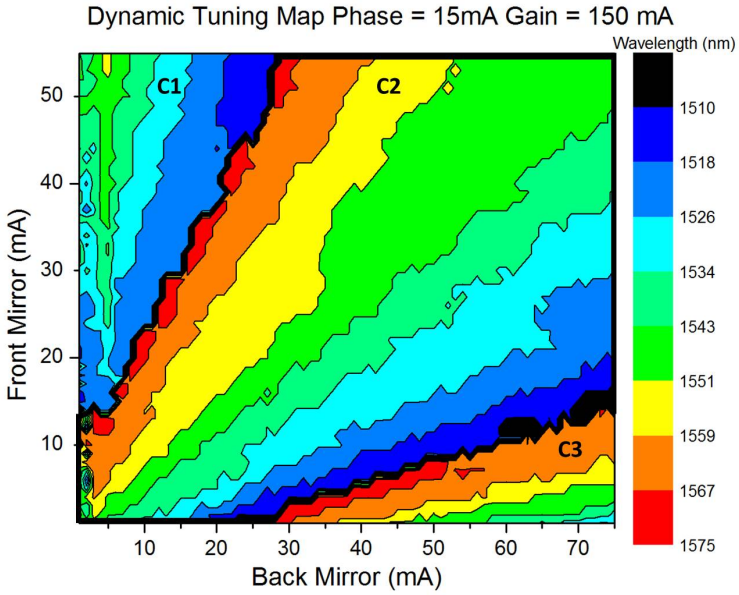

Figure 2.18: AC Dynamic Tuning Map measured at 100 kHz (10 μs per current combination)

Using the AC-RMS as a reference value to quantify the beating signal quality allowed determination of the lasing wavelength per current combination (Fig. 2.13), such results are shown in Fig. 2.19b and Fig. 2.20a-d. Instead of having a tuning map, a 3D scatter plot represents the wavelength as a function of the front and back mirror currents, where the color code is the calculated AC-RMS (red represents a better quality signal). These plots are very relevant as they present many similarities with the previously obtained DC maps (Fig. 2.17, Fig. 2.19a) Fig. 2.19b presents three main tuning regions, as previously found.

Each tuning path can also be identified, notice however this tuning path has a higher density of points to be chosen from, hence a computer program was written to select only one current combination per wavelength according to the following criteria:

1. Avoid abrupt current changes of bias current.
2. Choose points that are as close as possible to the center of the tuning paths and not at the edges in order to avoid mode hopping.
3. Choose points with a linear k-step ($2\pi/\lambda$).

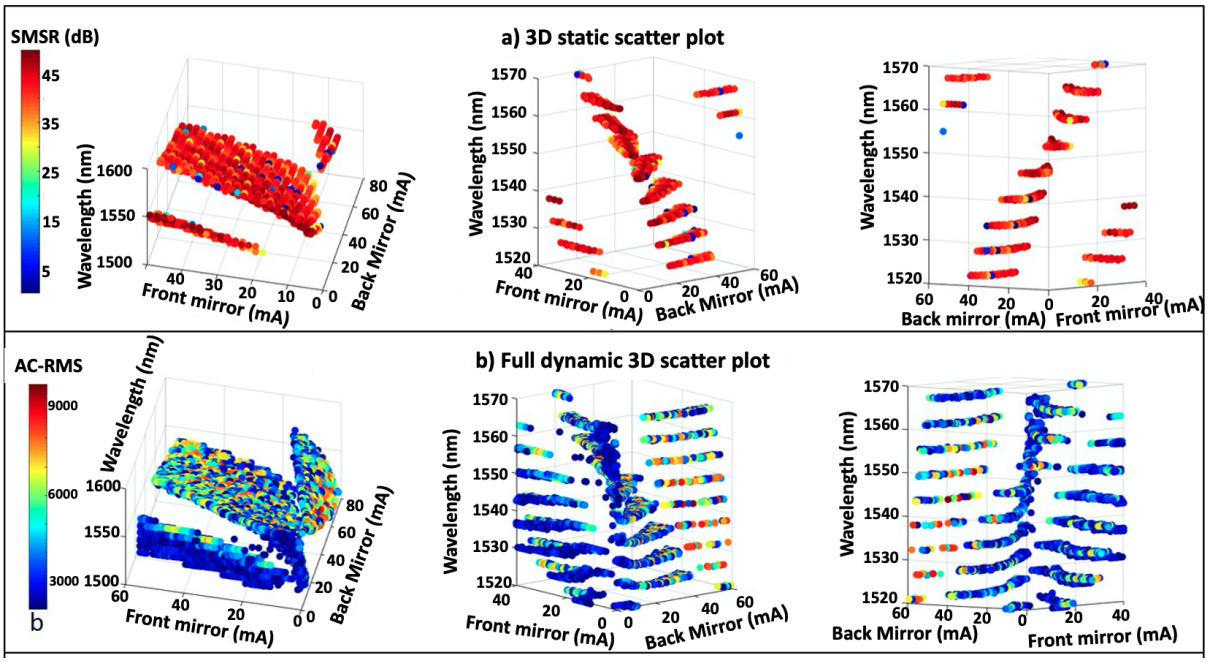

Figure 2.19: DC and AC characterization at 100 kHz (10 μs per current combination) a) 3D static scatter plot - colour bar represents the SMSR. b) Full dynamic 3D scatter plot with three tuning regions (7000 tuning points) - Colour bar represents the AC-RMS.

In order to meet the 1^{st} criteria only the points of the central region are kept (Fig. 2.20a, 3428 tuning points). With this point filtering, the only abrupt current changes that will happen is when going from the end of a tuning path, to the beginning of the next one. The following step is to choose only one current combination per wavelength, for this reason three solutions were proposed: Chose the points with the shortest path, maximum AC-RMS and remove the duplicate wavelengths (Fig. 2.20b-d, 379 tuning points).

The 1^{st} solution reduces abrupt current changes, however it was observed that the lowest AC-RMS quality points are chosen (blue points), not only that but there is a high density of current combinations for low currents which will cause mode-hopping. The 2^{nd} solution automatically chooses the highest quality AC-RMS between a group of points, there is also a high density of points for low values of current. The 3^{rd} solution removes all current combination duplicates and keeps only one. Most of the chosen points are neither the highest quality nor lowest quality point but an intermediate value. What can be observed from the three cases is that most of the dynamic tuning for this SG-DBR laser happens in a window of 20 mA for both FM and BM, hence the relevance of being able to produce current values as close as possible to the desired values and decreasing the electronic noise as much as possible. A 'tuning dictionary' is obtained with the chosen points. Such points are put into a list and the laser is swept with the chosen current combinations (379 tuning points).

2.5 Discussion and conclusions

This chapter gave an overview of the current up-to-date swept source technologies including commercial sources using different tuning mechanisms that provide several sweep repetition rates, sweep ranges, imaging depths and axial resolutions. The required application will determine which swept source is the most suitable. Additionally, multi-section

slotted lasers processed in-house as well as a tunable telecoms SG-DBR laser were optically and electronically characterized to determine their capabilities in becoming a swept source. The conclusions of the chapter are now discussed.

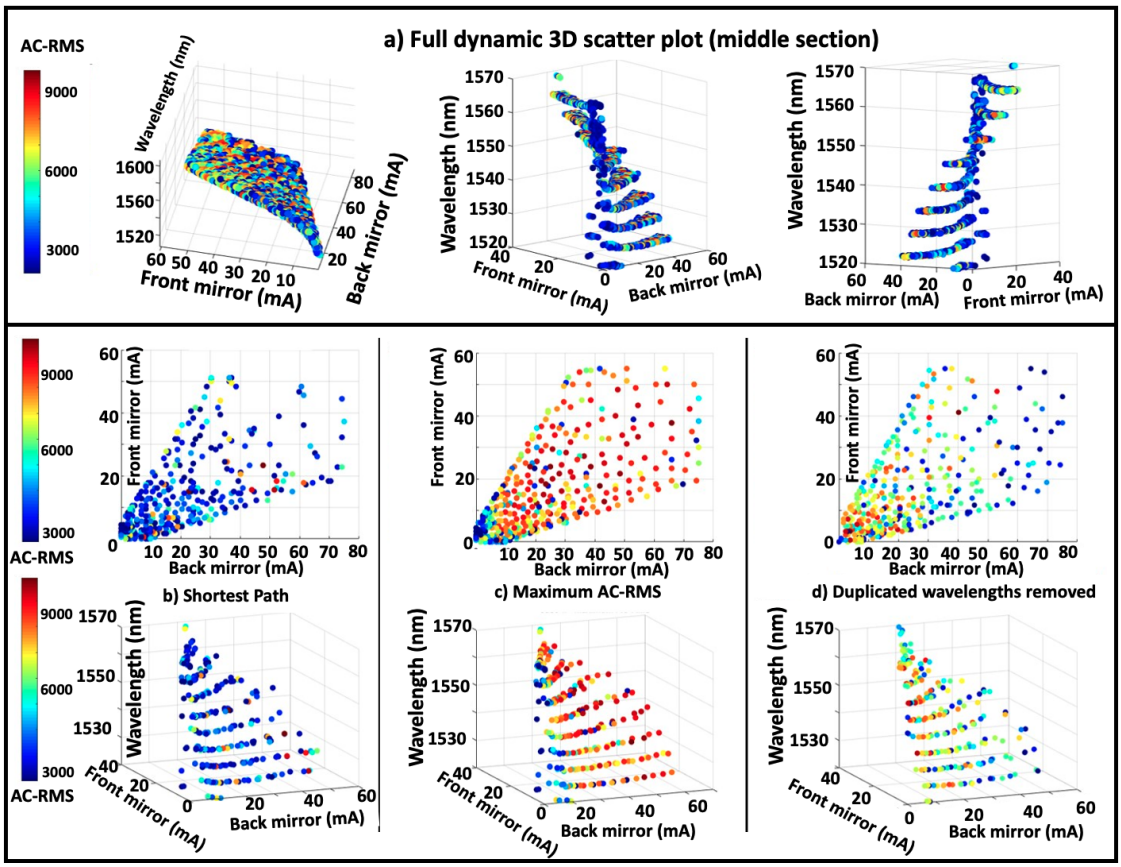

Figure 2.20: DC and AC characterization at 100 kHz (10 μs per current combination) a) Tuning points only from the middle region (3428 tuning points) b) Shortest Path (379 points) c) Maximum AC-RMS (379 points) d) Duplicated wavelengths removed (379 points)

2.5.1 Swept source requirements

The requirements for a swept source to be used as the core of an endoscopic OCT system are a fast sweep repetition rate of at least 200 kHz, a broad sweep range, a centre wavelength of 1300 nm and imaging depth in the mm range. This requirements are met by the Axsun swept source capable of providing an axial resolution of 10 μm in air, fast A-scan of 200 kHz and deep imaging depth of 10 mm. This source fulfills the requirements of optical power, sweep range and sweep repetition rate needed to assemble the endoscopic OCT probe. Signal synchronization has been achieved through the λ-trigger and k-clock for signal resampling.

2.5.2 Automated heterodyne method

DC characterization provided a broad understanding of the behavior of the tunable lasers allowing identification of the central tuning region as well as its tuning paths. It was also possible to determine the tuning range, central wavelength, SMSR, average lasing power and the lower and upper limits for the mirror tuning currents. An advantage of the proposed setup is that different tunable laser architectures can be characterized as the whole characterization process has been automated. Despite the broad picture given by the DC characterization it is absolutely necessary to perform the heterodyne/AC measurement of the laser. The final outcome of the heterodyne/AC characterization were tuning dictionaries which were then tested for linearity. One of the requirements of this setup is a laser with a stable lasing power as well as low noise levels, otherwise a beating signal cannot be discriminated from a noisy signal, hence providing incomplete tuning maps. Also, the setup requires a high-speed oscilloscope which might be expensive. For this reason a cheaper method using a linear filter as a one-shot characterization is proposed as an alternative to complement for the heterodyne method (Appendix A.2).

2.5.3 Multi-section slotted laser

Several multi-section slotted lasers were characterized. DC tuning maps were measured and 'fanlike' tuning maps were observed allowing the identification of clear tuning paths with a broad tuning range of 60 nm around a central wavelength of 1550 nm with an acceptable SMSR $>$ 30 dB. One drawback is the high level currents required as this increases the temperature of the device. Also, the 'fanlike' behaviour was observed at very slow tuning speeds which are not useful for OCT applications.

A dynamic AC tuning map was measured observing high amounts of noise per lasing wavelength, therefore clear tuning paths were not identified. One of the main reasons were optical power fluctuations when the laser was biased at constant DC levels. Therefore, when going to higher speeds the noise increases considerably affecting the characterization of the device. It was also noticed that the laser is highly sensitive to electric current noise, although this might be a good indicator of how fast is the laser, it adds a level of complexity to the control electronics requiring impedance matching and noise-free signals. Another reason for the poor AC performance is mode-hopping as observed when biasing only one of the mirror sections. The previous factors indicate that the difference between the DC and AC maps depends on the sample rate at which currents are produced as the laser is highly sensitive to input currents. Solutions to the discussed limitations include:

- Adding anti-reflection (AR) coatings to the laser in order to avoid undesired light reflections.
- Manufacture new lasers considering different edge and slot spacing since the slot profile has a major impact on the device performance as a single mode tunable source.
- Increase the DAQ resolution to have the smallest current step with low noise.

- Design a printed circuit board with corresponding matching impedance.

Despite the challenges for slotted lasers these have the advantages of being a single chip laser with standard materials, and foundry compatible process technology. The cost of such a laser is then equivalent to present telecoms lasers, which can be individually purchased for about 1,000€.

2.5.4 SG-DBR laser

Invalid points in the sweep and large stitching noise were two important limitations that need to be compensated in order to use the SG-DBR laser as a swept source. Invalid points in the sweep were observed when the instantaneous lasing wavelength drifted from the expected value. E.g, the instantaneous lasing wavelength for the shortest path and maximum AC-RMS deviated from the expected value for certain current combinations. A solution to replace the invalid points is to use this point as a 1^{st} reference, replace it with a neighboring value, reproduce the sweep and observe the wavelength stability. This process shall be repeated until a stable point is found.

Large stitching noise and large amounts of optical noise were associated with abrupt changes in injection currents, especially when going from the end of one tuning path to the start of the following one, hence reducing the quality of the linear sweep since undesired wavelengths affect the quality of an OCT image. Such behavior is due to the mode-hopping of the laser as the injection currents abruptly change from one set to a completely different one. A solution to limit the stitching noise is to add a feedback loop to know the instantaneous lasing wavelength. When mode-hopping is detected in the laser, the feedback loop shall compensate it by dynamically changing the input currents of the laser in order to stabilize the lasing wavelength. When implementing this solution, one has to be careful of properly designing the control system, otherwise the system can become unstable. Other adverse effects are due to the high density of points in the lower

left window of the tuning paths (thus being sensitive to electronic noise) and when one current combination is too close to the border of a tuning path. This effect was observed as unstable instantaneous wavelengths.

A relevant observation during the dynamic tuning of the laser was that the quality and stability of the instantaneous wavelength was highly dependent on the previous optical state, hence when the same path was reproduced the signal quality was improved compared to choosing the same current combination but having different previous optical states. Such behavior is due to the hysteresis of the laser. A solution to this problem is to use the tuning dictionary as a reference/starting point and then fine tune the values of the currents in order to find a path with better optical performance; such a process is then repeated until a stable configuration is obtained. This process was tested with the tuning dictionary by selecting alternatives from the duplicate wavelengths. This improved performance but the lasing wavelength was still unstable when changing from one tuning path to another.

In order for the SG-DBR laser to become the swept source for a SS-OCT several considerations have to be taken into account: The laser sections are sensitive enough to detect electric noise coming from the control electronics, therefore when the laser is operating near the border of two tuning regions unstable mode-hopping is present. This behavior can be compensated by choosing points closer to the center of the tuning paths and can be practically accomplished by adding a feedback loop of the wavelength in order to fine tune the phase section to obtain the desired wavelength. This concept can also be applied during the transition of abrupt current changes and control of the current in the SOA so that instead of letting the laser light being transmitted it is absorbed. Another relevant parameter to have a stable linear sweep is the temperature of the device. Different current densities being injected to the semiconductor structures at high speed rates produces different local temperatures per section, the section with the highest temperature will

change the temperature of the adjacent section, hence when reproducing a tuning dictionary the temperature has to be the same as when it was firstly measured, otherwise the lasing wavelength will not be as expected. In this setup, the temperature of the SG-DBR laser was only controlled with the TEC.

2.5.5 Relevance of akinetic tunable laser sources

The possibility to develop low-cost OCT is a clear market opportunity, and essential for the future commercial viability. Currently, the high cost of an OCT comes from the swept source price that vary between approx. 17,000 to 58,000 €. Swept sources have undoubtedly become a crucial element in OCT in order to acquire images with high quality at fast imaging rates. These, however are expensive compared to conventional SLED sources of SD-OCT, hence, long term cheaper solutions based on akinetic all-semiconductor sources are still required.

For akinetic swept sources, the main cost is due to the significant time that has to be invested in their characterization in order to find the correct tuning maps. Additionally, the control electronics need to be high-speed (GHz range). Despite their complexity these sources provide a narrow linewidth, small dimensions, can produce its own k-clock and are software controllable. This last feature provides deep imaging depths with custom sweep patterns. Finally, the wafer-scale production of all-semiconductor tunable lasers shall reduce the overall cost of the swept source.

In order to reproduce a linear sweep useful for SS-OCT one most consider the high number of control variables per semiconductor section, its sensitivity and the hysteresis of the laser. Also, precise electronics are required in order to avoid mode-hoping and long current transitions between tuning paths. Research in the area of akinetic swept sources is highly relevant to continue the development of endoscopic OCT with the ultimate goal of reducing the price of the overall OCT system and providing high quality OCT images.

Chapter 3

Optical coherence tomography

3.0.1 Review of background material

Optical Coherence Tomography (OCT) has become a main medical imaging modality due to its fast acquisition of cross-sectional images. This has been possible due to the combination of swept sources, light interferometers, fast signal acquisition electronics and scanning mechanisms. The first step to design an OCT system is understanding that its core is a light interferometer, hence it is relevant to define a solid mathematical foundation to describe how to acquire a spectrally resolved interference pattern. For this reason, this chapter begins by introducting the mathematical and physical foundations of OCT. The definition of OCT is discussed in Sect. 3.1 in terms of signal in k-space (3.1.1), multiple interface samples (3.1.2), signal in Fourier Space (3.1.3), axial and lateral resolution (3.1.4), signal sampling (3.1.5), dispersion compensation (3.1.6) and noise analysis (3.1.7).

3.0.2 Contributions to the field

Once the mathematical foundation has been laid out, the following step is to implement an OCT setup composed of several optical elements such as optical fibres, splitters, photodetectors and a swept source. For OCT to be translated into a clinical setup, all of the optical elements have to be integrated in a compact way. For such reason the following

original contributions are made:

1. **A novel SS-OCT system using a multi-modal interferometer with double-clad fibres** (Sect. 3.2). The design, integration and assembly of a SS-OCT is presented. This system is fibre-based and proposes the use of double clad fibres to collect the OCT signal using the core and an additional imaging signal, such as fluorescence or multi-photon tomography (MPT), using the cladding. The signals are combined using an interferometer box that allows easy integration into a clinical setting.

2. **Dispersion compensation algorithm**. OCT uses already existing numerical dispersion compensation algorithms. In this chapter a modification of such algorithms is presented in order to compensate a whole set of B-scans allowing image correction for an entire image dataset. The implementation requires the computation of the Hilbert transform to correct to a linear phase. This algorithm is presented in Sect. (3.1.6) and the results are shown in Sect.3.3.

3. **Scanning mechanisms.** Two different types of scanning mechanisms were developed (Sect. 3.3). The first one uses a **translation stage** to obtain an ample field of view of 100 mm x 40 mm allowing imaging of longer ex-vivo samples (3.3.1) The second scanning mechanism uses a **piezo-tube (PZT) fibre-tip cantilever** to form an endoscopic probe that can be integrated into a conventional endoscope (3.3.2). The novelty of this probe is its fast acquisition B-scan speed of 1.4 kHz that compensates for moving motion as well as increased sampling density with **an original interleaving algorithm** that improves image quality. Finally discussion and conclusions are presented in Sect.3.4

3.1 Optical Coherence Tomography definition

Optical Coherence Tomography (OCT) is capable of creating cross-sectional and volumetric images of biological samples with a micrometer resolution (1-10 μm) for up to one to two millimeters in depth. This is accomplished by using a light interferometer that measures the time-of-flight or light reflections between backscattered light from a sample and a reference mirror. The measured signal is a spectrally resolved sinusoidal interference pattern. For swept source OCT (SS-OCT) [102, 103, 104, 105, 106, 107], the light source is known as a swept source or rapidly tunable laser source since a narrow wavelength, with long coherence length, is rapidly tuned over a large optical bandwidth[108]. A representation of the optical spectrum as function of time is shown Fig. 3.1.

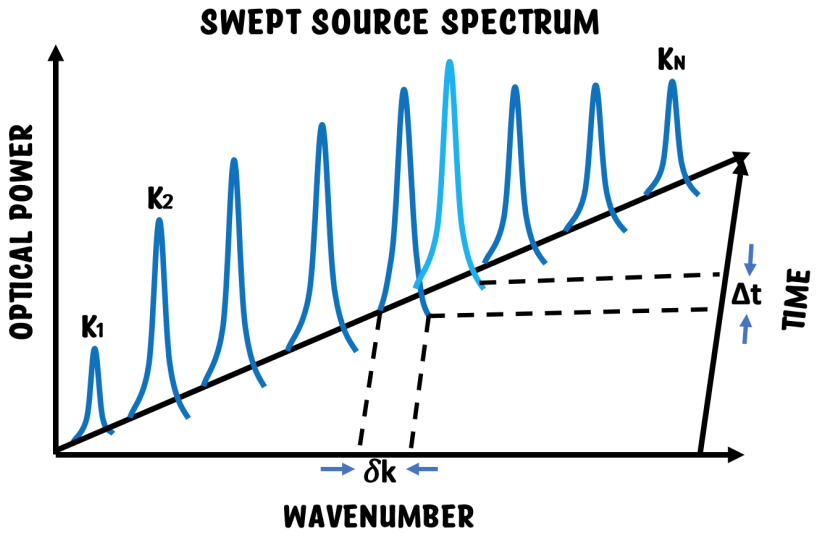

Figure 3.1: Swept source spectrum. A wavelength sweep is performed with individual optical bandwidth δk over the time window Δt. Redrawn from [108].

Two important parameters are defined: Δt is the single detector sampling time and δk is the narrow optical bandwidth. SS-OCT generates a spectrally resolved interference pattern where a narrow optical bandwidth δk, with a long coherence length on the mm range, is measured sequentially in time Δt using a balanced photodetector. It is then

the backscattered light coming from different depth regions of the sample, within this coherence length, that will interfere with the reference light at the detector and will form the spectral interference pattern. The spectral interference pattern encodes the depth-resolved structure in its spectral frequency content. The depth structural features are retrieved from reflectivity profiles along the depth of the sample and are obtained for a multitude of wavelengths separately. This is accomplished by Fourier transforming the interference pattern in order to obtain the axial structure of the sample defined as **A-scan**. The following subsections describe the previously mentioned steps to acquire an A-scan.

3.1.1 OCT signal in k-space

In order to obtain better axial resolution for the A-scan, the interference pattern must be linearly spaced in wavenumber k (k-space) and not in wavelength λ[109]:

$$k = 2\pi/\lambda \tag{3.1.1}$$

A following Fourier transform is computed for an interference pattern linearly sampled in k-space in order to calculate a reflectivity depth profile in z-space. These depth profiles are defined by the spectral content generated by swept source. Hence the Fourier transform is the mathematical operation that links the z-k domain[110].

The interference pattern is generated with a light interferometer. Its optical elements are a swept source with a spectral intensity distribution $S(k)$, a beamsplitter, and sample and reference arms. A setup including these elements is shown in Fig.3.2a. The light from the swept source is split by a beamsplitter characterized by a reflection coefficient α and transmission coefficient $1 - \alpha$. The beamsplitting creates two arms, reference and sample[111].

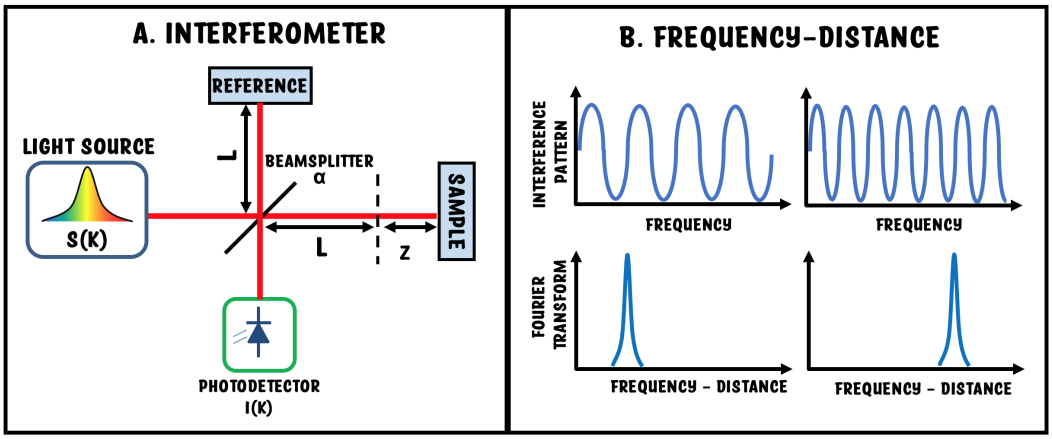

Figure 3.2: Optical interferometer. A) Interferometer composed of a swept source $S[k]$, reference and sample arms and a photodetector detecting signal I[k]. B) Frequency-distance relationship as a function of the optical delay of the interferometer.

For the reference arm, the light travels a total distance $2L$ as reflected by the reference arm mirror. The light goes through the beamsplitter and then reaches the detector. For the sample arm, the light travels the same distance $2L$ plus an additional distance 2z and is then backscattered to the detector. Only light that travels approximately the same optical distance defined by the coherence length of the source creates an interference pattern observed as interference fringes[112]. In practical terms, interference will only be measured between electric fields whose frequency difference Δf is within the bandwidth of the detector.

The distance where both arms have equal optical lengths is defined as the **zero-delay** point, which is the reference distance for the interference pattern. When the optical path difference is close to the zero delay, an oscillating interference pattern with a low frequency is generated. Its Fourier transform is a δ-function with a peak closer to the zero delay point. On the contrary, as the optical path difference increases, the interference pattern will have a faster oscillating frequency which is translated to Fourier space as a right-shift away from the zero delay (Fig. 3.2b). The previous holds for a perfect reflector with a single interface and a dispersion-free system.

3.1.2 OCT signal of a multiple interface sample

Biological samples, including biological tissue, have more than one single interface. Hence, these are modeled by a **depth-dependent** electric field reflectivity along its sample beam axis $r_s(z_s)$, for z_s the path length in the sample arm. This sample with N reflective interfaces is modeled as a summation of real delta-functions [113]:

$$r_S(z_s) = \sum_{n=1}^{N} r_{sn}\delta(z_S - z_{Sn}) \tag{3.1.2}$$

The $n-th$ reflection has a reflectivity r_{sn}, and path length z_{sn}. The power reflectivity of the sample is obtained as $R_{S1} = |r_{S1}|^2$. With this, it is then possible to reconstruct the function $\sqrt{\mathbf{R_s(z_S)}}$, **which is the desired reflectivity profile of the sample as a function of depth along the beam axis**. In order to obtain this reflectivity profile, a sample with N reflective surfaces is placed in the sample arm of the interferometer of Fig. 3.2a. Additionally, consider a beam splitter with even split ratio, a reference mirror with electric field reflectivity r_R and an input broadband light source as shown in Fig. 3.3.

The light source is modeled as a plane wave propagating along z with its electric field expressed as [113]:

$$E_i = s(k,\omega)e^{i(kz-\omega t)} \tag{3.1.3}$$

where $s(k,\omega)$ is the amplitude of the complex electric field as a function of the wavenumber $k = 2\pi/\lambda$ (spatial frequency) and angular frequency $\omega = 2\pi\nu$ (temporal frequency) of each spectral component, where $c/n(\lambda) = \lambda\nu$, and *c* is the vacuum speed of light. The incoming plane wave E_i is evenly split into the reference and sample arm. For the reference arm, a perfect reflective mirror with electric field reflectivity r_R, power reflectivity R_R = r_R^2, and a distance from the beam splitter to the mirror of z_R is considered. The reference plane wave after double pass ($2z_R$) is given by [113]:

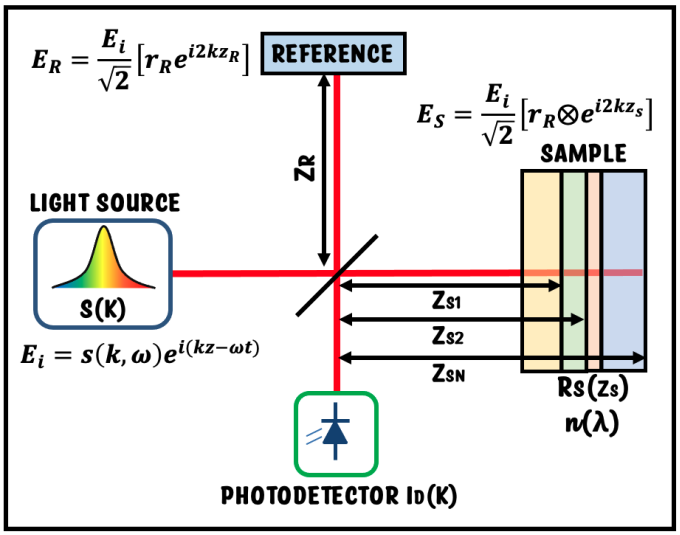

Figure 3.3: Interferometer setup. The light source produces the electric field E_i which is split into reference and samples fields E_R and E_s. A sample with multiple interfaces is considered. Interference pattern is detected at the photodetector. Redrawn from [113].

$$E_R = \frac{Ei}{\sqrt{2}} r_R e^{i2kz_R} \tag{3.1.4}$$

The electric field returning from the sample is defined as:

$$E_S = \frac{E_i}{\sqrt{2}}[r_S(z_S) \circledast e^{i2kZ_{Sn}}] \tag{3.1.5}$$

where the convolution operator $\circledast$ includes the individual contributions of the sample electric field reflectivities r_{sn}. Considering N reflectors, the incident electric sample field on the beam splitter is:

$$E_S = \frac{E_i}{\sqrt{2}} \sum_{n=1}^{N} r_{Sn} e^{i2kz_{Sn}} \tag{3.1.6}$$

Both fields, E_R and E_S, return to the beam splitter and are then directed to the photodetector where the fields interfere with the power reduced to its half. A photocurrent proportional to the square of the sum of both electric fields is generated:

$$I_D(k,\omega) = \frac{\rho}{2} < (E_R + E_S)(E_R + E_S)^* > \tag{3.1.7}$$

$$I_D(k,\omega) = \frac{\rho}{2}\left\langle \left| \frac{s(k,\omega)}{\sqrt{2}} r_R e^{i(2kz_R - \omega t)} + \frac{s(k,\omega)}{\sqrt{2}} \sum_{n=1}^{N} r_{Sn} e^{i(2kz_{Sn} - \omega t)} \right|^2 \right\rangle \tag{3.1.8}$$

Where ρ is the responsivity of the photodetector (Amperes/Watt) and the brackets represent the time integration of the detector. The time dependence $e^{i\omega t}$ of the electric field is neglected as the electric field oscillates much faster compared to the response time of the detector. Substituting for E_R (3.1.4) and E_S (3.1.6) outputs three main terms:

$$I_D(k) = \frac{\rho}{4}[S(k)[R_R + R_{S1} + R_{S2} + ...]] \text{ DC terms} \tag{3.1.9}$$

$$+ \frac{\rho}{2}[S(k) \sum_{n=1}^{N} \sqrt{R_R R_{Sn}} cos[2k(z_R - z_{Sn})]] \text{ Cross-correlation terms} \tag{3.1.10}$$

$$+ \frac{\rho}{4}[S(k) \sum_{n \neq m=1}^{N} \sqrt{R_{Sn} R_{Sm}} cos[2k(z_{Sn} - z_{Sm})]] \text{ Auto-correlation terms} \tag{3.1.11}$$

Where $S(k)$, R_R, R_S, z_R, z_S are the spectral density of the incoming plane wave, reference power reflectivity, sample power reflectivity, distance from the beam splitter to the mirror and the sample, respectively. Three main terms are identified in the previous expression, a DC term, cross correlation and autocorrelation:

- **DC terms** are independent of the path differences and are measured as an offset added to the detector photocurrent. Its amplitude is defined by the sum of the reference and sample power reflectivities[114].

- **Cross-correlation** is the desired interference pattern. This is proportional to the square root of the product of the reference and sample power reflectivities as well as being dependent on wavenumber and path differences between the reference mirror and the sample reflectivities (z_R - z_{Sn}). A cosine function modulates the source spectrum proportionally to the distance between the reference and the sample[112].
- **Autocorrelation** relates the interference between different sample power reflectivities and their separation distance, creating undesired artifacts[115, 116].

The previous three terms defined the interference pattern. The source spectrum is modulated by multiple cosine patterns with a modulation frequency defined by the optical path difference between the reference and sample arms. The modulated amplitude depends on the power reflectivity of the reference mirror and the sample. For SS-OCT the DC and autocorrelation terms are suppressed using a balanced detector[114].

3.1.3 OCT signal in Fourier-Domain (z-space/A-scan)

The sample reflectivity profile $\sqrt{R_S(z_s)}$ is obtained by calculating the inverse Fourier transform of $I_D(k)$, which goes from wavenumber, *k-space*, to physical distance, *z-space*. Using the FFT pair $\frac{1}{2}(\delta[(z+z_0)]+\delta[(z-z_0)]) \longleftrightarrow cos(kz_0)$, the inverse FFT of equations (3.1.9,(3.1.10),(3.1.11) yields[115]:

$$i_D(z) = \mathscr{F}_k^{-1}[I_D(k)] = \frac{\rho}{8}[\gamma(z)[R_R + R_{S1} + R_{S2} + ...]] \text{ DC terms} \tag{3.1.12}$$

$$+ \frac{\rho}{4}\Big[\gamma(z) \circledast \sum_{n=1}^{N} \sqrt{R_R R_{Sn}}(\delta[(z \pm 2(z_R - z_{Sn}))])\Big] \text{Cross-correlation terms} \tag{3.1.13}$$

$$\frac{\rho}{8}\Big[\gamma(z) \circledast \sum_{n\neq m=1}^{N} \sqrt{R_{Sn} R_{Sm}}(\delta[(z \pm 2(z_{Sn} - z_{Sm}))])\Big] \text{Auto-correlation terms} \tag{3.1.14}$$

where $\gamma(z) = FT^{-1}(S(k))$. The multiplication operations in k-space are equivalent to a convolution operation, denoted by $\circledast$. This operation expresses the OCT intensity signal in z-space and is defined as the axial point spread function (PSF) convoluted with the sample reflectivity. Therefore, the power reflectivity profile is obtained by performing the corresponding convolution operations [115]:

$$i_D(z) = \frac{\rho}{8}[\gamma(z)[R_R + R_{S1} + R_{S2} + ...]] \text{ DC terms} \tag{3.1.15}$$

$$+ \frac{\rho}{4}\sum_{n=1}^{N}\sqrt{R_R R_{Sn}}[\gamma[2(z_R - z_{Sn})] + \gamma[-2(z_R - z_{Sn})]] \text{ Cross-correlation terms} \tag{3.1.16}$$

$$+ \frac{\rho}{8}\sum_{n\neq m=1}^{N}\sqrt{R_{Sn} R_{Sm}}[\gamma[2(z_{Sn} - z_{Sm})] + \gamma[-2(z_{Sn} - z_{Sm})] \text{ Auto-correlation terms} \tag{3.1.17}$$

Notice that the sample field reflectivity profile is found in the cross-correlation terms, however, expressed as [115]:

$$\sqrt{R_s(z_s)} = \sum_{n=1}^{N}\sqrt{R_{Sn}}\delta[(z_R - z_{Sn})] \tag{3.1.18}$$

The reflectivity profile (Eq. 3.1.18) is the basic building block of an OCT image which is termed as **A-scan**. An example of an A-scan is shown in Fig. 3.4. Several observations are made:

1. The reference distance for the zero delay is given by the position of the reference mirror z_R.

2. The δ-function is not a perfect infinite impulse but is broadened as determined by the width of the coherence length of the source $\gamma(z)$. This defines the point spread function (PSF) of the imaging system.

3. A broadband source with a long tuning range is needed to increase the resolution of the reflectivity profile as the spectral bandwidth defines the axial imaging resolution.

4. The amplitude of the sample reflectivity is amplified by reference reflectivity $\sqrt{R_R}$.

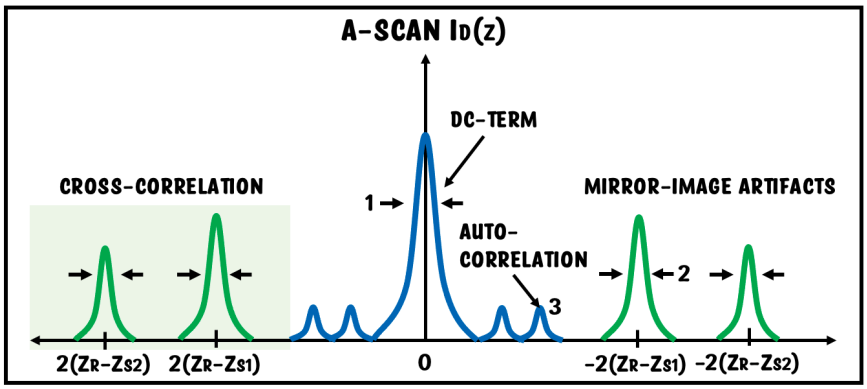

Figure 3.4: A-scan terms including DC, auto-correlation and cross-correlation as well as their mirror image artifacts. The DC term is present at the zero delay (1). The width of (2) corresponds to the axial resolution Δz. The side lobes (3) are the autocorrelation terms. Redrawn from [113].

Three image artifacts are to be considered:

1. *Complex conjugate artifact.* Due to the symmetry of the Fourier transform (real signal) there is a mirror image of $\sqrt{R_S(z_s)}$ on opposite sides of the zero delay position. This is compensated by showing only either positive or negative spectrum of the sample[117].

2. *DC term.* It adds an offset to the signal at the zero delay point.

3. *Autocorrelation terms.* These are observed as side lobes that add to the floor noise. To compensate for this, one must increase the reference intensity reflectivity so that the autocorrelation terms are small compared to the DC and cross-correlation terms.

3.1.4 Axial and lateral resolution

Unlike microscopy, where both lateral and axial image resolution depend on the spot size and numerical aperture (NA) of the optics, the axial and lateral resolution in OCT are decoupled. The spectral content or wavelength sweep range of the light source, which is independent of NA, determines the axial resolution. In the case of a Gaussian spectral shape, the **axial resolution** is defined as [118]:

$$\Delta z = \frac{2ln2}{\pi}\frac{\lambda_0^2}{\Delta\lambda} \tag{3.1.19}$$

Where λ_0 is the center wavelength of the light source and $\Delta\lambda$ the wavelength bandwidth. A shorter center wavelength and broader spectral content of the light source improve the axial resolution. The **lateral resolution** is defined as:

$$\Delta x = \frac{4\lambda}{\pi}\frac{f}{D} \tag{3.1.20}$$

where f is the focal length of the objective lens and D the diameter of the incident beam or the entrance pupil. A better transverse resolution is achieved with higher NA. However, there is a trade-off between high transverse resolution and depth of field or confocal parameter $b = 2z_R$, z_R is the Rayleigh range. The confocal parameter b is defined as [118]:

$$b = \frac{\pi\Delta x^2}{2\lambda} \tag{3.1.21}$$

Fig. 3.5 illustrates the mentioned trade-off. At high NA, there is a highly divergent beam with a reduced focal spot size obtaining a lower collection efficiency at large depths, hence there is a shallower depth of field with better lateral resolution. For low NA, the focal spot size is increased obtaining a collection efficiency that remains moderately constant within 'b', however with a reduced lateral resolution. The confocal parameter is much larger than the axial resolution $b > \Delta z$.

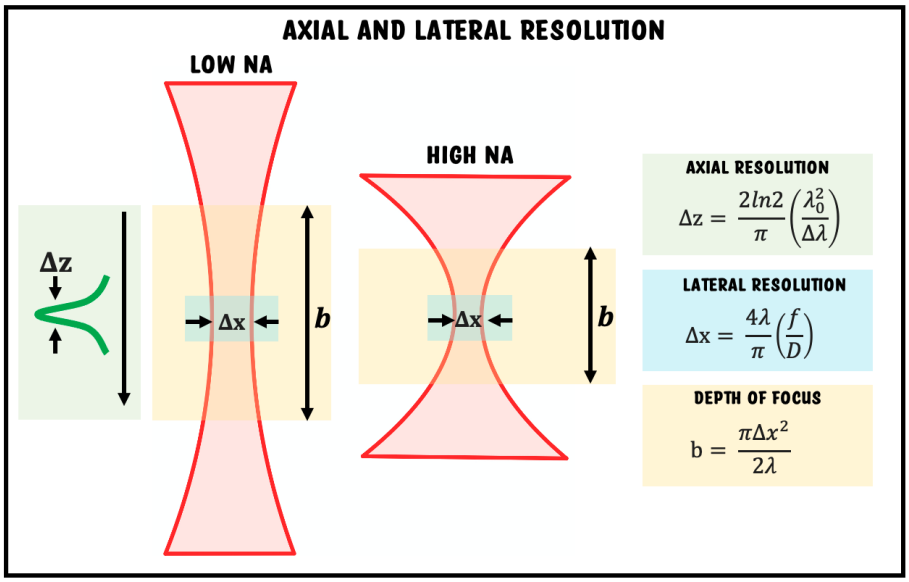

Figure 3.5: Axial and lateral resolution. The axial resolution depends on the parameters of the swept source, while the lateral resolution depends on the NA of the imaging lens. The trade-off between lower and higher NA is defined by the depth of focus parameter[118].

3.1.5 Signal sampling and k-resampling

For a real OCT setup the interference pattern is sampled and digitized for further post-processing in the computer. This is accomplished by connecting the electronic signal output of the balanced photodetector to a electronic digitizer. The digitizer samples the interference pattern as determined by the timing provided by an electronic clock. Depending on the digitizer, the clock may either be synchronous or asynchronous in time.

For the synchronous case, an internal clock source is used to obtain a signal that is evenly spaced in time t. This, however, requires a 2^{nd} processing step known as k-remapping, a process that can be done either by hardware during signal acquisition or by software postprocessing using signal interpolation algorithms. This is required to have a signal that is evenly spaced in k-space prior to Fourier transforming[116, 119]. For the asynchronous case, an external k-clock triggers the data acquisition, hence the signal will be evenly sampled in k-space as required. For the particular case of the presented OCT,

the asynchronous case is used by connecting the generated k-clock coming from the laser (section 2.3.1). For SS-OCT, the sampling of the interferogram creates a multitude of OCT depth scans separated by $z = \pi/\delta k$. Hence the maximum imaging depth in the OCT signal is defined by [120, 111]:

$$z_{max} = \frac{\pi}{2\delta k} = \frac{\lambda^2}{4\delta\lambda} \tag{3.1.22}$$

The maximum imaging depth is determined by the instantaneous linewidth of the tunable source, hence the importance of designing swept sources with narrow linewidth in order to obtain deep imaging in the mm range.

3.1.6 Dispersion compensation

One of the factors that affects the axial resolution of the OCT is the dispersion of the system[121, 122]. Dispersion is an effect caused by the wavelength dependency on refractive index of the optical components $n = n(k)$, hence each wavelength travels at different speeds causing an out of phase detection. This means that the axial resolution of the OCT will worsen as the FWHM of the axial resolution will be broader. In order to obtain the best performance of the axial resolution over the full imaging depth, one must perform dispersion compensation, which consists in matching the dispersion in both arms of the interferometer. Hardware dispersion compensation can correct both the system and sample dispersion by physically matching the dispersion in both arms by adding compensating materials[123] using gratings[124], fiber-stretchers[125], prisms[126], between others. Considering the refractive index as a function of wavenumber and depth $n = n(k, z)$, the spectral information $I_D(k)$ contained in the cross-correlation term of Eq. 3.1.10 can be redefined as [127]:

$$I_{int}(k) = \frac{1}{2}\rho(k)S(k)\sqrt{R_R(k)}\int r_s(\Delta z)\cos\Big(2k\Delta z + \Delta\theta(\Delta z)\Big)d\Delta z + \Delta\Phi_{disp}(k) \tag{3.1.23}$$

Where $\rho(k)$ is the detector responsivity, $S(k)$ the spectral power of the incoming light source, $R_R(k)$ the power reflectivity of the reference arm, $r_S(\Delta z)$ the magnitude of the sample field reflectivity, $\Delta\theta(\Delta z)$ the phase of the sample field reflectivity and $\Delta\Phi_{disp}(k)$ is the dispersion mismatch between sample and reference arms. Notice the k dependence of $\Delta\Phi_{disp}(k)$. The term $\Delta\Phi_{disp}(k)$ is a wavelength dependent phase proportional to the refractive index mismatch $n_S(k) - n_R(k)$. Therefore, the spectral components of the broadband light travel at different speeds dispersing the light worsening the axial resolution. This is caused by a broadening of the cross-correlation interferogram, signal peak decrease, and increase in coherence length. Numerical dispersion compensation was performed in this thesis as shown in Fig. 3.6. This was accomplished by:

1. Acquiring a raw set of B-scans.
2. Computing the DFT and then applying a rectangular window using the iFFT.
3. Calculate the correction factor θ_{CURVE} by phase unwrapping and linear fit.
4. Retrieving the envelop and phase unwrapping of a B-scan using the Hilbert transform.
5. Correct the phase by $\theta_{CORR} = \theta_{HIL} - \theta_{CURVE}$
6. Reconstruct the A-scan by $A = |H\{I\}|e^{i\theta_{CORR}}$

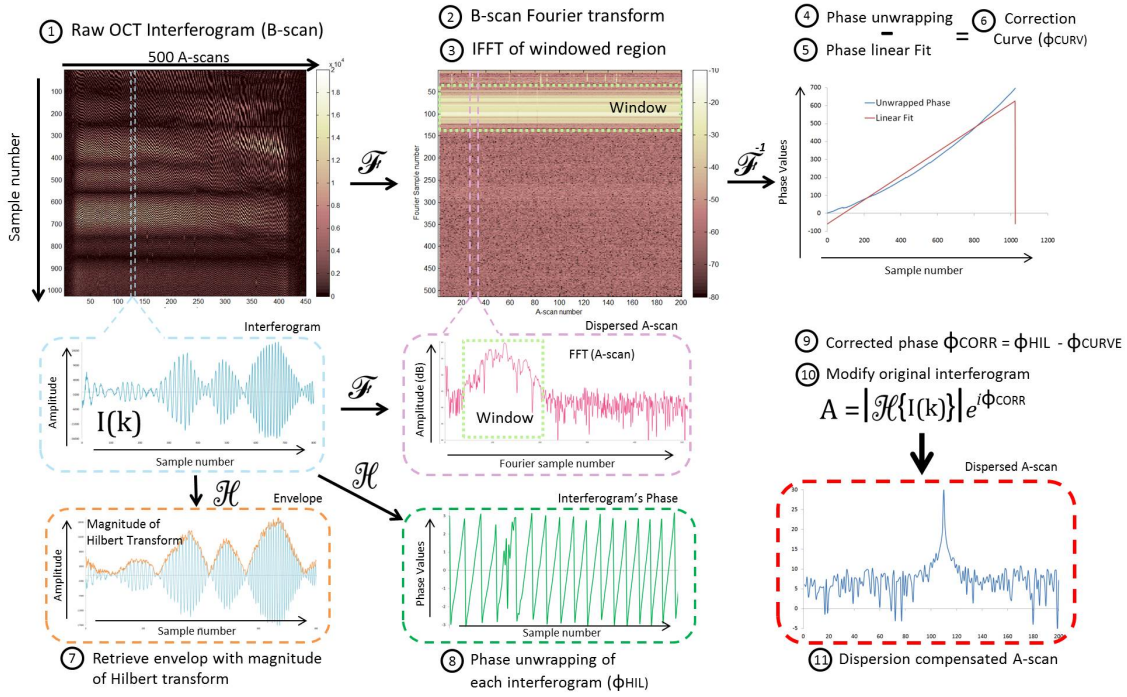

Figure 3.6: Dispersion compensations steps. 1) Acquire raw B-scans. 2) Compute the FFT of the B-scan 3) Apply the iFFT in a windowed region. 4) Unwrap the phase. 5) Linearize the phase. 6) Calculate the correction curve. 7) Retrieve the envelop with the magnitude of the Hilbert transform. 8) Unwrap the phase of each interferogram. 9) Calculate the corrected phase. 10) Modify the original interferogram. 11) Obtain the dispersion compensated A-scan. The applied Scilab code can be found in A.3.

3.1.7 OCT SNR

A key advantage of SS-OCT is the improved sensitivity Σ compared to TD-OCT coming from noise reduction hence increasing the Signal-to-Noise Ratio (SNR)[128, 129, 130]. The improved sensitivy and SNR comes from detecting the reflectivity profile as a function of wavenumber. Sensitivity Σ is defined over the smallest detectable back-scattered sample arm signal $R_{s,min}$, for which SNR is equal to 1 [26]:

$$\Sigma = 1/R_{s,min} \tag{3.1.24}$$

Sensitivity defines the minimum detectable reflected optical power compared to a perfect reflector, i.e., the weakest signal that can still be measured. Detection sensitivity decreases as a function of imaging depth, defined as roll-off. The roll-off is determined by the instantaneous linewidth and the detection bandwidth of the photodetector and digitizer. The SNR is the quotient of the average squared signal divided by noise variance [26]:

$$SNR =< I^2 > /\sigma^2_{noise} \tag{3.1.25}$$

The noise sources for SS-OCT are shot noise, relative intensity noise (RIN) and thermal noise. The best SNR is obtained at the shot noise limit, e.g., $\sigma^2_{shot} >> \sigma^2_{th} + \sigma^2_{RIN}$. For SS-OCT, this is mainly defined by the source RIN and RIN suppression by the balanced detector. The shot noise is generated due to the random arrival of photons at the detector. The SNR at shot noise limit is defined as [26]:

$$SNR^{shot}_{ss} = \frac{\eta P_{sample} \Delta t N}{E_\nu} \tag{3.1.26}$$

Where η is the quantum efficiency, P_{sample} is the sample arm power, Δt the single detector sampling time, $E_\nu = h\nu$ the photon energy at optical frequency ν with h Planck's constant and N related to the optical bandwidth by $\Delta k = N\delta k$. This definition holds for $P_{ref} >> P_{sample}$ and for the case of shot noise limited detection accomplished by using balanced detection to suppress the RIN noise.

3.1.8 Summary

The first half of this chapter has presented the mathematical definitions of the parameters that define the performance of the SS-OCT system. These include the narrow optical bandwidth Δk, the detector sampling time Δt, the axial resolution Δz, the lateral resolution Δx, the confocal parameter b, the imaging depth z_{max}, dispersion compensation and SNR. A summary is shown in Table 3.1:

Table 3.1: Summary of factors determining the performance of the SS-OCT system.

Narrow optical bandwidth	Δk	Detector sampling time	Δt
Axial resolution	$\Delta z = \frac{2ln2}{\pi}\frac{\lambda_0^2}{\Delta\lambda}$	Lateral resolution	$\Delta x = \frac{4\lambda}{\pi}\frac{f}{D}$
Confocal parameter	$b = \frac{\pi\Delta x^2}{2\lambda}$	Imaging depth	$z_{max} = \frac{\lambda^2}{4\delta\lambda}$
Dispersion	Numerical dispersion needed to compensate dispersion mismatch	Signal-to-noise ratio	$SNR_{ss}^{shot} = \frac{\eta P_{sample}\Delta t N}{E_\nu}$

Implementing a SS-OCT is a complex procedure determined by the combination of several such as performance of the swept source, imaging optics and sampling electronics. Optimization of these parameters will lead to develop a system with a high axial resolution, acceptable lateral resolution, imaging depth of 1-2 mm with a detection sensitivity that will allow to collect backscattered light from biological tissue. The following sections explain how to implement a real SS-OCT system.

3.2 Optical Coherence Tomography system design and implementation

The OCT system is composed of four main elements (Fig. 3.7): the Axsun swept source, an interferometer box, the signal acquistion electronics and the scanning mechanism. Each element was individually tested throughout the development of this thesis and then put together in order to obtain a synchronized system capable of acquiring B-scans. Each element is now explained.

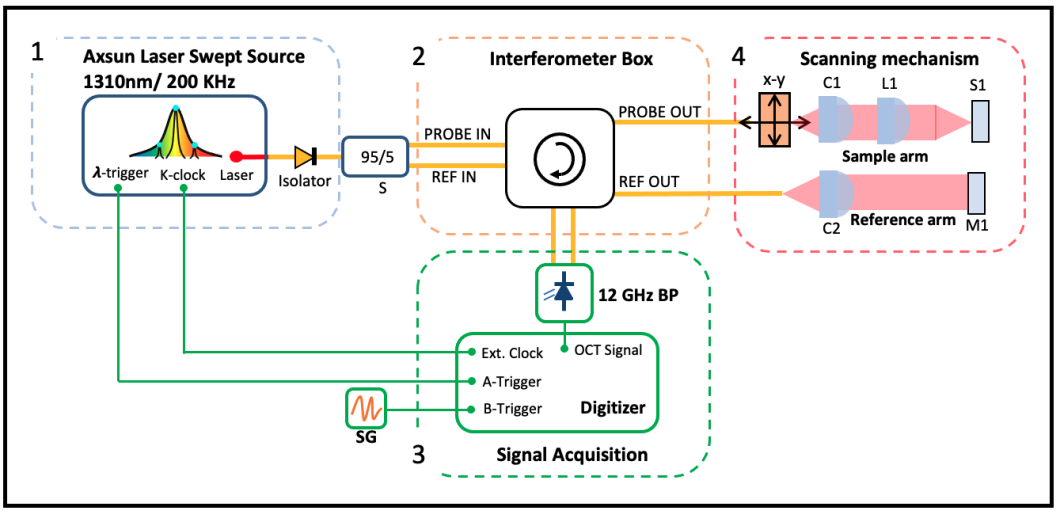

Figure 3.7: OCT setup composed of 1) Axsun Laser, 2) Interferometer Box, 3) Signal Acquisition 4) Scanning Mechanism. S: Splitter; C: Collimator; L: Lens; S: Sample; M: Mirror; SG: Signal Generator; BP: Balanced Photodetector.

3.2.1 Interferometer

The SS-OCT setup (Fig. 3.7) uses an all-integrated interferometer module (Castor Optics, QC, Canada) that is capable of multimodal imaging allowing simultaneous OCT @1300 nm and multi-photon tomography (MPT) @785 nm imaging modalities. This is accomplished by using a wavelength division multiplexer (WDM) to couple light coming from both the OCT and MPT laser sources into the same single-mode fibre. After that, a double-clad fibre optic coupler (DCFC) allows the coupling of both imaging modalities through the core of a double-clad fibre. Hence, the fluorescence signal for the MPT generated in the sample can be collected in the first cladding of the double-clad fibre and then reach the DCFC where the MPT and OCT signals are separated. The MPT signal is sent to a photomultiplier tube (PMT), while the OCT signal to a balanced photodetector. The internal components of the interferometer module are shown in Fig. 3.8.

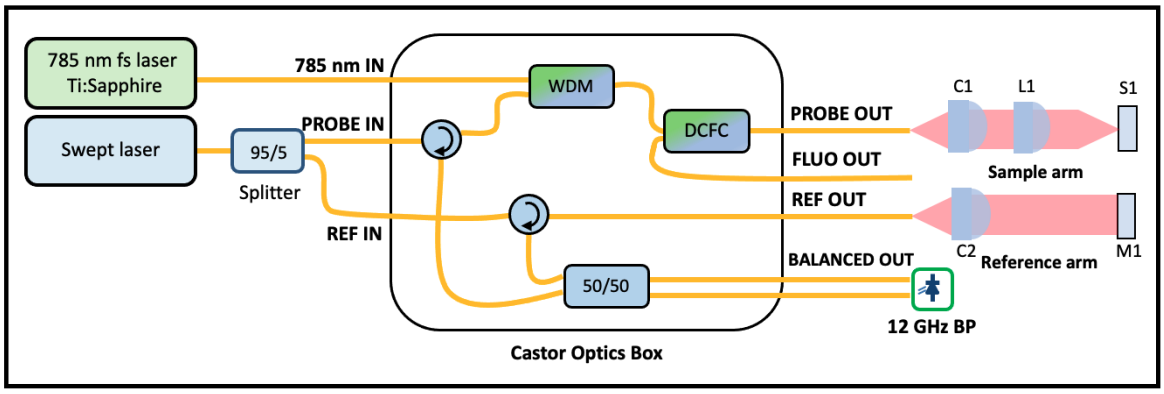

Figure 3.8: Interferometer box to allow simultaneous OCT and MPT imaging. WDM: Wavelength Division Multiplexer; DCFC: Double-Clad Fibre Optic Coupler; C: Collimator; L: Lens; M: Mirror; S: Sample; BP: Balanced Photodetector

For this thesis only the OCT modality is used, therefore, the swept source laser light is split by a 95/5 splitter whose outputs are connected to the inputs of the interferometer module, Probe-in and Ref-in (SMF-28/FC-APC connectors). This split ratio was selected since the sample arm has low collection from scattered light coming from the biological sample, hence, requiring more power. In contrast, the reference arm has a mirror with high reflectivity, therefore requiring less optical power due to lower losses. The optical signal at the Probe-Out can be connected through a FC-APC connector to a double clad fibre (DCF) in case of multi-photon fluorescence applications. However, since only OCT imaging is performed, a single-mode fibre (SMF/FC-APC) can also be connected.

An interference pattern was obtained by introducing a path difference of approx. 7 mm between the probe mirror and the reference mirror. In order to keep the fiber lengths balanced and close to the zero delay, two 1-meter single-mode fibers were connected to the *PROBE OUT* and *REF OUT*. In practice, a slight imbalance in path differences is desired between the focus of the sample spot and the reference mirror. Otherwise, if the lengths are exactly equal, the interference is at the DC level, which makes small positive and negative distances indistinguishable.

3.2.2 Signal Acquisition

Two main elements are necessary for signal acquisition, the balanced photodetector and the digitizer or acquisition card. The selected balanced photodetector is InGaAs based and has a bandwidth of 400 MHz and optimized for 1300 nm (PDB470C, Thorlabs, Germany). A commercial acquisition card (ADQ14OCT, Teledyne SP devices, Sweden) was used to perform signal sampling. The data acquisition is synchronized using external A-, B- triggers and k-clock analog inputs.

Four main connections between the acquisition card, the swept laser (Sect. 2.3.1), a signal generator and the OCT signal from the photodetector are made: the 200 kHz λ-trigger of the laser is connected to the A-trigger, an external 1.4 kHz signal generator is connected to the B-scan trigger, the k-clock of the laser to the ext. clock input of the acquisition card, and the OCT signal of the photodetector to the OCT data (Fig. 3.7). This configuration produces an interferogram signal every 5 μs which is sampled 1024 times at every up transition of the k-clock with a 14-bit resolution (Fig. 3.9a). This sampling generates an interferogram linearly spaced in k-space ($k = 2\pi/\lambda$) and is directly output at CH 1 of the card obtained through a PCI-e port connected to the computer (Fig. 3.9b). Numerical dispersion compensation was performed in a thick glass block using the methods described in section 3.1.6 and then applied to the acquired A-scans.

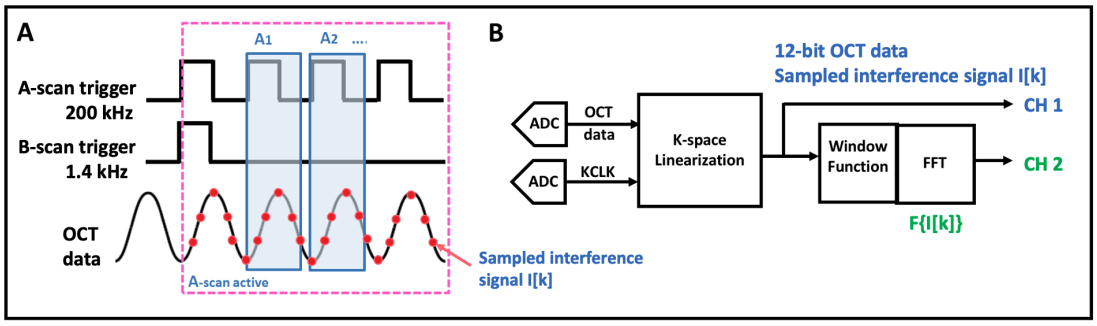

Figure 3.9: a) A and B-scan trigger inputs for synchronization. b) Internal architecture of the acquisition card. CH 1 outputs the sampled interference signal I[k]. CH 2 is the Fast Fourier Transform of I[k]

3.3 Scanning mechanisms

Two scanning mechanisms were developed for the OCT system, the first one with a translation stage and a microscope objective, and the second one using a Piezo-Tube (PZT) fibre-tip cantilever scanner and a GRIN lens. The purpose of the first scanning technique was to test the interferometer using single-mode fibres and to develop the necessary acquisition software while the endoscopic probe was being developed. Once the OCT setup was tested the second scanning method using the PZT and the GRIN lens was used as the main scanning system, this is termed the PICCOLO probe, as it was funded by EU H2020 project PICCOLO. Both scanning systems are shown in Fig.3.10.

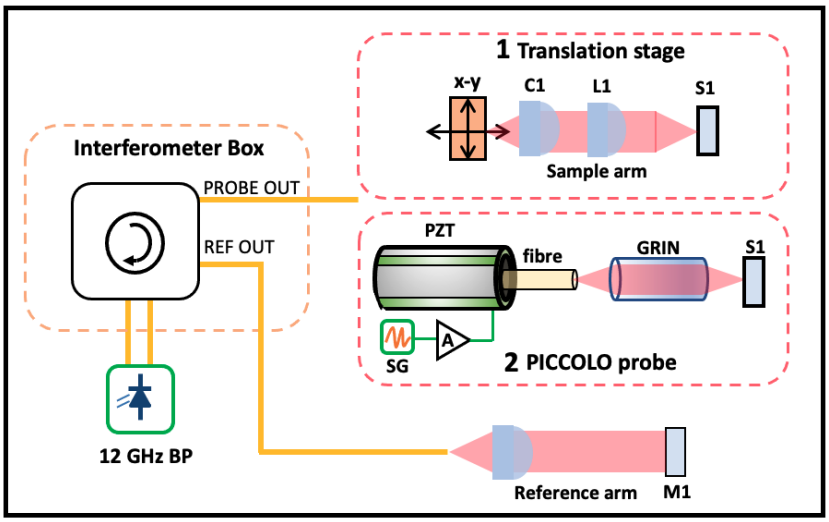

Figure 3.10: OCT setup showing the interferometer box and two scanning mechanisms. 1) Translation stage with a microscope objective x20, NA = 0.5. 2) PICCOLO probe using a PZT fibre-tip cantilever with GRIN lens

3.3.1 Translation stage

In order to identify possible limitations due to the scanning probe head and field-of-view that the PICCOLO probe will have, a stand-alone system was built that would use the

interferometer box, but changing the imaging optics and scanning method. To this end, a free-standing imaging head was developed using free space collimation and focusing optics, mounted on a computer-controlled XY stage. By using all the components except the probe head, any issues that may arise with the combining optics and fibres can be dealt with before attaching the PICCOLO probe. The setup is shown in Fig. 3.11

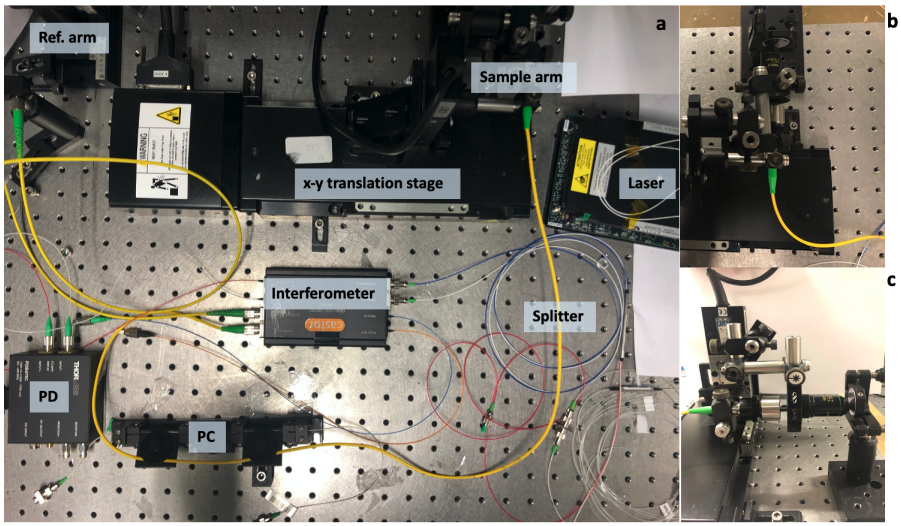

Figure 3.11: a) OCT setup b) Top-view of the scanning mechanism c) Lateral view of the fibre, collimator and lens arrangement

Motorised translation stages comprised of two Newport ESP compatible stages (M-ILS100CC and M-MFN25CC) with 0.5 μm step capability, controlled via computer through an ESP controller (ESP300). Stage travel are approximately 100 mm and 40 mm allowing ample field-of-view. A fibre collimator with 5 mm beam diameter and a x20 microscope objective (NA = 0.5) were chosen as the best options for collected signal and working distance. With this configuration the optical fibre, collimator and microscope objective are translated together, hence the optical beam always goes through the geometrical centre of the objective, avoiding aberrations caused by its edges. This provides a longer scanning range, however at slower scanning speed. Ex-vivo motionless samples can be imaged using this configuration.

A-scans and axial resolution

An interference pattern is obtained by moving the reference and sample mirrors in the axial direction, either closer or away from the optical fibres, until finding the zero-delay position of the interferometer. Three interferograms at the zero delay and $\pm$ 1.00 mm were obtained in air with the setup of Fig. 3.11 and are shown in Fig. 3.12. The interferograms were sampled using the acquisition card at 2 GSPS where each yellow block represents 1024 sampling points and 0.512 μs, and a 10 GSPS oscilloscope (50k total sampling points) where each green block is equivalent to 4096 sampling points and 0.4096 μs, both in a time window of $5\mu s$. The plot is divided in two main sections, before and after sweep trigger. As the interference gets closer to the zero delay the oscillation frequency reduces towards a DC value as observed in the blue signal. Conversely, as the optical delay increases towards $\pm$1 mm, the oscillation frequency increases.

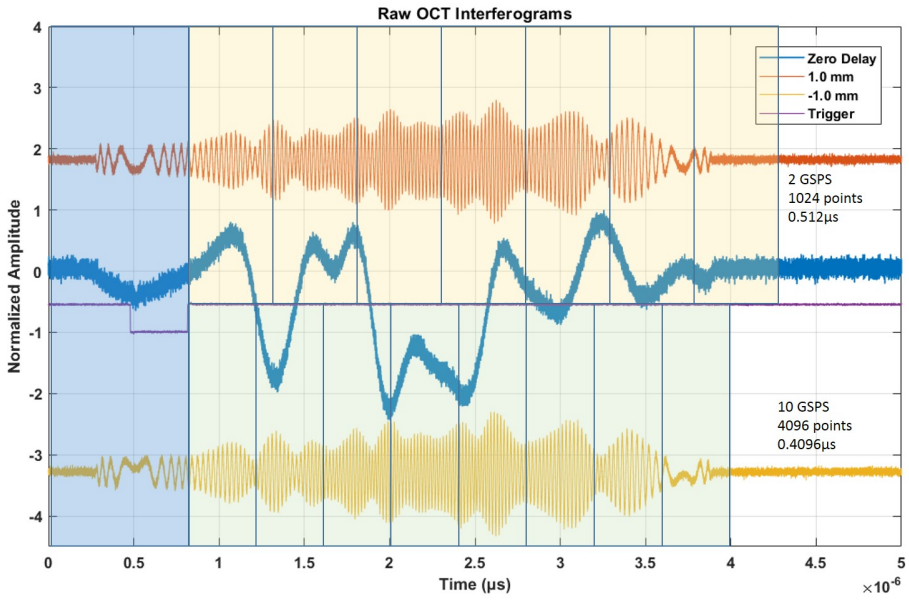

Figure 3.12: OCT interference signals close to the zero delay (blue) and at $\pm$ 1 mm (orange and yellow). The total time trace is 5 μs. The blue block of the trace is before the laser trigger. Each yellow blocks represents 1024 sampling points (0.512μs) sampled at 2 GSPS. Each green blocks represent 4096 points (0.4096 μs) sampled at 10 GSPS.

The dispersion effect is observed from the signal chirp. Just after the sweep trigger, the signal oscillates with a lower frequency compared to the central part of the signal and it then decreases again. This has a direct impact on the FFT by broadening the width of the FWHM as well as adding additional frequency peaks. After acquiring the raw interferogram the next step is k-resampling which can be done by interpolation or sampling the interferogram at every up-transition of the k-clock as done with the Teledyne card. The effect of k-resampling and dispersion compensation is shown in Fig. 3.13 for interferograms at a delay of ± 1 mm.

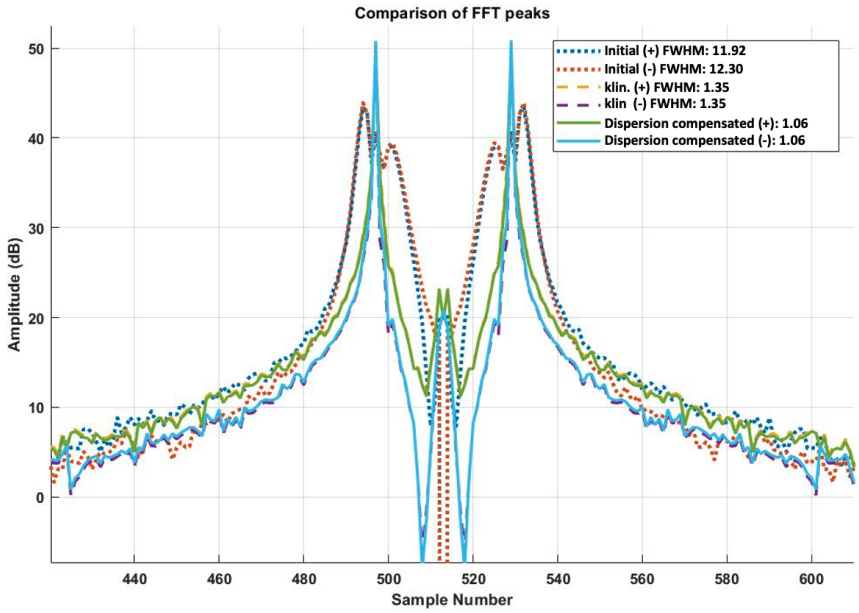

Figure 3.13: FFT peaks at depth of ± 1 mm. The blue and red dotted are the raw FFT which are broad and have multiple peaks. The dashed yellow and purple are the interferograms after k-resampling. Finally, the solid blue and green are the dispersion compensated peaks.

The raw FFT peaks (blue and red dotted) are broad and have multiple undesired peaks due to system dispersion. The effect of the k-resampling is to narrow the FWHM to a width of 1.35 points and eliminate the unwanted peaks (yellow and purple dashed), hence the importance of resampling the signal at linear k-space intervals so that the Fourier

transform is symmetric. The solid green and blue peaks are the dispersion compensated peaks, which are narrower than the k-resampled peaks with a width close to 1 pixel. This procedure shows the importance of k-resampling the interferogram and the applying the dispersion compensation in order to obtain a clean and sharp peak free from side-lobes and a with a high SNR to obtain sharp and noise-free images.

The **axial resolution of the OCT system in air is 10 μm** and was obtained by measuring the interference produced by two mirrors. The raw and dispersion compensated interferograms are shown in Fig. 3.14a, notice how the compensated interferogram (blue signal) does not have the frequency chirp anymore. The compensated FFT and bandpass filtered FFT peaks are shown in Fig. 3.14b. A-scans of a coverslip (glass index with n = 1.44) of approximately 160 μm in thickness were also obtained, two spaced sides could simultaneously be measured with high resolution. The peaks are 10 μm wide, which is the depth resolution limit of the system as expected from the laser source (Fig. 3.15).

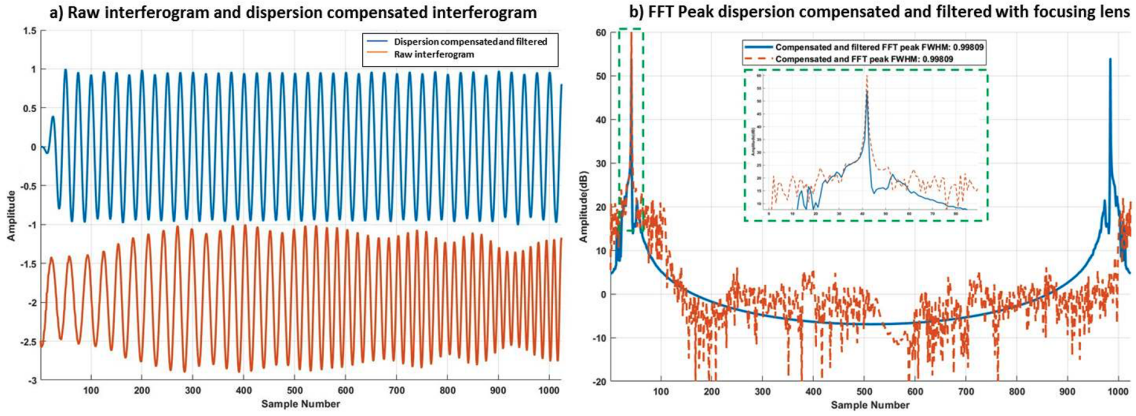

Figure 3.14: a) Raw interferograms produced by a mirror b) Dispersion compensated and filtered FFT peaks.

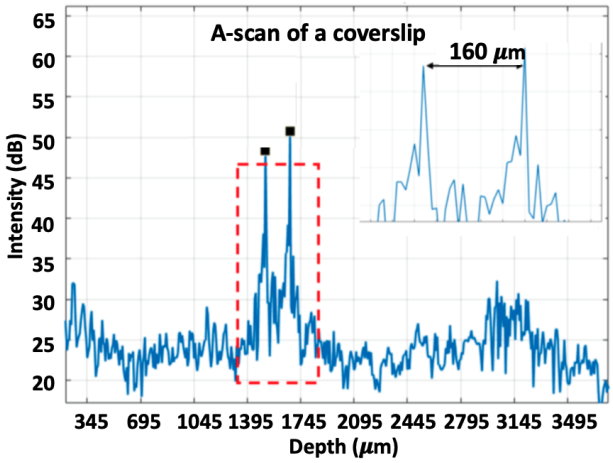

Figure 3.15: Axial resolution validation in a glass slide, correction factor is the refractive index of glass = 1.44

Lateral resolution and field-of-view

The lateral resolution was found to be 4 μm as measured from the 10% to 90% intensity transition on a semiconductor resolution target where the substrate had gold lines deposited each with a width of 200 μm as shown in Fig. 3.16.

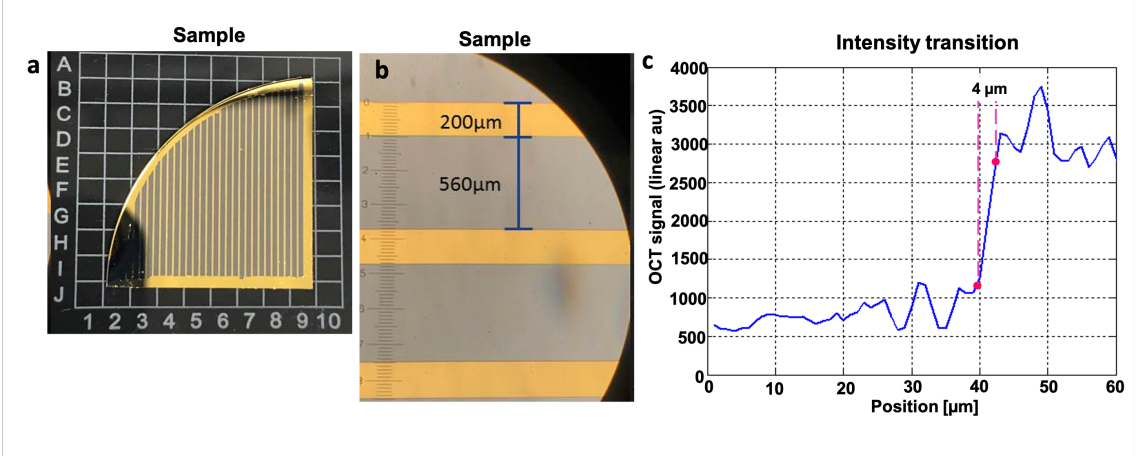

Figure 3.16: a) Semiconductor resolution target b) Gold lines on a substrate c) OCT signal across a metal edge to extract lateral resolution of 4 μm.

One advantage of using the translation stages is the ample field-of-view (FOV, 100 x 40

mm^2) for imaging of large sections of ex-vivo samples. In order to show this, a front-view OCT image of a pcb board with dimensions of 2x2 cm was imaged and shown in Fig. 3.17. Several features can be observed such as the wirebond of a semiconductor laser structure (20μm thickness), as well as reflective surfaces with features in the μm scale.

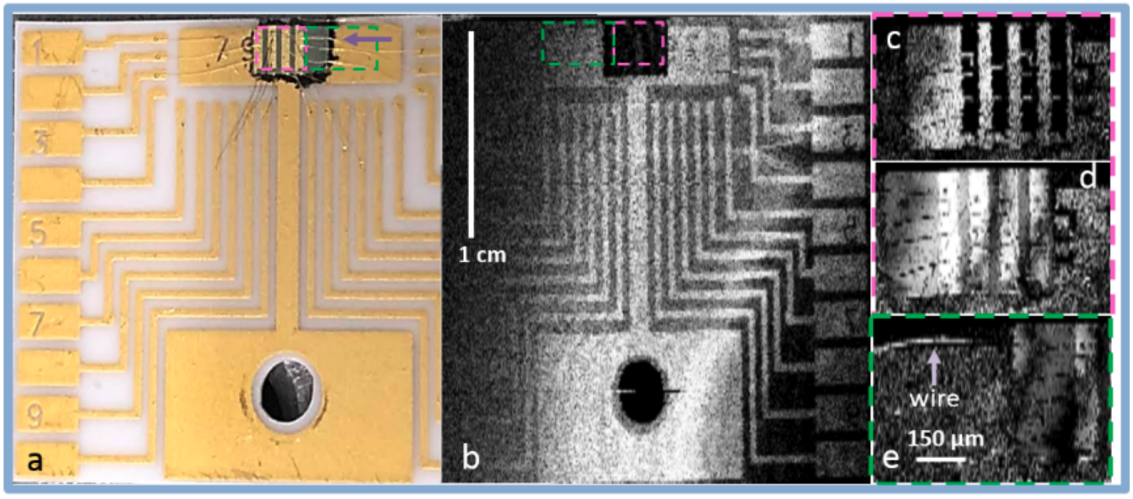

Figure 3.17: a) PCB board. The pink rectangle is the semiconductor laser structure. b)OCT image of the PCB and the laser structure. c) Laser structure acquired with a lateral step of $20\mu m$. d) Wires on top of the laser structure. e) Wire with a thickness of 20 μm.

3.3.2 PICCOLO probe

Endoscopic OCT requires in-vivo fast imaging capabilities in order to avoid image artifacts and present real-time cross-sectional images of the imaged organs. In this thesis an endoscopic OCT forward scanning imaging probe based on a fibre-cantilever piezotube (PZT) scanner resonating at 1.4 kHz and with a linear field-of-view (FOV) of 0.5 mm is presented. The trade-off between faster scanning speed and fewer A-scans per B-scan is compensated by an interleaving algorithm where consecutive B-scans are acquired and then interleaved, increasing the sampling density hence improving image quality. This process emulates a resonance frequency of 460 Hz without having to add extra-weight to

the fibre. The imaging probe can be integrated into the working channel of a commercial endoscope and has a diameter of ∅ = 2.5 mm, rigid length of 25 mm and a total length of 2.2 meter to allow mobility for in-vivo imaging. The following sections explain the mechanical and optical design of the imaging probe composed of the fibre-tip, a scanning system and focusing optics.

Scanning system - PZT

The forward-scanning probe was designed using a single tubular piezo actuator with the outer surface divided in four quadrants to form two pairs of electrodes. Such an actuator is referred as quartered-piezo tube (PZT). The optical fibre is placed inside the axis of the PZT. When sinusoidal waves of opposite polarities are applied to one electrode pair, the tube will bend transversely with respect to the two corresponding quadrants and the fibre free standing length will be displaced along the PZT. A schematic of the PZT with a fibre cantilever is shown in Fig.3.18. The deflection angle α together with the fibre free standing length l determine the linear scanning range l_{range} which for small angles is given by:

$$l_{range} \approx 2ltan\alpha \tag{3.3.1}$$

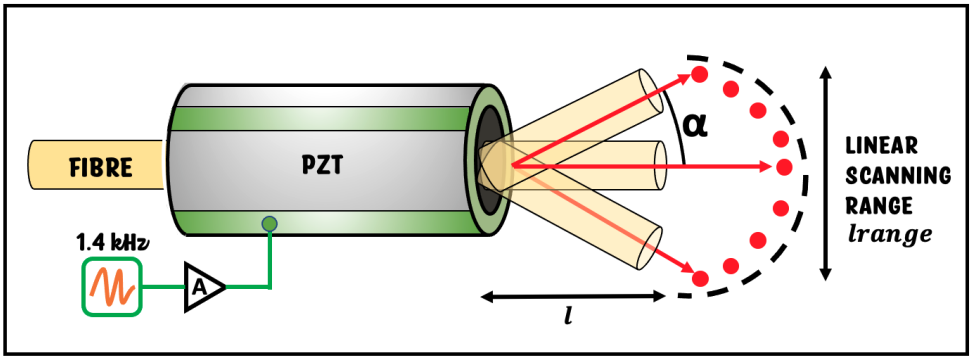

Figure 3.18: Fibre-cantilever piezotube (PZT) configuration. The deflection angle α and length l determine the linear scanning range l_{range}; PZT: piezo-tube; A: amplifier

The tube deflection angle α depends on the applied voltage (around $\pm$ 250 V) and on the tube length. Such deflections lead to scanning ranges on the order of few μmeters. This range can be increased by applying a sinusoidal voltage closer to the resonance frequency of the cantilever which depends on the free-standing length. In practice, this parameter is limited by the maximum rigid length for the fibre tip estimated to be $\approx$ 22.5 mm. Different scanning patterns can be achieved with the PZT by driving the quadrants with sinusoidal voltages. One such pattern is called "Lissajous pattern" which is obtained by applying on the PZT x and y axes two sinusoidal voltages with frequencies given by:

$$f_y = 2y_{rep}f/(x_{rep} + y_{rep}) \tag{3.3.2}$$

$$f_x = 2f - f_y \tag{3.3.3}$$

Where f is the resonance frequency and y_{rep}/x_{rep} the number of repetition cycles, creating a total repeat time t_{rep}:

$$t_{rep} = x_{rep}/f_x \tag{3.3.4}$$

The total number of points per sinusoidal signal is defined by the time axis length t_{length}:

$$t_{length} = ft_{rep}p_{fund} \tag{3.3.5}$$

Where p_{fund} is the number of points per fundamental creating a set of points x and y:

$$x = x_{amp}sin(2\pi f_x t_{rep}(1 : t_{length}/t_{length})) \tag{3.3.6}$$

$$y = y_{amp}sin(2\pi f_y t_{rep}(1 : t_{length}/t_{length})) \tag{3.3.7}$$

The parameters defined on Table 3.2 can generate a Lissajous pattern (Fig. 3.19 for a resonance frequency f = 1.4 kHz (0.7 ms/fibre oscillation) and 140 A-scans (points per fundamental, p_{fund}) at 200 kHz A-scan rate:

Table 3.2: Parameters to obtain a Lissajous pattern.

x_{rep}	10	y_{rep}	9
x_{amp}	1	y_{amp}	1
fx	1473 Hz	fy	1326 Hz
t_{rep}	6 ms	p_{fund}	140
t_{length}	1330		

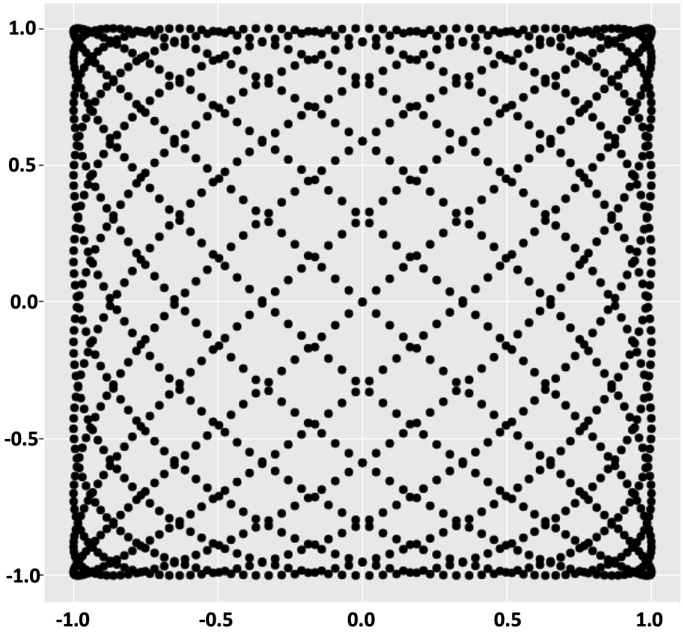

Figure 3.19: Simulated Lissajous pattern with perfect perpendicular axes.

With the previous parameters, the scanned area is approximately square and simulates the situation of two perfectly perpendicular scanning axes with the applied sinusoidal voltages and the same mechanical response. However, in the real case distortion in the fibre movement has to be considered, hence x_{rep}, y_{rep} cannot be chosen arbitrarily because fx, fy must be close to the fibre cantilever resonance range. The simulated Lissajous

pattern shows an approximate square area, however there are image distortions to be noticed. At the center, the separation between sampling points is longer as compared to the four corners where the distance is shorter making some points indistinguishable from each other. This is due to the nature of the fibre scanning, as the fibre approaches the corners it has to stop and bend back towards the center producing image artifacts. Additionally, at the current A-scan rate of 200 kHz only 140 A-scans can be acquired per fibre oscillation, hence to obtain an image with higher density of sampling points at least 10 repetition cycles (x_{rep}) must be acquired equivalent to a B-scan rate of $\approx$ 160 Hz (6 ms).

Focusing optics

For the imaging optic, a GRIN lens (GRIN2913, Thorlabs) with a diameter $\varnothing$ = 1.8 mm and 0.29 pitch was selected. The GRIN has a focal depth of 1.4 mm and is AR coated at 1300 nm, minimising back reflections. It is proposed to use this GRIN lens due to its small dimensions and ease of integration. This lens focuses the divergent light from the fibre core down to the tissue. The magnification M determines the FOV according to:

$$FOV_{max} = M * l_{range} \tag{3.3.8}$$

The lens is designed to have a 1:1 magnification with an object and working distance $z1$, $z2$ of 1.48 mm. However, a design requirement is to increase the FOV as much as possible. For this reason, the object distance to the 1^{st} surface of the GRIN was decreased to 0.5 mm (z1), which pushes the focal length back to a distance of 3.4 mm (z2) as shown in Fig. 3.20. With this modification, a magnification of x2 and spot size of 22 μm is estimated:

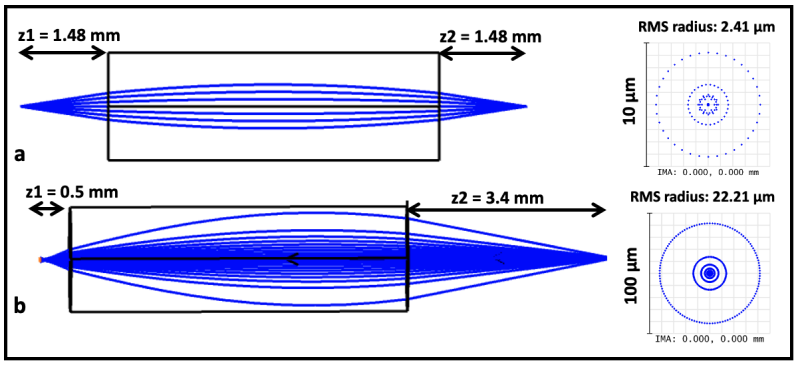

Figure 3.20: Zemax simulation of GRIN2913. a) Configuration to obtain a 1:1 magnification b) Configuration to increase the magnification; z1 = 0.5 mm, z2 = 3.4 mm

In order to estimate the FOV of the GRIN, light was focused onto an infra-red camera to image its spot shape while displacing the fibre laterally using a translation stage with the setup shown in Fig. 3.21a. It was observed that for a fibre lateral displacement of 500 μm from centre, the image spot is not too distorted (Fig. 3.21b), hence with the obtained magnification a FOV of 1 mm can be achieved. The shorter the distance z1, the greater magnification will be obtained as shown in Fig. 3.21c. A 2^{nd} example of the FOV was obtained by imaging the front-view of a PCB achieving a FOV of $\approx$ 3.2 x 2.8 mm^2 (Fig. 3.22). The PCB was imaged by displacing the fibre with the translation stage while having the GRIN lens fixed. In practice the FOV will be smaller. As the fibre sweeps, the signal is strongest in the centre and slightly less at the edges. This is due to the change in angle of the probe spot in relation to the sample, and the change in angle of the fibre with respect to the lens.

Device tip

In practice, the scanning system, focusing optics and external protective housing constitute the device tip. Two main parameters are required in order to integrate the imaging probe into the working channel of a commercial endoscope, the overall maximum outer diameter $\varnothing_{max}$ of 3.5 mm and the maximum rigid length of 22.5 mm, hence limiting the dimensions of the imaging optics. With this in mind, a forward-scanning optical probe

has been designed and assembled. The mechanical design of the scanning probe is composed by several elements including a plastic ring (1), housing (2), piezo-quartered tube (3), double-clad fibre (4) housing (5), lens housing (6), GRIN lens (NA = 0.46, pitch = 0.29, GRIN2913, Thorlabs) (7) as shown in Fig. 3.23.

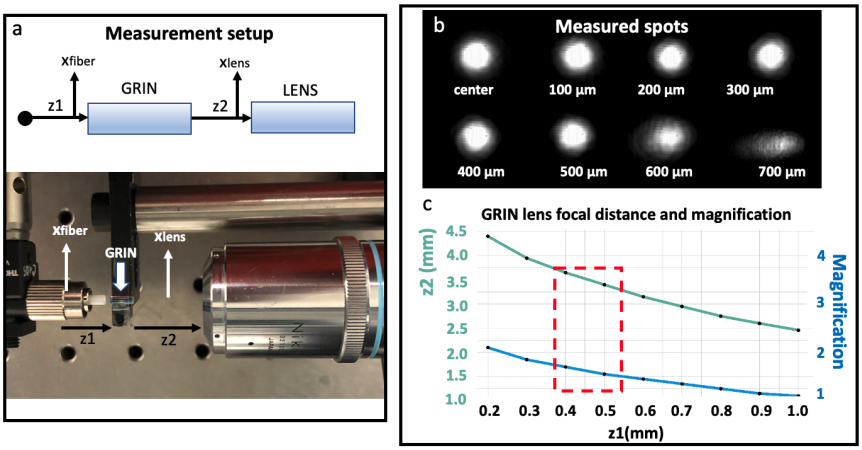

Figure 3.21: GRIN lens magnification a) Measurement setup showing the fibre, the GRIN and a microscope objective. Distance xfibre is displaced to measured the spot quality b) Measured image spots for lateral fibre-GRIN displacements 0 to 700 μm from centre c) Focus distance z2 and magnification as function of distance z1.

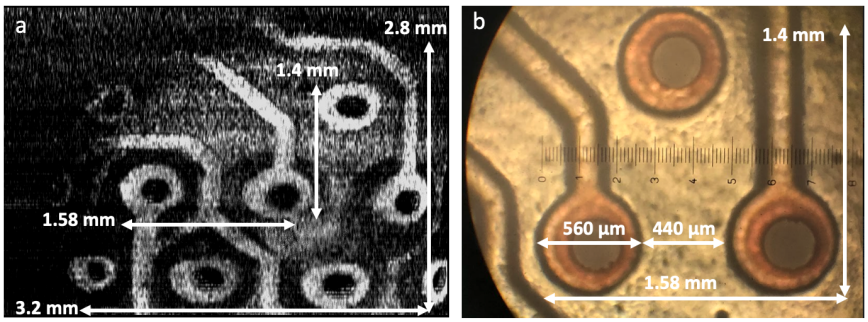

Figure 3.22: a) PCB front-view OCT image showing a field-of-view of ≈3.2 x 2.8 mm^2 that can be obtained with the GRIN2913 b) PCB under microscope to correlate the dimensions.

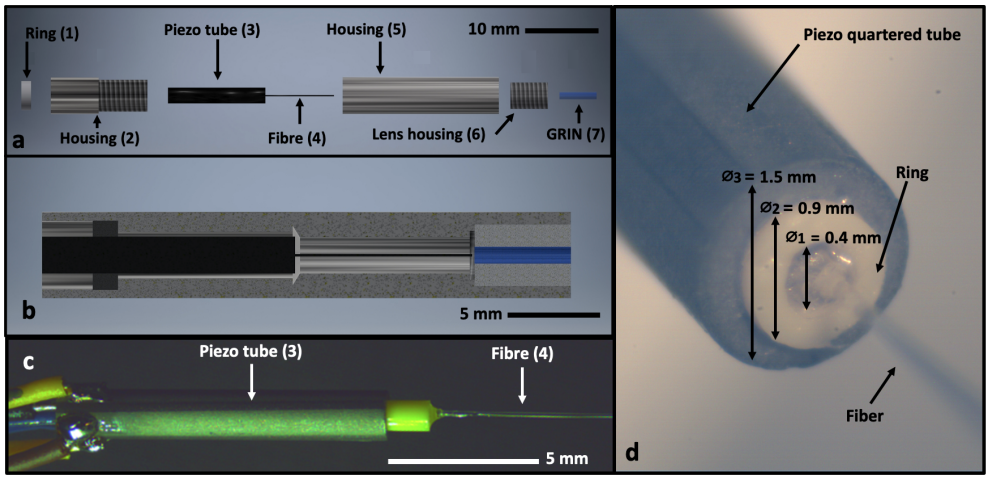

Figure 3.23: a) Optomechanical elements b) Mechanical assembly of the elements of the imaging probe c) PZT connections d) Front-view of the imaging probe. The probe was assembled by the project partner L4T-Light4tech.

The elements were assembled by cleaving the fibre (4), gluing it to the PZT (3) and finally inserting them into the 1st mechanical housing (2) using the plastic ring (1). The GRIN lens (7) was glued to a cylindrical lens housing (6). Finally, both housings (2, 5) are screwed together allowing distance adjustment between the tip of the fibre and the GRIN lens. The external housing pieces are made of biocompatible aluminium and polyoxymethylene. The wired PZT is shown in Fig. 3.23c. The imaging probe is referred to as the PICCOLO probe and is shown in Fig. 3.24.

Interleaving

During fibre oscillation, it is important to consider that there is a non-uniform velocity of the fibre, creating a spatial separation between B-scan points as the fiber is moving while acquiring an A-scan. In practical terms the problem of the fibre movement during an A-scan is made worse for larger physical sweep range. For the selected swept source with an A-scan rate of 200 kHz, the scan position will move by 4 μm during an A-scan which is at the limit of the acceptability because it is comparable with the expected spatial resolution for the OCT system, hence slight blurring of the image will occur.

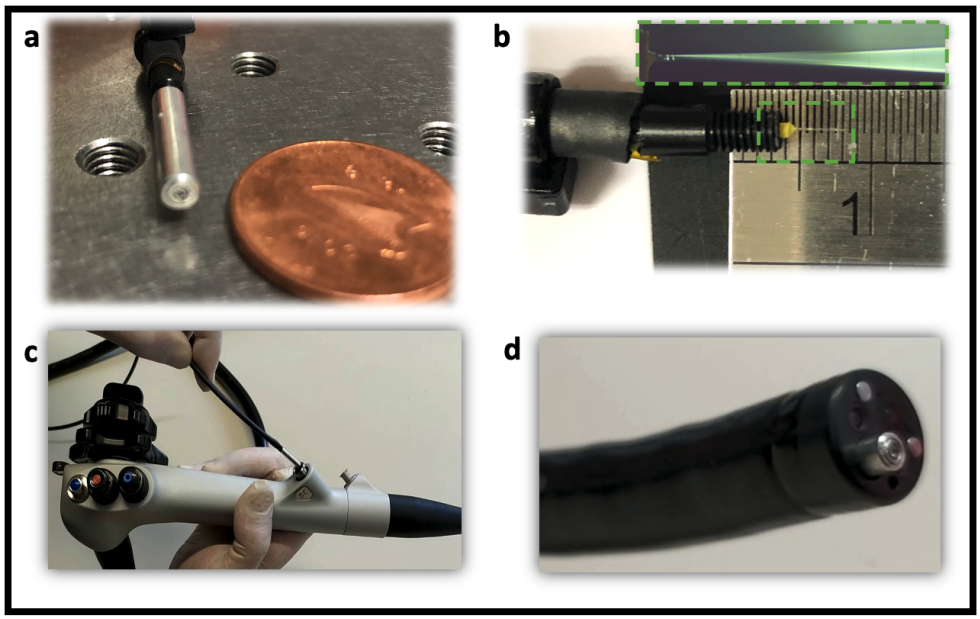

Figure 3.24: a) Assembled PICCOLO OCT-imaging probe b) Fibre-tip cantilever c) PICCOLO probe inserted into the working channel of a commercial endoscope d) Front-view of the endoscope showing the outer surface of the GRIN lens

Fibre scanning was performed by applying a sinusoidal signal at the resonance frequency of 1.4 kHz (700 μs) to only one pair of electrodes of the PZT. The PZT bends transversely and the fibre free standing length is displaced along the PZT tube. A full fibre oscillation requires 0.7 ms. In this time window it is possible to acquire 140 A-scans (5 μs per A-scan). Since the fibre oscillates with a sinusoidal pattern along only one axis, a mirrored image will be obtained, hence only the data of half cycle is needed. This is equivalent to only 70 A-scans per B-scan image as illustrated in Fig. 3.25a, which is an important trade-off to consider, the faster the fibre scanning frequency the less sampling points in the image. This means the density of A-scans per B-scan image will be lower, hence obtaining an image with a lower lateral resolution.

This trade-off is compensated by interleaving consecutive B-scans to increase the sampling density (Fig. 3.25b). This is possible since consecutive B-scans are not the identical as the A-scan/B-scan rate are asynchronous. Each B-scan is at a different position with

new sampling points contributing to more image data, hence increasing the image quality. The procedure to interleave consecutive B-scans is shown in Fig. 3.25b; three consecutive B-scans are acquired to form a new image with a size 210 A-scans per B-scan. The individual data of this image is filled with the obtained individual A-scans in order to increase the sampling density, which takes 2.1 ms to be acquired as shown in Fig.3.25c. This procedure is equivalent to emulating a resonance frequency of 460 Hz without adding extra-weight to the fibre and hence providing more lateral information and increasing image quality.

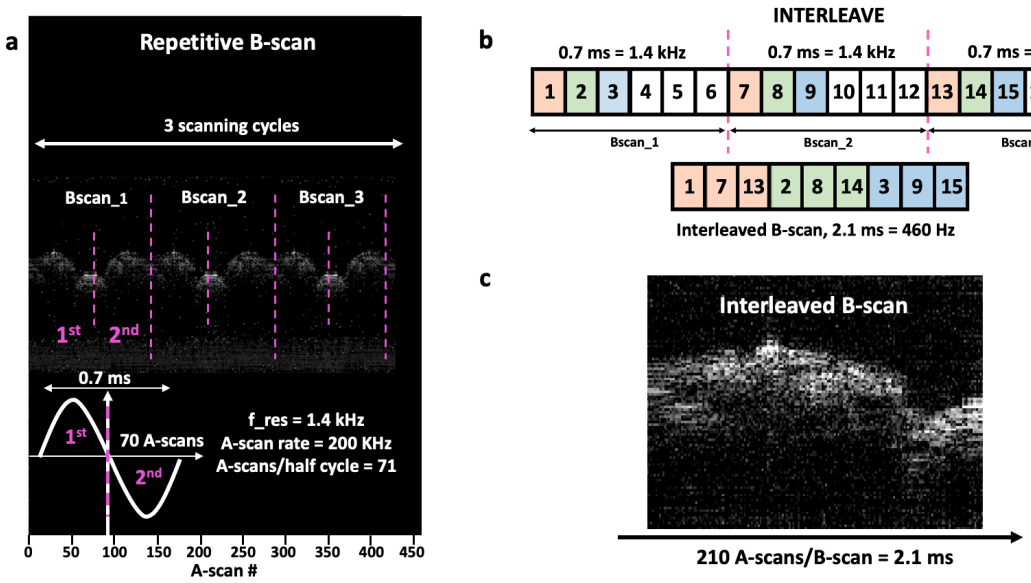

Figure 3.25: B-scan interleaving. (A) Three consecutive B-scans with 140 A-scans each are acquired in 0.7 ms. (B) Interleave algorithm to increase the sampling density per B-scan taking a total time of 2.1 ms. c) Final interleaved image composed of 210 A-scans per B-scan.

B-scans

B-scans obtained on a reference cover slip and microscope slide are shown in Fig.3.26. Both samples show an axial resolution of 10 μm in air, which is the resolution limit due to the swept source laser. Focusing on the glass surface gives approximately 40 dB SNR, while visualising both upper and lower surfaces gives about 25-30 dB. Interfaces can be measured to 5 mm in depth. Using a mirror as a reference object saturates the detection

electronics, showing good optical coupling.

Notice that the backscattered light intensity at the center of the image is brighter as compared to the sides. This is due to the nature of the fibre scanning that bends towards the edges, therefore the object is no longer at the exact focus of the GRIN lens. Also, this is equivalent to an object that is 'deeper' in axial position with a reduced sensitivity. In order to place the B-scan at the center position, a phase delay is introduced to the sinusoidal signal that compensates for out of phase scanning.

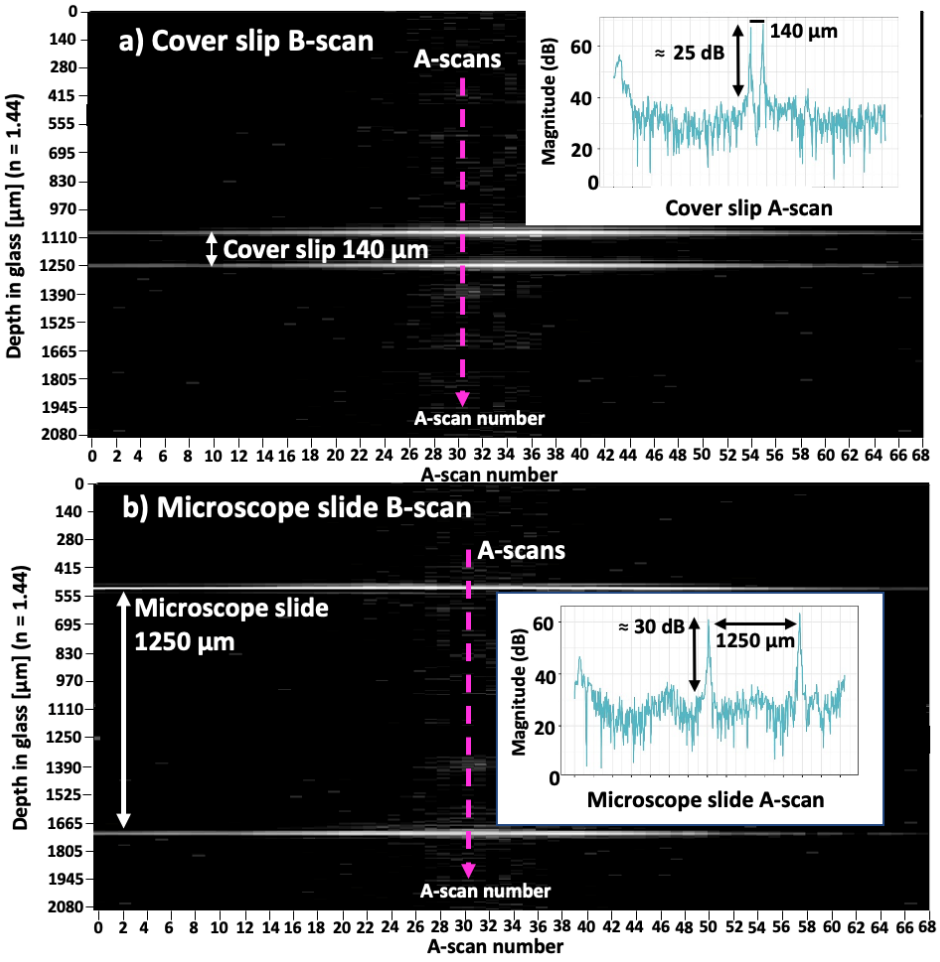

Figure 3.26: a) Coverslip B-scan with 69 A-scans. Coverslip A-scan showing a peak separation of 140 μm and SNR $\approx$ 25 dB. b) Microscope slide B-scan with 69 A-scans. Microscope slide A-scan showing a peak separation of 1250 μm and SNR $\approx$ 30 dB.

3.4 Conclusion

The first half of this chapter has discussed the mathematical and physical definitions of an OCT system in terms of an interference signal in k-space, that is further Fourier transformed to obtain reflectivity profiles in z-space (A-scans). Obtaining and optimizing an A-scan is the first step to develop the OCT system. The second half of the chapter part has presented the system design and implementation of a SS-OCT. Conclusions for A-scan optimization, OCT system performance and scanning mechanisms are further discussed. The achievement of this chapter is the fully assembled endoscopic OCT system with the PZT fibre scanning probe shown in Fig. 3.27.

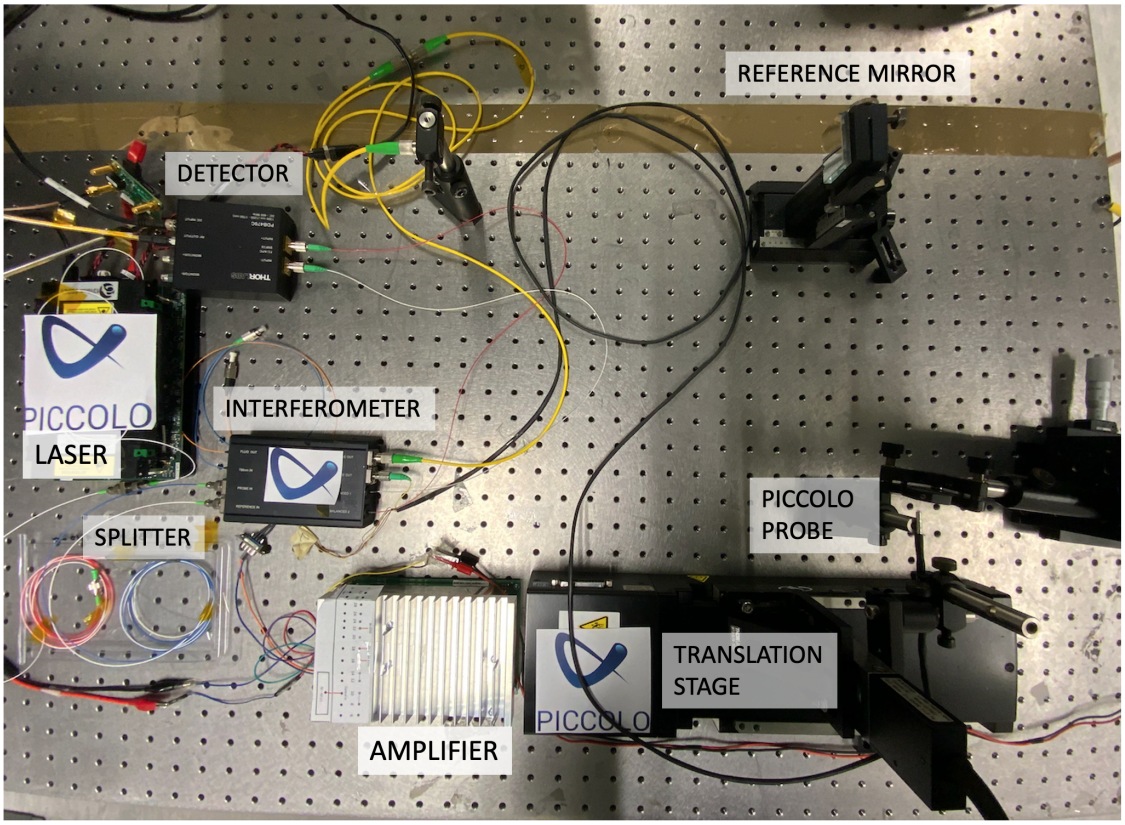

Figure 3.27: Fully assembled endoscopic OCT system.

3.4.1 A-scan optimization

An A-scan is the basic building block of any OCT system. Its quality and optimization is determined by the combination of several parameters such as axial resolution, signal sampling in k-space, dispersion compensation, Fourier transformation from k- to z-space, SNR and imaging depth. An axial resolution of 10 μm in air with a 40 dB SNR focusing on a glass surface within a 5 mm imaging window was obtained with the endoscopic imaging probe. The axial resolution is as narrow as it can be based on the parameters of the swept source, k-resampling and by accurate numerical dispersion compensation using the proposed algorithm (Sect. 3.1.6). k-resampling using the acquisition card was sufficient and no further k-remapping was necessary. Additionally, the dispersion compensation algorithm matched the dispersion of both arms of the interferometer without requiring additional physical elements for both single mode and double clad fibres. In practice, however, the final user, such as a clinician, might face certain challenges when imaging a tissue if the quality of the A-scan is affected. This has to be considered as the user has no experience optimizing the OCT system. To avoid this, the following factors have to be considered:

- Calculate the dispersion correction factor. This is done using either a thick glass block or a mirror. This, however, can be a drawback for the final users who lack this expertise. A solution is to calculate the dispersion correction factors in advance by either using phantoms that resemble the optical properties of tissue or imaging real tissue for further adjustment of the A-scan within the imaging window of 5 mm.

- Correct positioning of the A-scan to avoid mirrored images. One of the drawbacks of Fourier domain are the mirrored image artifacts (Fig. 3.4), which are compensated by the positioning of the reference mirror. Practically, this can be automated using either a variable optical delay line, or motorized stage to auto-align and center the A-scan to avoid image artifacts.

- Polarization state alignment. One of the drawbacks of using optical fibres is that the quality of the interference pattern depends on the polarization state, which in practice can be easily distorted by bents, mechanical movements or vibrations on the fibre. This can be solved by using either manual polarization controllers to fix the position of the fibres or by motorized fibre polarization controllers that optimise the polarization state for every measurement session to obtain consistent sensitivity.

3.4.2 OCT system improvement

A fully functional endoscopic SS-OCT has been developed. This was accomplished by the use of a swept source, interferometer, signal sampling and scanning mechanism. The all-integrated interferometer module simplified the integration of the optical elements such as the swept source, splitters, optical fibres, sample and reference arms, and connecting the interference signal to the balanced photodetector. This provides flexibility for system integration as well as reducing the size of the overall system. However, there were some drawbacks. The interferometer box is designed to combine two imaging modalities including OCT and MPT, which requires a 785 nm Ti:Sa fs laser and a photomultiplier tube (PMT) as a detector, by using wavelength division multiplexers (WDM) and double-clad fibre optic couplers (DCFC). Nonetheless, for this thesis, only the OCT imaging part was used. High levels of noise were detected when using the double-clad fibre as compared to a single mode-fibre. This were due to internal reflections on the connectors and that were translated to constant reflectivity peaks in the A-scan. These peaks were avoided by compensating the reference arm distance so that the peaks were outside an imaging window of 1 mm. Therefore, the double clad fibre can be replaced by a polarization maintaining single-mode fibre to avoid the noise levels as well as using dedicated fibre splitters for OCT without the need of the second imaging modality.

The use of the double-clad fibre is justified since the ultimate goal of the project, which is out of the scope of this thesis, is to combine both OCT and MPT imaging to provide structural and functional image data. This system improvement requires the GRIN lens to be adapted to a broad wavelength spectrum going from 500 nm of the fluorescence signal to over 1300 nm of the OCT source. There will be a trade-off to consider in selecting the numerical aperture of the imaging lens since MPT requires a tight focus, which will reduce the imaging depth of OCT.

Signal sampling was accomplished by the combination of the balanced photodetector and the commercial acquisition card. In practice, the detector did not provide perfectly balanced signal since one of the arms had more optical power. This was compensated simply by intentional misalignment of the optical fibre as it was observed that balanced detection significantly reduces the DC and autocorrelation noise. The acquisition card was fast enough to sample the interferogram using the external k-clock functionality. However, the card was limited to acquiring only a maximum of 1300 A-scans per B-scan. Possible reasons for this was buffer saturation or lack of software compatibility. Also, direct transfer between the card and the dedicated LabView software was not accomplished affecting the real-time display of the B-scan. These issues can be solved by writing dedicated software using C-language which is the native programming language of the acquisition card.

3.4.3 Scanning mechanisms

Two scanning mechanisms were presented, the first one using a translation stage and the second one using the PZT fibre scanner. The translation stage provided an ample field-of-view of 100 x 40 mm^2, which facilitates sample placing. A drawback is the scanning speed as it is slow compared to conventional galvanometric scanning systems. However, translation stages are useful to scan long sections of ex-vivo motionless samples. This

scanning mechanism was mainly used to optimize the performance of the OCT system.

Assembly of the PZT fibre scanner required precise μm alignment for the integration of the optical elements. A probe that is mechanically stable was hard to accomplish due to the size of the components, this was done by gluing the fibre to the PZT and placing the GRIN lens in a cylindrical lens housing that allowed distance adjustment. One drawback, however is the difficulty of placing the fibre and lens at the desired working distance. This was observed in practice as the lens was misaligned and had to be placed manually without a clear reference of the alignment distances. A design solution for this is to use 3D printing in order to accomplish more precise alignment by having guides to where to place the elements. This also provides a more solid construction being less prone to mechanical vibrations.

The imaging probe fits into the working channel of a conventional endoscope due to its length of 2.2 meters. The obtained FOV was limited to approx. 0.5 mm, since the amplified sinusoidal voltage was limited to avoid breaking the fibre. A Lissajous pattern was not proven since only one voltage amplifier was available when scanning the fibre. The size of the probe can still be slightly reduced as the overall dimensions are close to the maximum allowable outer diameter and rigid length. Trade-offs have to be considered to accomplish size reduction such as shorter FOV using a smaller imaging GRIN lens and placing the fibre closer the to the inner surface of the lens reducing image magnification.

Chapter 4

Biological imaging

The assembly of the OCT endoscopy system has been accomplished so far by investigation of swept sources, OCT system design, fibre scanner optomechanical design and imaging probe assembly. The last step is to perform OCT imaging in biological tissue as presented in this chapter. The chapter starts by presenting colonic polyps as the biological tissue to be imaged in Sect. 4.1, to further introduce rat models of colonic tissue with healthy and developed polyps in Sect. 4.2. Original contributions in this chapter include OCT images acquired using both the translation stage and the PICCOLO endoscopic imaging head. The imaging procedure and polyp images for the translation stage are shown in Sect. 4.3 and Sect. 4.4 respectively. Finally, OCT imaging using the endoscopic PICCOLO probe is discussed in Sect. 4.5 showing biological imaging of colonic rat tissue and human tissue in Sect. 4.5.1 and Sect. 4.5.2 respectively.

4.1 Colonic polyps

Colonoscopy is the gold standard for identification of polyps. This is an endoscopic examination with direct visualization of the colonic mucosal surface. Conventional white-light endoscopy images of different types of colon tissue including healthy, apparently healthy, benign hyperplasia and neoplasia are shown in Fig. 4.1. These kind of images provide

an overview of the colon walls and general anatomical landmarks. One of the main limitations of conventional white-light endoscopy is differentiating between healthy and apparently healthy tissue. For such reason OCT is combined through an imaging probe in order to visualize sub-surface structure that will provide accurate structural information.

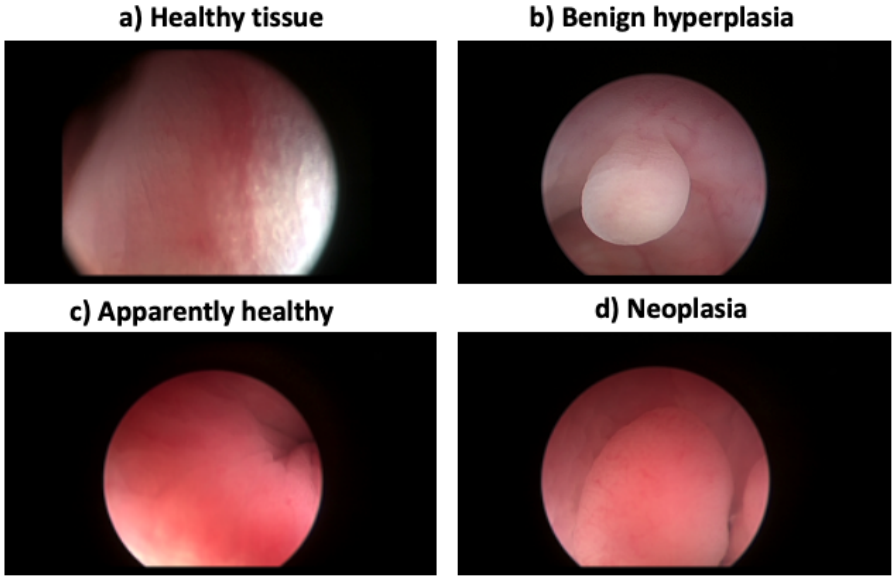

Figure 4.1: Different types of colon tissue in humans. a) Healthy tissue. b) Benign hyperplasia. c) Apparently healthy. d) Neoplasia. Images obtained by the consortium of the PICCOLO project.

Hyperplasia is histologically a gross thickening of the mucosa, where some growth may be pedunculated and herniation of epithelium through muscularis may occur. Hyperplastic polyps are defined as small sessile lesions characterized histologically by an expansion of the crypt replicative zone and a maturation of epithelial cells in the upper portion of the crypt. Finally, gastrointestinal intraepithelial neoplasia (GIN) is defined as histologically apparent areas of dysplasia that are not visible grossly ($< 0.5 - 1.0mm$). These lesions may be referred to as microadenoma, microcarcinoma [131].

4.2 Rat models

The large intestine of a rat model is used to simulate diseases since it is similar in mural structure as that of humans, consisting of mucosa, submucosa, inner circular and outer longitudinal tunica muscularis, and finally serosa[132]. For this thesis, colonic samples have been extracted from different groups of rat models. These consisted of genetically modified rats with neoplastic polyps and rats with hyperplastic polyps surgically created in the descending colon. In the ascending and transverse colon no polyps were induced, in order to have comparative healthy mucosa for comparison.

For this thesis, ex-vivo samples have been extracted from the colon of Polyposis in Rat Colon (PIRC - F344/NTac-Apcam[133, 134]). These were provided by the Rat Resource and Research Centre (University of Missouri). After an exploratory colonoscopy procedure under the correct anesthesia, the colonoscopy was performed with the objective of locating all these lesions using white light rigid cystourethroscope of 2.9 mm in diameter. For the ex-vivo sample preparation, the rat colon was excised and a protocal for sample preservation in refrigeration, for subsequent measurement, was applied (Fig. 4.2):

1. Extract the rat colon and divide it in three regions following the ascending, transverse and descending colon.

2. Immerse all regions in 4% formaldehyde overnight at a temperature of 4° for at least 14 hours.

3. Submerge the samples in phosphate buffered saline (PBS) and 0.1% of sodium azide and keep in refrigeration at 4°.

Ethical approval for the samples was provided by the CCMIJU Animal Welfare Committee and by the Regional Government of Extremadura, Spain. The presented OCT system was used to obtain cross-sectional images of these samples. The purpose was to acquire sub-surface image data and to identify structural μm patterns to distinguish between healthy tissue and neoplastic polyps with an abnormal growth. OCT is used to obtain images of gastrointestinal epithelium, including small lesions of a few mm which represent early colorectal adenomas. With the cross-sectional images it is possible to measure mucosal thickening at the site of adenoma (2x normal mucosal thickness) and a mild protrusion above the basal mucosal height ($<50\%$ total thickness).

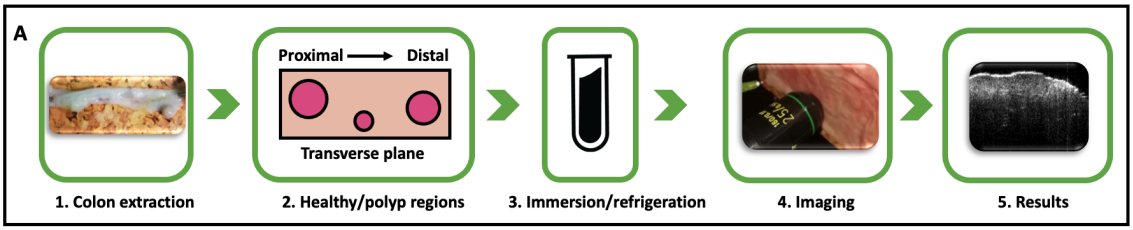

Figure 4.2: Sample preparation. 1) Colon is extracted. 2) Colon is divided in three regions including healthy and polyp regions. 3) Sample is immersed in PBS to be preserved. 4) Imaging is performed 5) OCT images are acquired.

4.3 Imaging procedure using the translation stage

For acquiring a B-scan, an ex-vivo sample is placed at the focus of the microscope objective and then the motorised translation stage is moved horizontally along with the imaging optics. The number of A-scans/B-scan is defined by the specified translation distance and the step resolution. E.g., 2000 A-scans are be acquired for a distance of 5 mm and a resolution of 2.5 μm. The total number of B-scans is calculated in the same way. A horizontal B-scan is acquired by translating the stage, returning it to the zero position and then moving it to the next vertical position, generating a C-scan with 3D image data.

The interferograms are compensated while the stage is moving. The option of selecting the scanning step gives the flexibility to the user to either increase or decrease the image resolution, e.g., to obtain a higher resolution image in a shorter scanning range, or a lower resolution image for a longer scanning range. This process is shown in Fig. 4.3 and is repeated until all B-scans are acquired. This data acquisition procedure is used for sample imaging. The tissue is divided into grossly healthy to create control regions and polyp-containing regions across a transversal plane from proximal to distal directions. During an imaging session a sample is taken out of refrigeration and imaged in sessions no longer than 20 minutes.

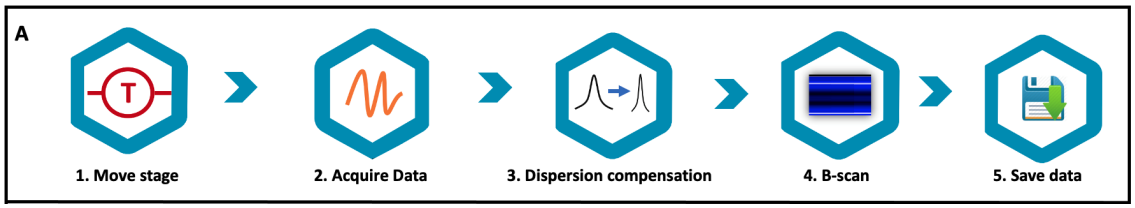

Figure 4.3: Sample scanning procedure using the translation stage. 1) Move the stage with the imaging optics. 2) Acquire data. 3) Apply dispersion compensation algorithm. 4) Form B-scan. 5) Save data.

4.4 Polyp imaging using the translation stage

OCT ex-vivo imaging was performed with the purpose of studying the sub-surface polyp structure and the surrounding healthy regions. One such a sample with a neoplastic polyp is shown in Fig. 4.4a. The sample was scanned in an area of 1 x 2 mm^2 with a step size of 1 x 20 μm^2 with a depth of 900 μm. The total number of B-scans was 100, each with 1000 A-scans. An en-face image of the polyp is shown in Fig. 4.4b. It is possible to observe the abnormal growth in the periphery of the polyp, e.g., in (1) the indicated region is thicker compared to the thickness of (3). Region (2) presents a dent and inhomogeneous shape as the polyp had an abnormal growth. 3D OCT data allows the reconstruction of en-face

images at different depths compared to the standard front view of colonoscopy.

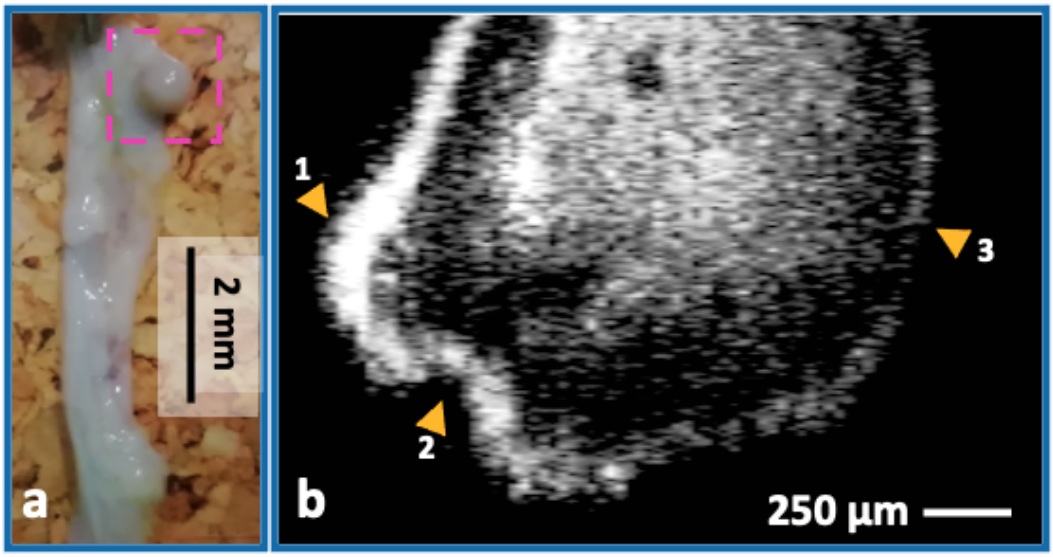

Figure 4.4: a) Colon sample with one polyp. b) Plane frontal slice. (1) Thicker region/growth in the polyp periphery; (2) Dent and inhomogeneous shape in the polyp; (3) Thinner region of the polyp periphery.

A second colon sample with two neoplastic polyps is shown in Fig. 4.5a. The sample shows the proposed method of extracting the rat colon and then dividing it in healthy and polyp regions across the transversal plane in order to provide clear imaging regions to differentiate the sub-surface morphology and observe how a developed polyp affects normal tissue. Two neoplastic polyps and one healthy region were imaged. For all images, the mucosa appears as a more highly scattering band, compared to the submucosa which was a less scattering layer. For polyp one (Fig. 4.5b), the highest scattering layer is the epithelium, so its thickness and shape can be clearly observed, and although the curvature is not fully round no major deformations are present (1). However, there is a region (2) of approximately 250x100 μm^2 that has high backscattered intensity underneath the epithelium, although homogeneity is still observed. An A-scan across the dashed yellow line is shown in Fig. 4.5c. Peak a is the epithelium while peak b represents other μm features that are comparable in thickness and intensity as the epithelium. In between the two

peaks there are other internal peaks presenting an inhomogeneous structure as compared to other areas of the polyp.

For the second polyp (Fig. 4.5d), the epithelium is observed as well, however its curvature is less symmetrical presenting a gap (3) affecting its overall shape. Despite this, the sub-surface layers do not present inhomogeneities. There is a region (4) that presents high backscattered intensity similar as in the first polyp. Polyp 2 presents internal μm features that can be observed across an A-scan (Fig.4.5e). The epithelium is measured as a single peak (c) with high back-scattered intensity, internal μm features (d) with similar thicknesses and intensity as in the epithelium are also observed.

Healthy tissue (Fig. 4.6b) presents a different substructure information. The epithelium presents small 'bumps' as expected from its layered structure (5), yet its thickness can be clearly observed. One major difference is an internal layering (6) that is not present in the polyps, such a structure presented higher backscattering. This can be clearly observed from an A-scan (Fig. 4.6c) across the layered structure that shows three clearly spaced peaks. Peak e is the epithelium while peaks f,g represent the internal layering. Hence, this structural pattern might be an indicative in order to differentiate between healthy and polyp regions. As it can be observed from the images, OCT provides subsurface visualization of mucosal and submucosal morphology compared to the limited endoscopy surface view, hence providing further histological information to attempt to differentiate between healthy tissue and polyp regions.

Fig. 4.5 and Fig. 4.6 show the capability of OCT to provide gray-scale cross-sectional sub-surface structural image data represented as backscattered light reflectivity profiles as compared to conventional endoscopy images (Fig.4.1). With the OCT images it is possible to measure the thickness of the different tissue layers in order to observe grow abnormalities as well as other internal μm features that would only develop either in polyp or healthy tissue. This is valuable information to clinicians as the cross-sectional image is equivalent to an 'optical' non-invasive biopsy.

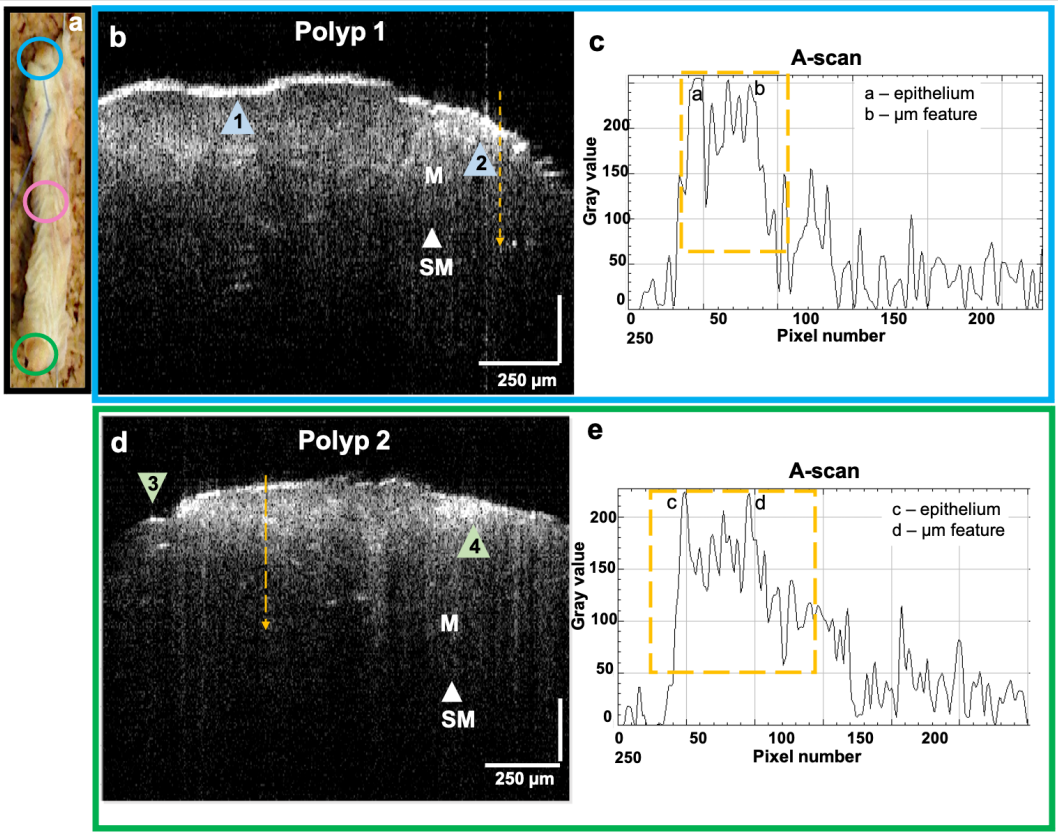

Figure 4.5: Colon sample 2 ex-vivo imaging. a) Colon sample with three imaging regions including healthy tissue and two polyps. b) Polyp 1; (1) The epithelium is clearly delineated. (2) Region with high scattered intensity underneath the epithelium. A-scan across a region with high-backscattering properties including the epithelium and μm features. d) Polyp 2; (3) Gap in the epithelium, although the subsurface structure has not been affected. (4) Region with high scattered intensity underneath the epithelium. c, e) A-scan across yellow line. The epithelium is identified as peak as well as other internal features that have similar thickness. M: Mucosa; SM: Sub-mucosa

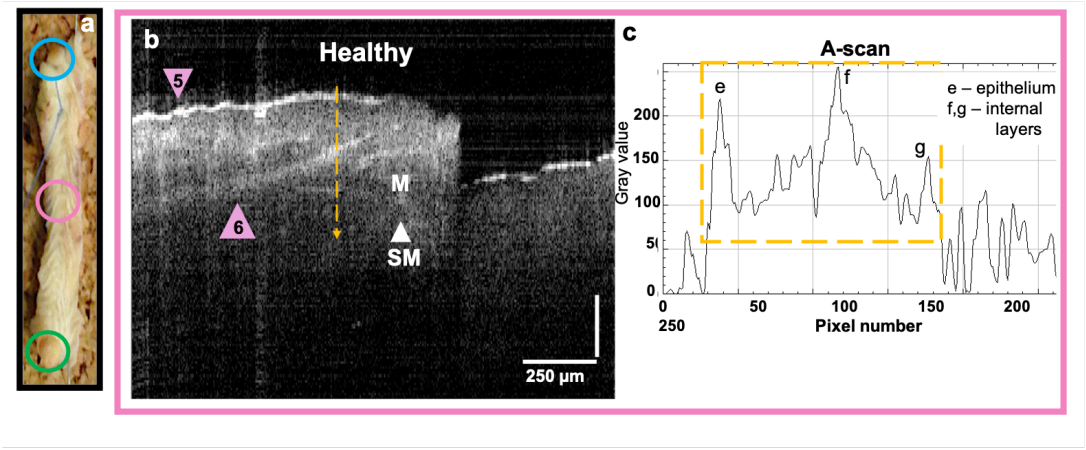

Figure 4.6: a) Colon sample with three imaging regions including healthy tissue and two polyps. b) Healthy tissue; (5) 'Bumps' in the epithelium due to the healthy tissue layered structure. (6) Internal layering not present in polyps. A-scan across three different layers including the epithelium and two internal layers. M: Mucosa; SM: Sub-mucosa

4.5 PICCOLO probe imaging

4.5.1 Rat colon ex-vivo samples

Endoscopic OCT images of ex-vivo rat colon are shown in Fig. 4.7. The imaging specifications obtained were a penetration depth of $\approx$ 1 mm with $\approx$ 7.5 μm axial resolution in tissue, and a FOV of 0.5 mm. Fig. 4.7a-c show images of an ex-vivo colon sample in the areas marked in Fig. 4.7d. Several features can be observed when comparing the subsurface structure of healthy tissue (green arrow) and deteriorated regions like unhealthy tissue (yellow arrow) and blood clot (pink arrow). For healthy tissue (Fig. 4.7a) it is possible to easily identify the front and back surfaces, while having a homogenous structure in between. In contrast, unhealthy tissue (Fig. 4.7b) has a deformation in its subsurface structure as well as reducing the penetration depth. Also, a blood clot (Fig. 4.7c) can be observed as a small bump on top of the front surface and reduce subsurface imaging depth. The ethical approval for imaging the samples was provided by the CCMIJU Animal Welfare Committee and by the Regional Government of Extremadura, Spain.

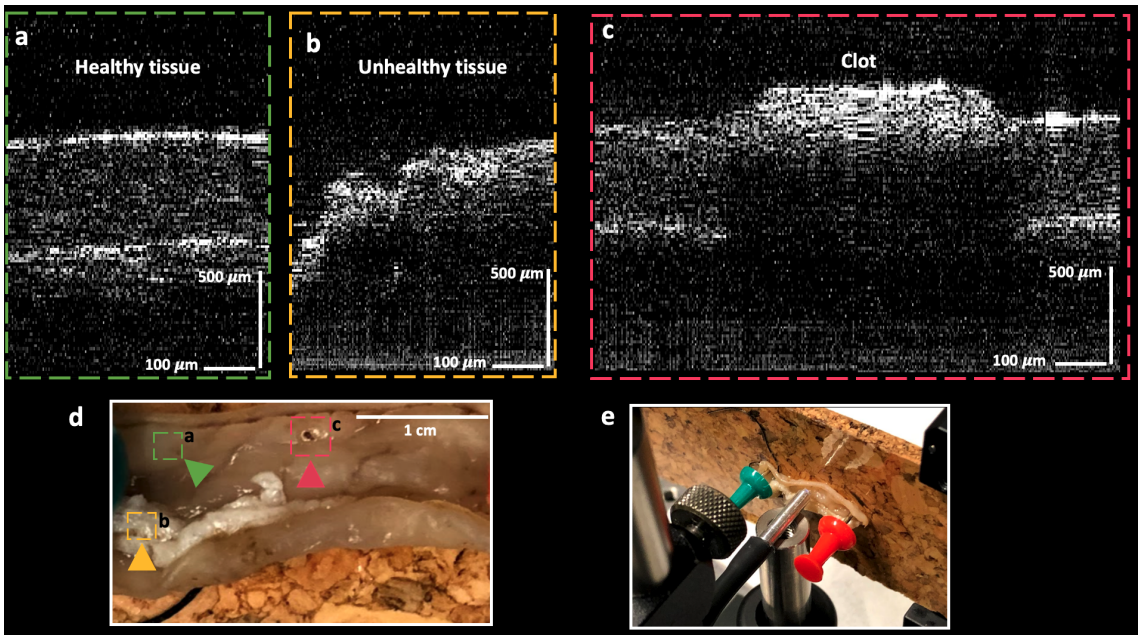

Figure 4.7: OCT B-scans of an ex-vivo colon rat sample. a) Healthy tissue where both front and back surfaces are clearly seen. b) Unhealthy tissue presents deformation of the internal layers and unsharp surface layer. c) Blood clot present in tissue. d) Ex-vivo colon rat tissue, B-scans were obtained across the line indicated by the arrows.

4.5.2 Human tissue

Figures 4.8a-h show different B-scans of a fingertip which allows identification of internal features like sweat ducts, dermis, epidermis and external features like fingerprint ridges. The internal layering including the dermis and epidermis can be clearly observed. These images are movement insensitive as they were obtained with a non-stationary finger. Fig. 4.9 shows OCT B-scans of human tissue including arm joint, nail, palm and wrist. An image penetration depth of $\approx$ 1 mm with an axial resolution of $\approx$ 7.5 μm was obtained in tissue with the endoscopic imaging probe.

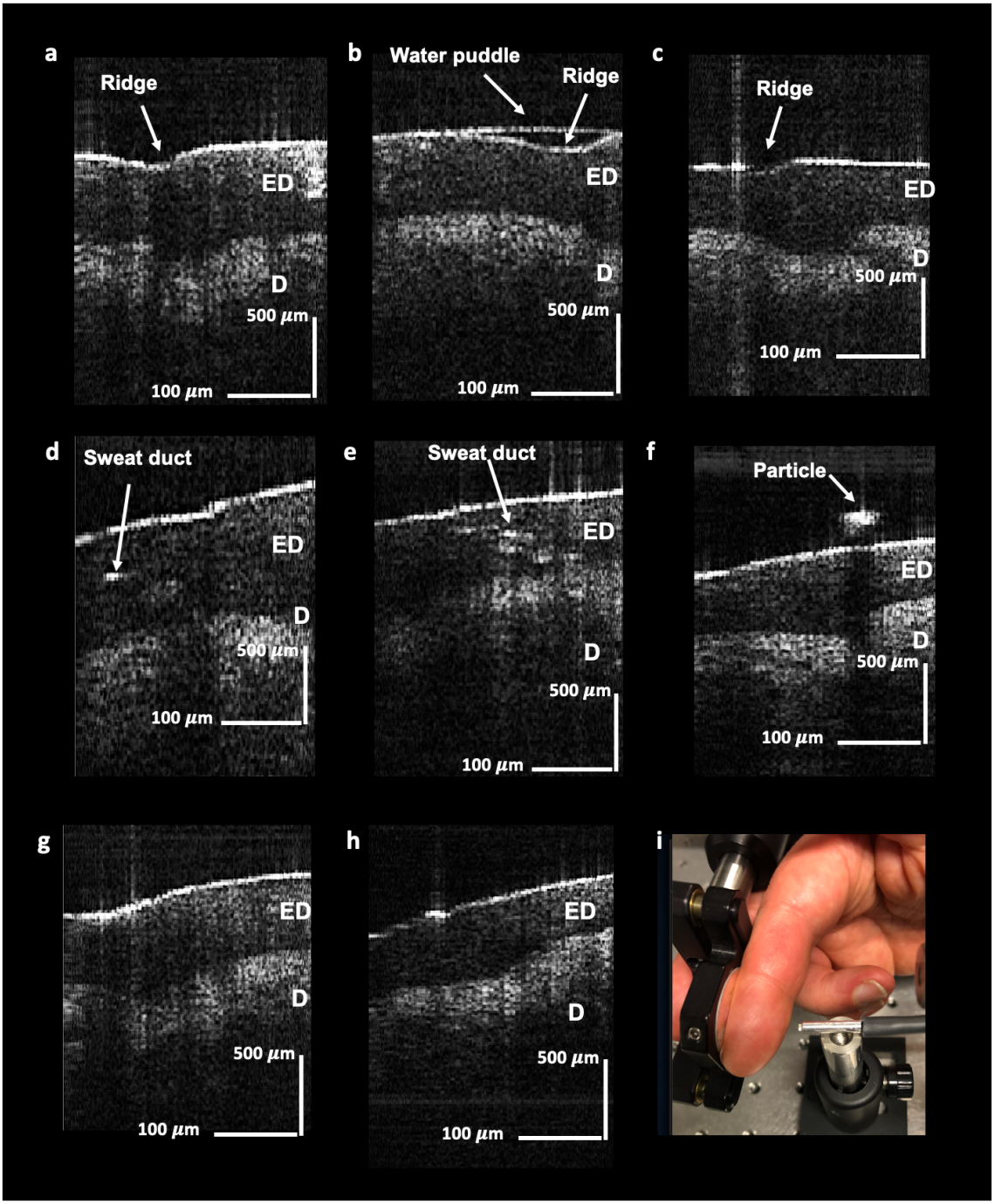

Figure 4.8: a-h) OCT B-scans of a fingertip with internal layering including dermis (D) and epidermis (ED). Other features like a water puddle (after finger is dipped in water), fingerprint ridges and internal sweat ducts can also be identified. i) Finger placement showing that the fibre scanning is fast enough to compensate for breathing motion.

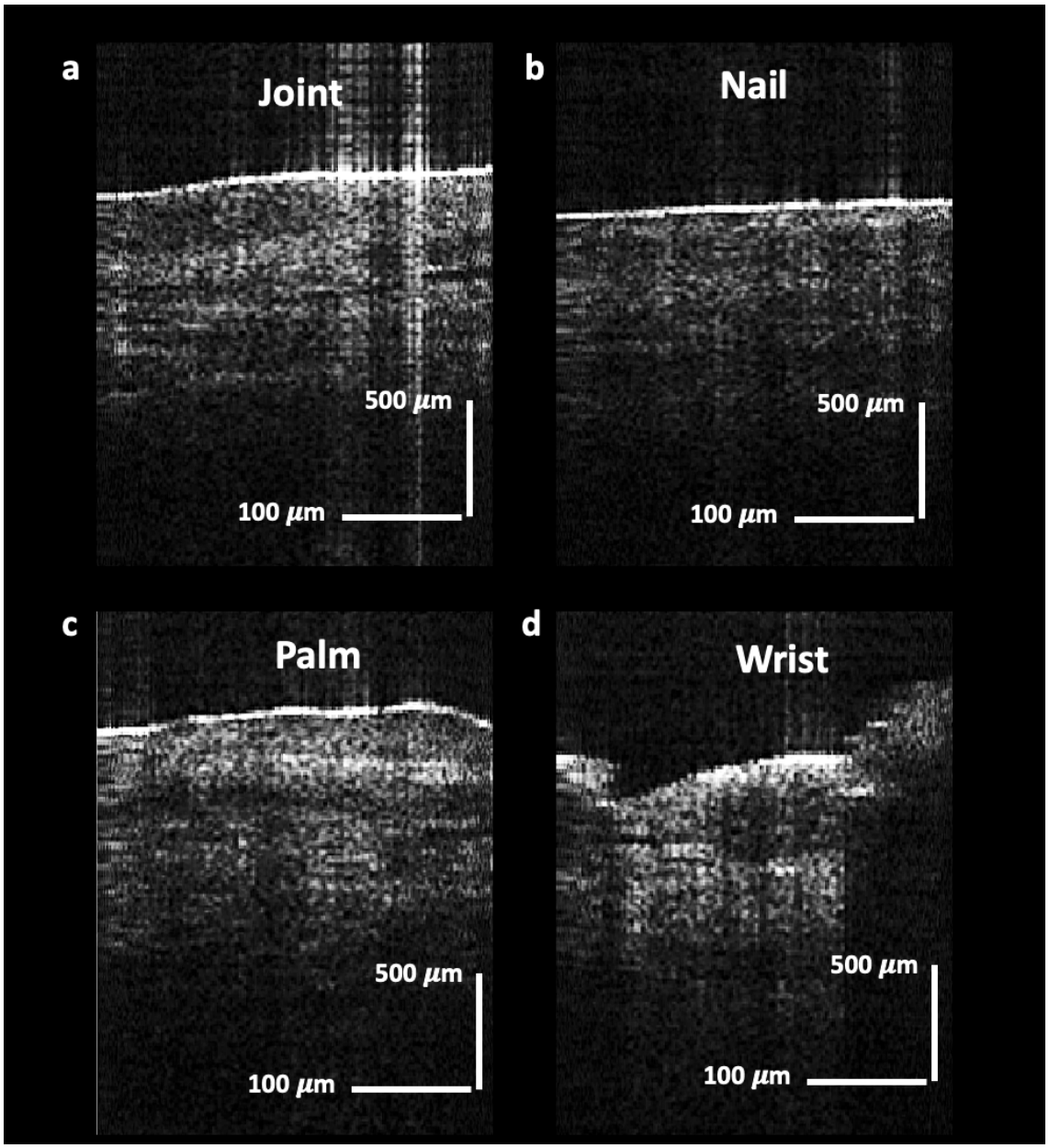

Figure 4.9: OCT B-scans of human tissue including arm joint, nail, palm and wrist. Images are movement insensitive. Images show different subsurface structure and internal layering that differentiate the images from one another.

Fig. 4.9 were acquired in real time by placing different parts of the arm at the focus of the imaging probe. The collection efficiency of the probe is good enough that in some cases the detectors are saturated. Notice how the joint, nail, palm and wrist have different subsurface structure. One common denominator for tissue that is healthy and normal is a homogeneous structure with clear layering as compared to cases with abnormal growths or defects in tissue.

The previous OCT B-scans were obtained by oscillating the fibre at the resonance frequency f = 1.4 kHz, and then interleaving three consecutive B-scans for a total of 210 A-scans per B-scan as explained in Sect. 3.3.2. The advantage of having a high scanning speed at an increased sampling density is that images are movement insensitive. Acquiring each B-scan requires 0.21 ms.

Notice that the FOV is not 1 mm as expected. The reason for this is that only half of the maximum voltage amplitude was applied to the PZT in order to operate in a safe region and avoid breaking the fibre. Despite this, the FOV is long enough to observe features such a finger ridges, sweat ducts, watter puddles and clear internal layering, therefore the obtained FOV is considered to be successful and as expected. In future work the fibre will be oscillated at its maximum amplitude by increasing the voltage range obtaining a longer FOV.

4.6 Discussion and conclusions

This chapter presented OCT imaging of biological tissue using both the translation stage and the endoscopic imaging probe. The images have proven successful integration of the SS-OCT achieved by combining the swept source, the interferometer, the signal detection, scanning mechanisms as well as software integration including algorithms for dispersion compensation, interleaving and signal synchronization. Biological OCT imaging was achieved using both scanning mechanisms obtaining an image penetration depth

of $\approx$ 1 mm with an axial resolution of $\approx$ 7.5 μm.

4.6.1 OCT imaging with the translation stage

The distinctive feature of the translation stage is the ample FOV that provides μm step resolution allowing the imaging of ex-vivo motionless samples. Despite the low scanning speed, the OCT images provided the required sub-surface image data that allowed to see internal layering as well as other μm structural features. Another advantage is that placement and imaging of the ex-vivo colon samples was simplified due to the flexible scanning range providing good control in image localization. This allows to observe the curvature and morphological changes going from healthy tissue to a polyp.

For the lesion neoplastic polyps, it was observed that these preserve a homogeneous surface structure as well as symmetric curvatures without clear inhomogeneity. The sub-surface structure is divided in the mucosa and submucosa, the first one with higher backscattered intensity, as well as having a clearly defined epithelium. This layer can be observed as the polyp develops at different stages in order to observe thickening as well as signal attenuation as an indicative of abnormal tissue. As a comparison with the polyps, healthy regions presented internal layering with more intense backscattering properties, as well as having some small 'bumps' in the epithelium due to its surface structure containing 'stripes'.

4.6.2 OCT imaging with the PICCOLO probe

The distinctive feature of the PZT fibre scanning probe is its fast scanning speed of 1.4 kHz which compensates for moving image artifacts. The fact that this will provide less sampling points was compensated with the proposed interleaving algorithm that increases the sampling resolution and final image quality requiring 0.21 ms to form the cross-sectional B-scan. OCT images were obtained with a lateral FOV of 0.5 mm, which falls within the

expected value.

Images of ex-vivo colonic tissue were successfully acquired showing the difference between healthy and unhealthy tissue as well as a blood clot. Healthy tissue presented clear layering where both the front and back surfaces can be observed. Compared to that, the unhealthy tissue presents a clear sub-surface abnormal growth. The blood clot presented high light attenuation as compared to the previous tissue types. More image data is required to identify clear biological markers that allow discrimination between healthy and abnormal tissue. Unfortunately it was not possible to acquire more polyp samples at the present time of writing this thesis due to the on-going global pandemic which limited the number of samples as well installing the OCT in a clinical setting.

4.6.3 OCT imaging as optical biopsy

The acquired cross-sectional OCT images are equivalent to a non-invasive 'optical biopsy'. The images resemble histology images without the requirement of tissue sectioning or imaging markers, hence preserving the structure of the tissue in case of in-vivo imaging. OCT provides value in medical imaging due to its in-vivo immediate imaging capabilities through the endoscopic probe without the requirement of tissue extraction.

OCT provides clear sub-surface image data to observe the internal layering of biological tissue complementing the front-view of a conventional endoscope. This shall provide more accurate and objective information for the clinician to discriminate between healthy and abnormal tissue. In practice, there are a lot of challenges for the clinicians to be familiar with the OCT images. One such a challenge is the OCT provides gray-scale images compared to conventional stained histology images. This requires clinicians to be trained and familiarized with the imaging procedure and the meaning of a cross-sectional image. Additionally, image processing algorithms to add artificial colour to the images can be implemented.

Chapter 5

Conclusions and outlook

5.1 Outcomes

The aim of this thesis was to develop and assemble novel endoscopic swept-source optical coherence tomography (OCT) system. This was accomplished through five building blocks including investigation of swept sources, OCT system design, fibre scanner optomechanical design, assembled imaging probe and OCT imaging. Several outcomes were achieved throughout this thesis including:

1. **An automated heterodyne method for DC and AC characterization of tunable lasers.** A novel method to generate a tuning dictionary to obtain linear tuning curves has been presented (Sect. 2.4.3). This includes a proposed setup as well as the controlled software developed in Labview (Sect. A.1).

2. **A dispersion compensation algorithm.** The presented algorithm coded in Scilab is capable of matching the dispersion of an interferometer to obtain high resolution axial A-scans (Sect. 3.1.6, Sect. A.3).

3. **A SS-OCT using a translation stage.** This OCT system allows acquisition of B-scans with an ample field of view of 100 x 40 mm^2 (Sect. 3.3.1).

4. **An endoscopic SS-OCT using a PZT fibre scanner.** An endoscopic imaging head using a resonant fibre PZT scanner was assembled using a GRIN lens as imaging optic. An axial resolution of 10 μm in air, with a FOV of 0.5 mm, oscillating at 1.4 kHz and with an interleaving algorithm to obtain a B-scan rate of 460 Hz. were obtained (Sect. 3.3.2). The probe can be integrated into the working channel of a conventional endoscope.

5. **OCT control software.** A fully automated software to acquire B-scans using the endoscopic probe has been programmed (Sect. A.4).

6. **OCT imaging of biological tissue**. OCT B-scans of ex-vivo colonic rat tissue as well as in human tissue were acquired obtaining a penetration depth of 1 mm at an axial resolution of 7.5 μm in tissue were obtained (Sect. 4.5).

5.2 Conclusions

5.2.1 Akinetic tunable lasers

All-semiconductor akinetic tunable laser sources are absolutely necessary to continue the development of swept sources looking forward to reduce the overall cost of an OCT. Multi-section slotted lasers proccesed in-house presented good performance in terms of an acceptable tuning range, optical power and response time being able to identify tuning paths in DC operation. However, a noise-free optical signal is yet to be produced in order to improve the dynamic performance of these devices, as required by a swept source. These lasers can be improved by adding AR coatings, as well as changing the parameters such as different edge and slot spacing.

SG-DBR telecoms laser presented a very good performance in terms of tuning range, SMSR, and optical output power with clear tuning paths in DC operation. Tuning maps

as well as tuning dictionaries were obtained. These lasers can be the core of a swept source although several factors have to be considered, such as hysteresis, temperature, and precise control electronics with extremely low noise levels. The proposed heterodyne method proved to be a useful tool to characterize the lasers electronically and optically and shall contribute to the research of akinetic swept sources. The setup can still be improved by correct impedance matching of the electronics components as well as using a faster DAQ to generate faster tuning speeds.

5.2.2 Endoscopic OCT system

The integration of the whole endoscopic system included precise optomechanical design and aligment, signal processing and data acquisition, control electronics and dedicated software. The final outcome are B-scans of biological tissue which were successfully acquired showing sub-surface structural image data with a micron resolution. The probe can be integrated into the working channel of a conventional endoscope for in-vivo imaging. The proposed interleaving algorithm was useful to increase the sampling density and finally the image quality.

5.3 Future work

One of the greatest challenges for OCT is convincing the ultimate users such as clinicians that perform conventional endoscopy of the added value of OCT as a medical imaging modality. To accomplish this future work has to be performed including:

1. An OCT imaging database using the endoscopic PICCOLO probe to identify clear biological markers. Several micron features were observed in this thesis when differentiating between healthy and unhealthy tissue, however these markers are not definite. Specificity and sensitivity of the system shall be calculated to determine

the correct biological markers.

2. Train the final users so that they are familiarized with the gray-scale cross-sectional images, compared to conventional stained histological images. An additional approach is using deep-learning algorithms that automatically identify patterns in images.

3. The developed probe is solid and stable, although hard to reassemble. A solution for this is to take the current design, but using a 3D printed approach so that the assembly is modular. This will allow a more precise integration and alignment of the elements as well as increasing the repeatability of different probes.

4. The LabView software interface can be improved by increasing the real-time B-scan update time. One of the limitations was the number of A-scans per B-scan that the card acquired. A solution for this is either choosing a different commercial card or developing dedicated acquisition software in C-code using the same acquisition card.

5. The integration of additional imaging modalities such as MPT is necessary to provide functional data on top of the structural data of OCT. This can be accomplished through a 785 nm Ti:Sa fs laser. This work will require additional trade-offs to consider in selecting the numerical aperture of the imaging lens since MPT requires a tight focus, which will reduce the imaging depth of OCT.

These are the necessary steps so that the PICCOLO endoscope probe can be used in public or private hospitals by gastroenterologists to enable immediate and detailed in situ identification through its 'optical biopsy' capabilities in order to identify colorectal neoplastic lesions. The probe shall facilitate accurate in-vivo diagnostics with grading capabilities as well as margin assessment. Other application areas include pathologies in the esophagus, stomach or small intestine.

Appendix A

Swept sources

A.1 Automated heterodyne method

The flow chart of the automated heterodyne method presented in Sect.2.4.3 is shown in the following figures. Block 1 consists of the first steps for configuring the oscilloscope and initializing the tunable laser source (TLS). After that, data is read from the scope and sent into a LabView program, the AC-Root Mean Square (RMS) value is calculated for each current combination which is composed of several scope data points. This AC-RMS value is proposed as a measure of the quality of the beating signal. Above a certain threshold the beating signal has a good quality producing a beat signal, opposite to that, the quality of the beating signal is low or there is no beating signal at all. Once the AC-RMS values are compared with the threshold, those above it are saved to a file with the corresponding current combination/coordinates that produced such wavelength. Block 2 contain the logical steps to perform a raster scanning in mirrors M1 and M2 as well as converting from current to digital numerical values.

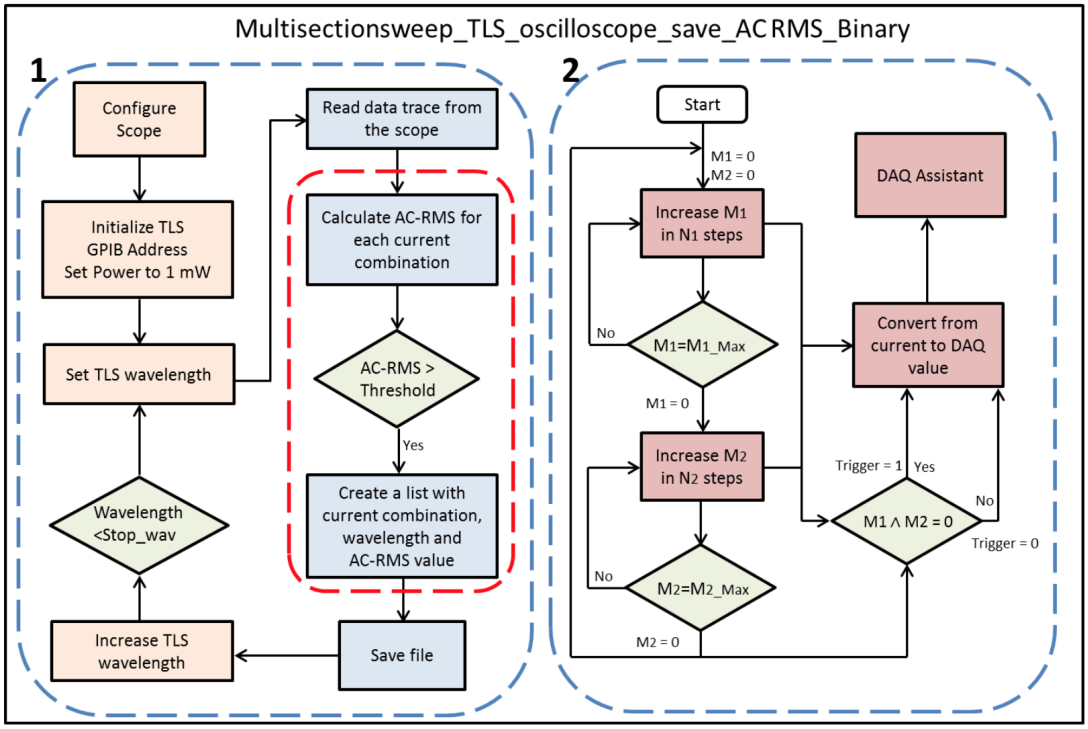

Figure A.1: Automated heterodyne method to characterize semiconductor based akinetic swept laser sources flow diagram. Block 1 representss AC-RMS calculation, while Block 2 represents how to generate a raster current pattern.

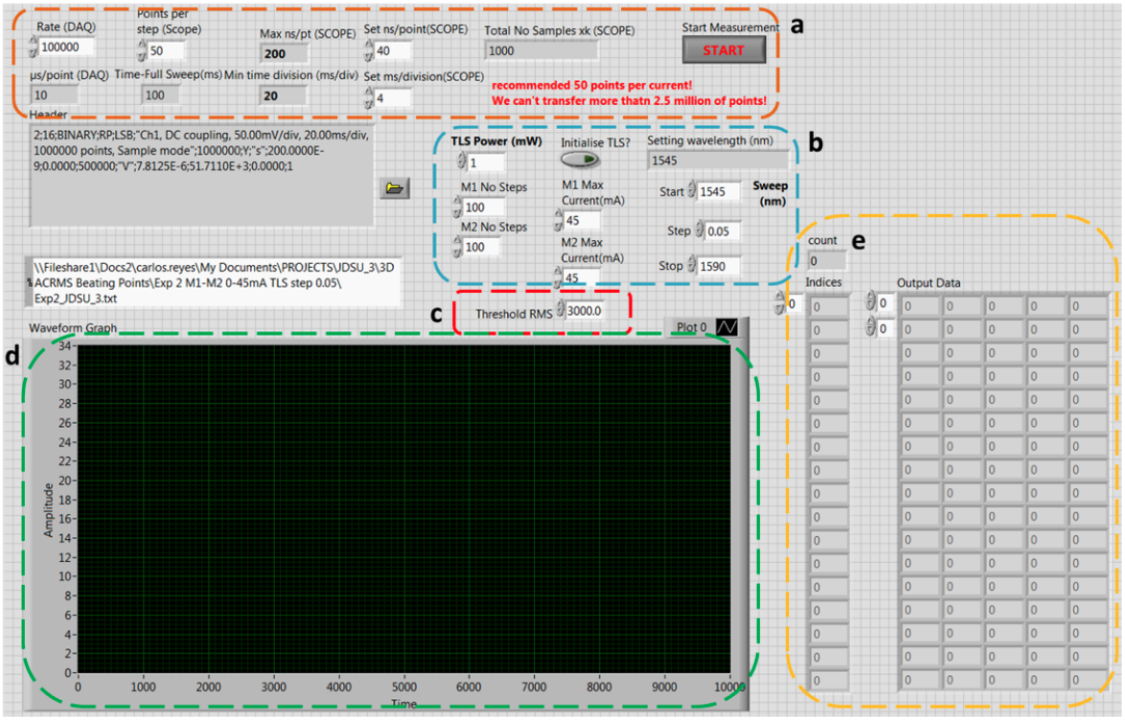

Figure A.2: a) DAQ configuration and scope setup. b) TLS Setup and current setup. c) RMS Threshold. d) Waveform Graph plot. e) Peaks that have an RMS greater than the threshold.

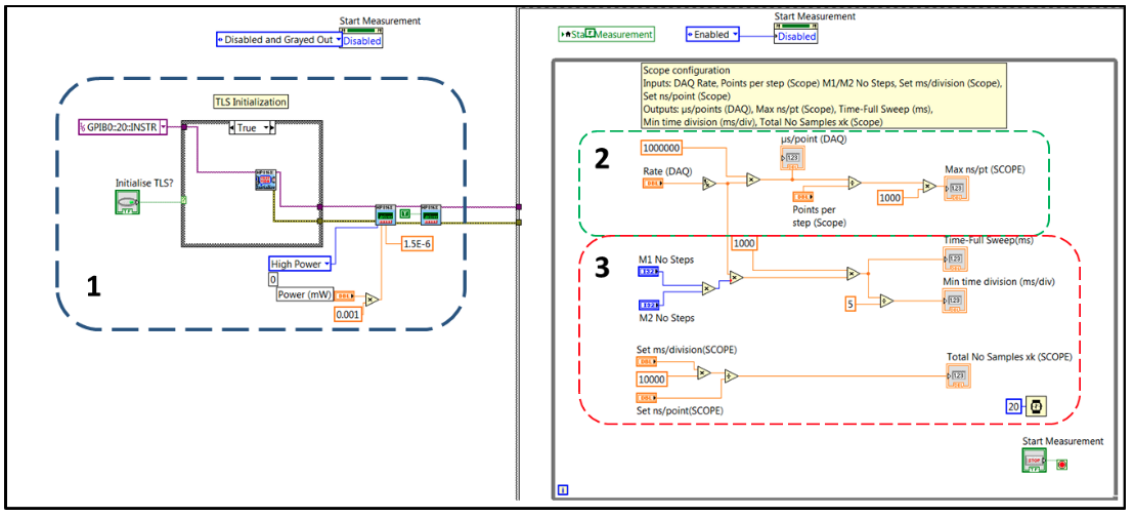

Figure A.3: 1) TLS configuration. 2) DAQ and scope configuration. 3) Total number of samples and min time per divsion of the scope.

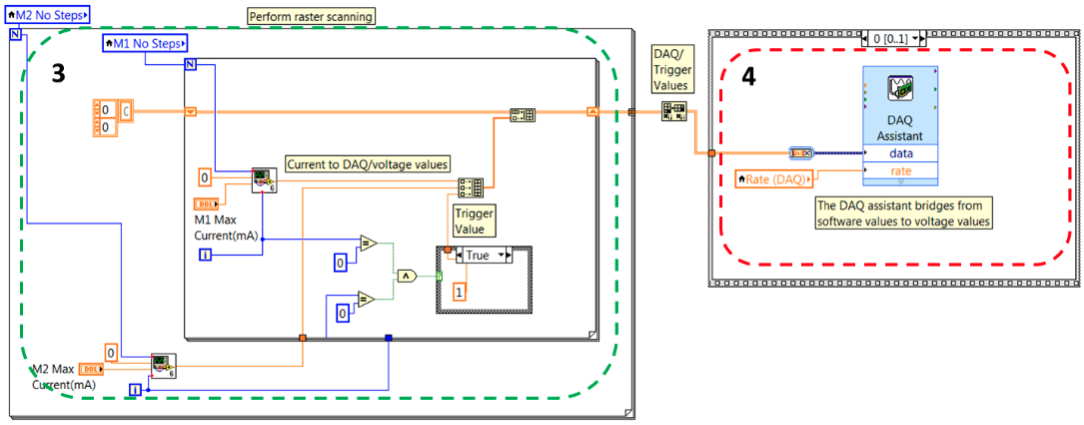

Figure A.4: 3) Block that creates a raster and trigger signal. 4) DAQ assistant block.

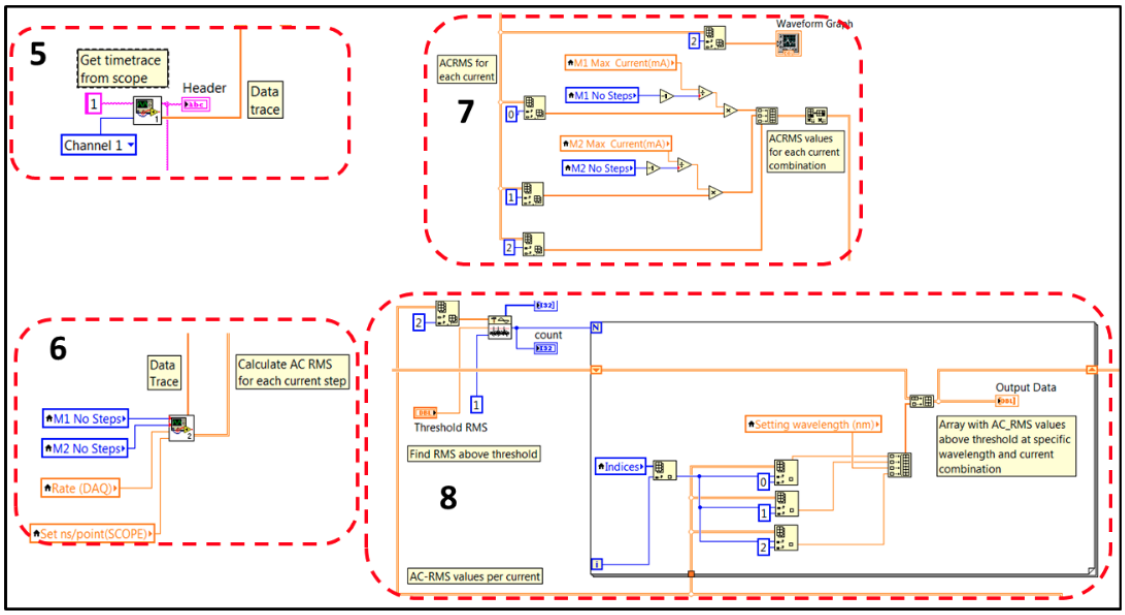

Figure A.5: 5) Sub-VI that reads the header and time/data trace from the scope. 6) Sub-VI that calculates the AC-RMS for each current step/combination. 7) Block that concatenates the AC-RMS with its respective M1/M2 current combination. 8) Find AC-RMS above threshold. The output is an array with the current combinations that are above the threshold.

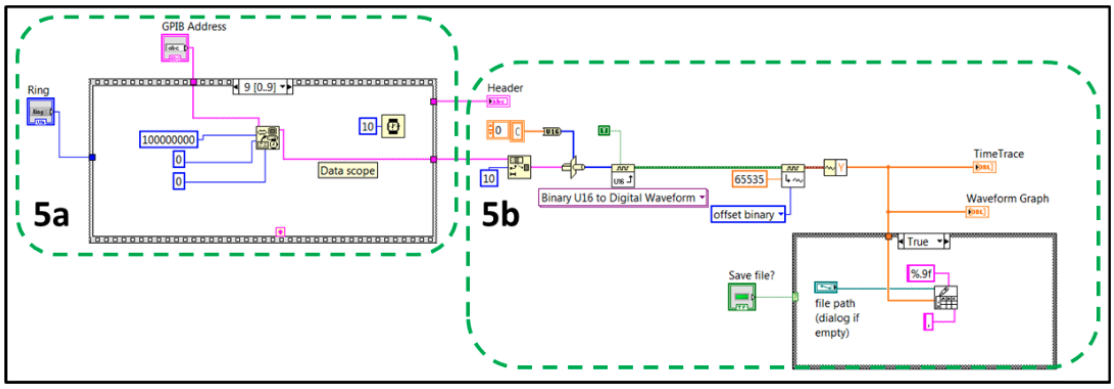

Figure A.6: 5a) Block that reads data scope and header in binary format. 5b) Block to convert from binary to analog format.

A.2 Linear filter and algorithm to generate a tuning path

The proposed heterodyne method is able to provide a tuning dictionary containing current combinations to obtain a linear sweep. However, one of the drawbacks is the measurement time as well as requiring expensive equipment. For such reason a modification of the setup includes a linear filter as a one-shot measurement technique. The main outcome are similar tuning maps but with the difference that these can be obtained faster. With these tuning maps, an algorithm is proposed in order to find a way in between the tuning paths to linearly increase the wavelength.

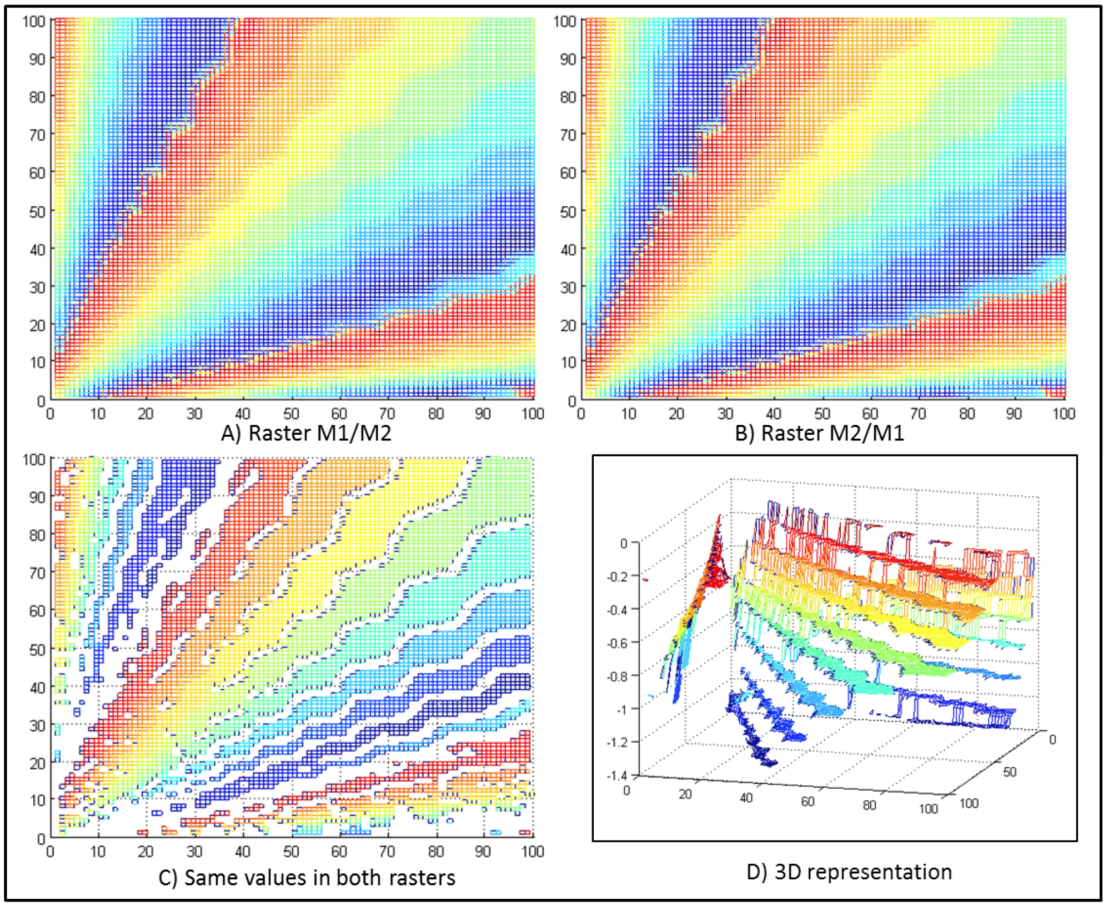

Figure A.7: A) Raster Scan M1/M2 B) Raster Scan M2/M1 C) Same values found in both scans. D) 3D representation of the tuning map.

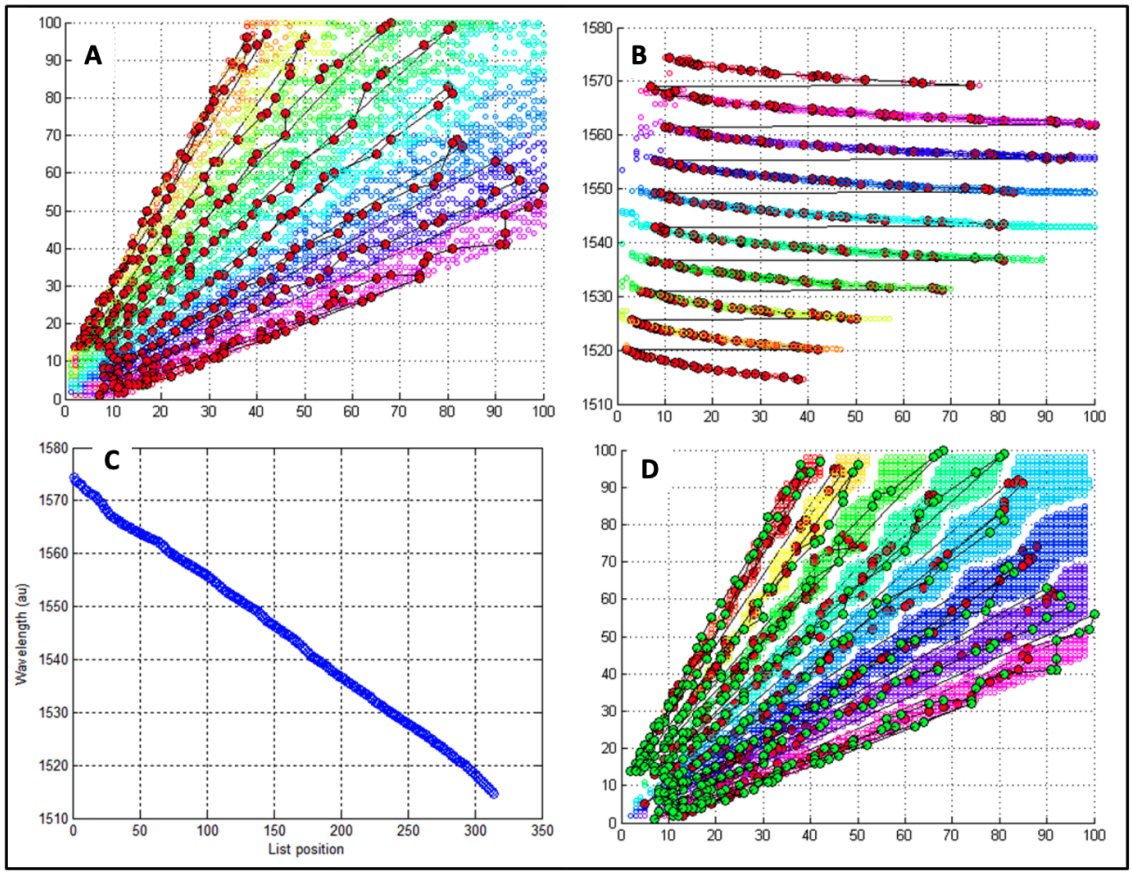

Figure A.8: A) Raster Scan M1/M2 B) Raster Scan M2/M1 C) Same values found in both scans. D) 3D representation of the tuning map.

Optical coherence tomography

A.3 Dispersion compensation and interleaving algorithms

The dispersion compensation algorithm used to match the dispersion of the arms of the interferometer was coded in Scilab and shown in Fig. A.9. The code follows the steps discussed in Fig. 3.6. The interleaving algorithm used to increase the sampling density of a B-scan acquired with the endoscopic probe is shown in Fig. A.10.

```
"""Input variables
Bscan - the Bscan to be compensated
low, high - low and high frequencies of a rectangle filter
"""
"""Output variables
Phase correction factor
Dispersion compensated A-scan
"""

# 1. Calculate the FFT of a Bscan, apply a rectangle filter
#    and inverse transform
Y = fft(Bscan)
window1 = zeros(1024, 1)
window1(low:high,:) = Y(low:high,:)
spectrum1 = ifft(window1)

# 2. Unwrap the phase
ang = atan(image(spectrum1(:,:)), real(spectrum1(:,:)))
spec1 = zeros(1024, 1)
```

```
# Phase unwrap
x = ang
y = 2*%pi.*cumsum(floor(.5+diff(ang)/2/%pi))
z = (x(2:1024) - y)
spec1 = [ang; z]
speca = spec1'

# 3. Perform a linear fit
[afit, bfit] = reglin([1:1024],speca)
lala = (afit*[1:1024] + bfit)'

# 4. Calculate correction factor
correction = spec1 - lala
correction = conv(correction, [1 1 1 1 1 1 1], "same")/7

# 5. Correct an A-scan with the correction factor
A_scan_corrected = A_scan_dispersed.*exp(-
imult(1)*correction)
OCT = 20*log10(abs(fft(A_scan_corrected)))
```

Figure A.9: Dispersion compensation algorithm programmed in Scilab.

A.4 OCT LabView interface

The main LabView interface to acquire B-scans using the endoscopic probe is shown in Fig. A.11. The interface displaces the live-view raw interferogram, its dispersion compensated FFT peak and a live-view OCT B-scan. The interface allows the acquisition of the

```
"""Interleave algorithm
Inputs:
   B-scan
   RepeatIndex - Number of A-scans/B-scan to be
interleave
   RepeatNum - Number of B-scans to interleave"""

Bave = zeros(1024, RepeatIndex*(RepeatNum)+1)
Bscanttoave = Bscan'
for rloop = 1:RepeatIndex
for skip = 0:(RepeatNum - 1)
   Bave(:, rloop*(RepeatNum)+skip+1) =
Bscantoave(:,skip*2*RepeatIndex + rloop)
   end
end
Bave = Bave'
```

Figure A.10: Interleaving algorithm to increase the sampling density resolution of a B-scan.

correction factor for the dispersion compensation as well as zero background removal. The LabView codes are shown in Fig.A.12 and Fig. A.13.

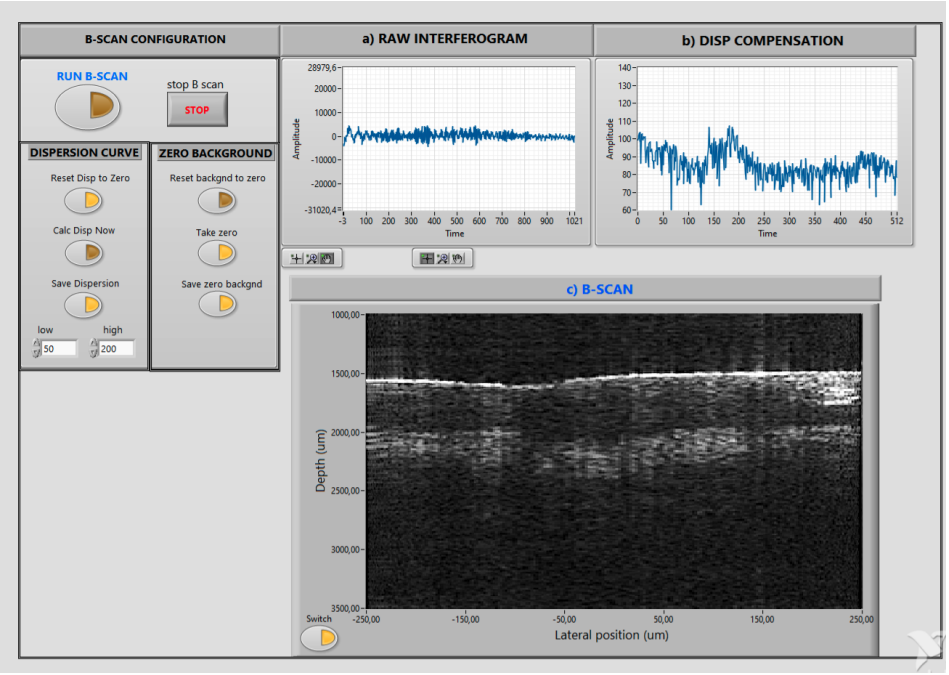

Figure A.11: Labview interface to acquire OCT B-scans. a) Live-view raw interferogram display. b) Dispersion compensated FFT peak display. c) B-scan live-view.

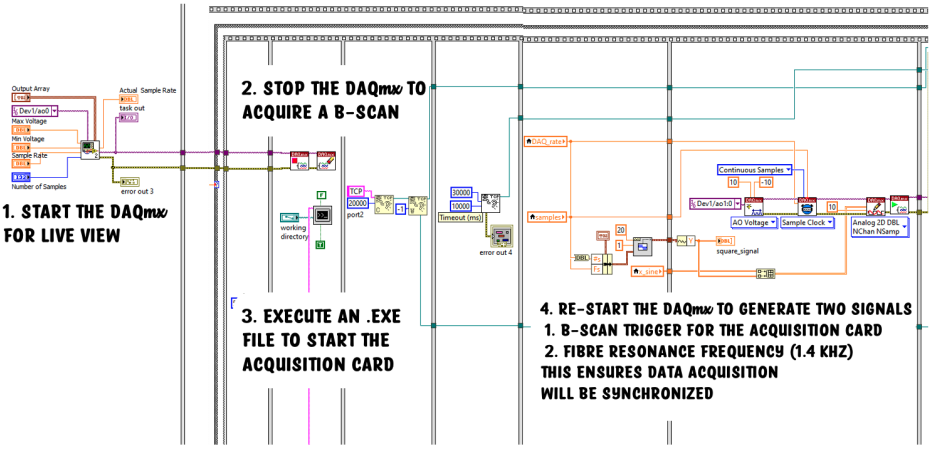

Figure A.12: LabView codes to acquire a B-scan, this includes starting a DAQmx acquisition, executing a .exe file to start the acquisition card and generating the analog signals to oscillate the PZT fibre scanner.

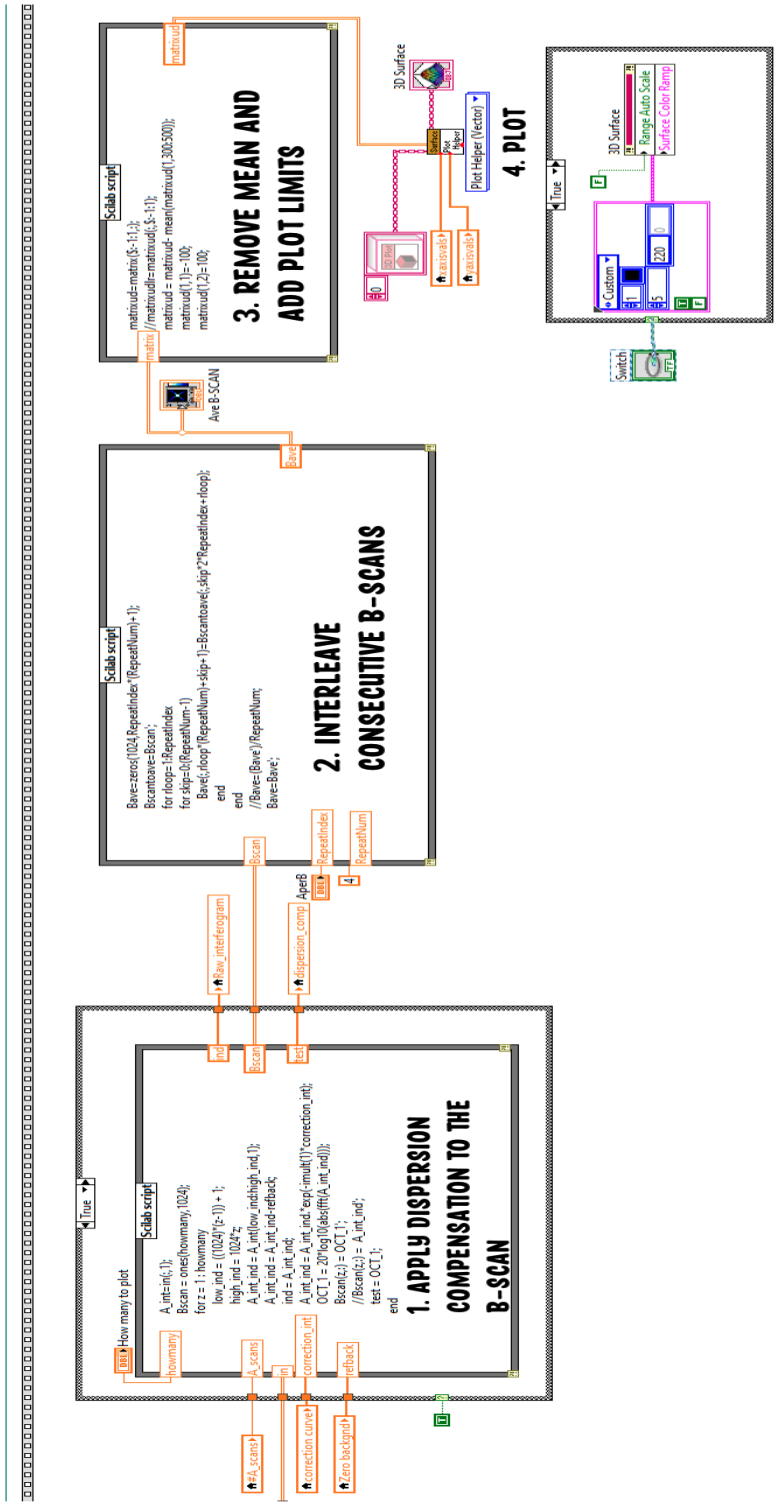

Figure A.13: Labview interface to acquire OCT B-scans. After acquiring a B-scan set the dispersion compensation algorithm is applied followed by the interleaving algorithm and finally plotting the B-scan.

Bibliography

[1] J. Fujimoto and W. Drexler. *Introduction to Optical Coherence Tomography*. Springer, 2015 (second edition).

[2] R. Chopra, S. Wagner, and P. Keane. Optical coherence tomography in the 2020s—outside the eye clinic. *Eye (Basingstoke)*, 35(1):236–243, 2021.

[3] W. Drexler and J. Fujimoto. State-of-the-art retinal optical coherence tomography. *Progress in Retinal and Eye Research*, 27(1):45–88, 2008.

[4] E. Tenekecioglu, F. Albuquerque, Y. Sotomi, Y. Zeng, P. Suwannasom, H. Tateishi, R. Cavalcante, Y. Ishibashi, S. Nakatani, M. Abdelghani, J. Dijkstra, C. Bourantas, C. Collet, A. Karanasos, M. Radu, A. Wang, T. Muramatsu, U. Landmesser, T. Okamura, E. Regar, L. Räber, G. Guagliumi, R. Pyo, Y. Onuma, and P. Serruys. Intracoronary optical coherence tomography: Clinical and research applications and intravascular imaging software overview. *Catheterization and Cardiovascular Interventions*, 89(4):679–689, 2017.

[5] Ziad A. Ali, Keyvan Karimi Galougahi, Akiko Maehara, Richard A. Shlofmitz, Ori Ben-Yehuda, Gary S. Mintz, and Gregg W. Stone. Intracoronary Optical Coherence Tomography 2018: Current Status and Future Directions. *JACC: Cardiovascular Interventions*, 10(24):2473–2487, 2017.

[6] Jonas Olsen, Jon Holmes, and Gregor B. E. Jemec. Advances in optical coherence tomography in dermatology—a review. *Journal of Biomedical Optics*, 23(04):1, 2018.

[7] B. Wan, C. Ganier, X. Du-Harpur, N. Harun, F. M. Watt, R. Patalay, and M. D. Lynch. Applications and future directions for optical coherence tomography in dermatology. *British Journal of Dermatology*, pages 1–9, 2020.

[8] Oscar M. Carrasco-Zevallos, Christian Viehland, Brenton Keller, Mark Draelos, Anthony N. Kuo, Cynthia A. Toth, and Joseph A. Izatt. Review of intraoperative optical coherence tomography: technology and applications [Invited]. *Biomedical Optics Express*, 8(3):1607, 2017.

[9] Jianfeng Wang, Yang Xu, and Stephen A. Boppart. Review of optical coherence tomography in oncology. *Journal of Biomedical Optics*, 22(12):1, 2017.

[10] Zahid Yaqoob, Jigang Wu, Emily J. McDowell, Xin Heng, and Changhuei Yang. Methods and application areas of endoscopic optical coherence tomography. *Journal of Biomedical Optics*, 11(6):063001, 2006.

[11] Michalina J. Gora, Melissa J. Suter, Guillermo J. Tearney, and Xingde Li. Endoscopic optical coherence tomography: technologies and clinical applications [Invited]. *Biomedical Optics Express*, 8(5):2405, 2017.

[12] Tejas S. Kirtane and Mihir S. Wagh. Endoscopic optical coherence tomography (OCT): Advances in gastrointestinal imaging. *Gastroenterology Research and Practice*, 2014, 2014.

[13] T. Tsai, C. Leggett, A. Trindade, A. Sethi, A. Swager, V. Joshi, J. Bergman, H. Mashino, N. Nishioka, and E. Namati. Optical coherence tomography in gastroenterology: a review and future outlook. *Journal of Biomedical Optics*, 22(12):1, 2017.

[14] J. E. Freund, M. Buijs, C. D. Savci-Heijink, D.M. de Bruin, J. J. M. C. H. de la Rosette T. G. van Leeuwen, and M.P. Laguna. Optical Coherence Tomography in Urologic Oncology: a Comprehensive Review. *SN Comprehensive Clinical Medicine*, 1(2):67–84, 2019.

[15] James G Fujimoto. Biomedical imaging and optical biopsy using optical coherence tomography. pages 970–972, 1995.

[16] Brezinski. M, G. Tearney, B. Bouma, J. Izatt, M. Hee, R. Michael, E. Swanson, J. Southern, and J. Fujimoto. Optical coherence tomography for optical biopsy: Properties and demonstration of vascular pathology. *Circulation*, 93(6):1206–1213, 1996.

[17] J. Fujimoto, C. Pitris, S. Boppart, and M. Brezinski. Optical coherence tomography: An emerging technology for biomedical imaging and optical biopsy. *Neoplasia*, 2(1-2):9–25, 2000.

[18] D. Huang, E. Swanson, C. Lin, J. Schuman, W. Stinson, W. Chang, M. Hee, T. Flotte, K. Gregory, C. Puliafito, and J. Fujimoto. Optical coherence tomography. *Science*, 254:1178–1181, Nov 1991.

[19] A. Fercher, C. Hitzenberger, G. Kamp, and S. El-Zaiat. Measurement of intraocular distances by backscattering spectral interferometry. *Optics communications*, 117:43–48, May 1995.

[20] M. Wojtkowski, R. Leitgeb, A. Kowalczyk, T. Bajraszewski, and A. Fercher. In vivo human retinal imaging by fourier domain optical coherence tomography. *Journal of Biomedical Optics*, 7(3):457–463, July 2002.

[21] R. Leitgeb, C. Hitzenberger, and A. Fercher. Performance of fourier domain vs time domain optical coherence tomography. *Optics Express*, 11(8):889–894, March 2003.

[22] S. Chinn and J. Fujimoto E. Swanson. Optical coherence tomography using a frequency-tunable optical source. *Optics Letters*, 22:340–342, March 1997.

[23] B. Golubovic, B. Bouma, G. Tearney, and J. Fujimoto. Optical frequency-domain reflectometry using rapid wavelength tuning of a cr4+:forsterite laser. *Optics Letters*, 22:1704–1706, November 1997.

[24] F. Lexer, C. Hitzenberger, A. Fercher, and M. Kulhavy. Wavelength-tuning interferometry of intraocular distances. *Applied Optics*, 36, No. 25:6548–6553, September 1997.

[25] H. Hiratsuka, E. Kido, and T. Yoshimura. Simultaneous measurements of three-dimensional reflectivity distributions in scattering media based on optical frequency-domain reflectivity. *Optics Letters*, 23, No. 18:1420–1422, September 1998.

[26] J. DeBoer, R. Leitgeb, and M. Wojtkowski. Twenty-five years of optical coherence tomography: the paradigm shift in sensitivity and speed provided by fourier domain oct. *Biomedical Optics Express*, Vol. 8, No. 7:3248–3280, July 2017.

[27] Freddie Bray, Jacques Ferlay, Isabelle Soerjomataram, Rebecca L. Siegel, Lindsey A. Torre, and Ahmedin Jemal. Global cancer statistics 2018: GLOBOCAN estimates of incidence and mortality worldwide for 36 cancers in 185 countries. *CA: A Cancer Journal for Clinicians*, 68(6):394–424, 2018.

[28] Rebecca L. Siegel, Kimberly D. Miller, and Ahmedin Jemal. Cancer statistics, 2019. *CA: A Cancer Journal for Clinicians*, 69(1):7–34, 2019.

[29] Rebecca L. Siegel, Kimberly D. Miller, Ann Goding Sauer, Stacey A. Fedewa, Lynn F. Butterly, Joseph C. Anderson, Andrea Cercek, Robert A. Smith, and Ahmedin Jemal. Colorectal cancer statistics, 2020. *CA: A Cancer Journal for Clinicians*, 70(3):145–164, 2020.

[30] Andrew W. Swartz, Jan M. Eberth, and Scott M. Strayer. Preventing colorectal cancer or early diagnosis: Which is best? A re-analysis of the U.S. Preventive Services Task Force Evidence Report. *Preventive Medicine*, 118(October 2018):104–112, 2019.

[31] Gabriella Buccafusca, Ilaria Proserpio, Antonino Carmelo Tralongo, Sebastiano Rametta Giuliano, and Paolo Tralongo. Early colorectal cancer: diagnosis, treatment and survivorship care. *Critical Reviews in Oncology/Hematology*, 136(January):20–30, 2019.

[32] Rajib Ahmed, Krieshshanthan Santhirakumar, Haider Butt, and Ali K. Yetisen. Colonoscopy technologies for diagnostics and drug delivery. *Medical Devices & Sensors*, 2(3-4):1–16, 2019.

[33] Perry J. Pickhardt, Pamela A. Nugent, Pauline A. Mysliwiec, J. Richard Choi, and William R. Schindler. Location of adenomas missed by optical colonoscopy. *Annals of Internal Medicine*, 141(5), 2004.

[34] Jeroen C. Van Rijn, Johannes B. Reitsma, Jaap Stoker, Patrick M. Bossuyt, Sander J. Van Deventer, and Evelien Dekker. Polyp miss rate determined by tandem colonoscopy: A systematic review. *American Journal of Gastroenterology*, 101(2):343–350, 2006.

[35] Nam Hee Kim, Yoon Suk Jung, Woo Shin Jeong, Hyo Joon Yang, Soo Kyung Park, Kyuyong Choi, and Dong Il Park. Miss rate of colorectal neoplastic polyps and risk factors for missed polyps in consecutive colonoscopies. *Intestinal Research*, 15(3):411–418, 2017.

[36] Eric A. Swanson and James G. Fujimoto. The ecosystem that powered the translation of OCT from fundamental research to clinical and commercial impact [Invited]. *Biomedical Optics Express*, 8(3):1638, 2017.

[37] C. Minke B. Winkens A. Masclee A. Reumkens, E. Rondagh and S. Sanduleanu. Post-colonoscopy complications: a systematic review, time trends, and meta-analysis of population-based studies. *Clynical systematic reviews*, (111):1092–111, 2015.

[38] T. Seerden Y. Backes and R. Van Gestel. Can colonoscopy sow the seeds of colorectal cancer? *Translational Gastroenterology Unit John Radcliffe Hospital and University of Oxford*, pages 1192–1195, 2019.

[39] Jessica Mavadia, Jiefeng Xi, Yongping Chen, and Xingde Li. An all-fiber-optic endoscopy platform for simultaneous OCT and fluorescence imaging. *Biomedical Optics Express*, 3(11):2851, 2012.

[40] Kaicheng Liang, Giovanni Traverso, Hsiang-Chieh Lee, Osman Oguz Ahsen, Zhao Wang, Benjamin Potsaid, Michael Giacomelli, Vijaysekhar Jayaraman, Ross Barman, Alex Cable, Hiroshi Mashimo, Robert Langer, and James G. Fujimoto. Ultrahigh speed en face OCT capsule for endoscopic imaging. *Biomedical Optics Express*, 6(4):1146, 2015.

[41] Hsiang-Chieh Lee, Osman Oguz Ahsen, Kaicheng Liang, Zhao Wang, Cody Cleveland, Lucas Booth, Benjamin Potsaid, Vijaysekhar Jayaraman, Alex E. Cable, Hiroshi Mashimo, Robert Langer, Giovanni Traverso, and James G. Fujimoto. Circumferential optical coherence tomography angiography imaging of the swine esophagus using a micromotor balloon catheter. *Biomedical Optics Express*, 7(8):2927, 2016.

[42] Michael V. Sivak, Kenji Kobayashi, Joseph A. Izatt, Andrew M. Rollins, R. Ungrunyawee, Amitabh Chak, Richard C.K. Wong, Gerard A. Isenberg, and Joseph Willis. High-resolution endoscopic imaging of the GI tract using optical coherence tomography. *Gastrointestinal Endoscopy*, 51(4 I):474–479, 2000.

[43] Victor X.D. Yang, Shou Jiang Tang, Maggie L. Gordon, Bing Qi, Geoffrey Gardiner, Maria Cirocco, Paul Kortan, Gregory B. Haber, Gabor Kandel, I. Alex Vitkin,

Brian C. Wilson, and Norman E. Marcon. Endoscopic Doppler optical coherence tomography in the human GI tract: Initial experience. *Gastrointestinal Endoscopy*, 61(7):879–890, 2005.

[44] Seok H. Yun, Guillermo J. Tearney, Benjamin J. Vakoc, Milen Shishkov, Wang Y. Oh, Adrien E. Desjardins, Melissa J. Suter, Raymond C. Chan, John A. Evans, Ik Kyung Jang, Norman S. Nishioka, Johannes F. De Boer, and Brett E. Bouma. Comprehensive volumetric optical microscopy in vivo. *Nature Medicine*, 12(12):1429–1433, 2006.

[45] Lida P. Hariri, Matthew B. Applegate, Mari Mino-Kenudson, Eugene J. Mark, Benjamin D. Medoff, Andrew D. Luster, Brett E. Bouma, Guillermo J. Tearney, and Melissa J. Suter. Volumetric optical frequency domain imaging of pulmonary pathology with precise correlation to histopathology. *Chest*, 143(1):64–74, 2013.

[46] P. R. Herz, Y. Chen, A. D. Aguirre, K. Schneider, P. Hsiung, J. G. Fujimoto, K. Madden, J. Schmitt, J. Goodnow, and C. Petersen. Micromotor endoscope catheter for in vivo, ultrahigh-resolution optical coherence tomography. *Optics Letters*, 29(19):2261, 2004.

[47] Peter H. Tran, David S. Mukai, Matthew Brenner, and Zhongping Chen. In vivo endoscopic optical coherence tomography by use of a rotational microelectromechanical system probe. *Optics Letters*, 29(11):1236, 2004.

[48] Jianan Li, Mattijs de Groot, Frank Helderman, Jianhua Mo, Johannes M. A. Daniels, Katrien Grünberg, Tom G. Sutedja, and Johannes F. de Boer. High speed miniature motorized endoscopic probe for optical frequency domain imaging. *Optics Express*, 20(22):24132, 2012.

[49] Tsung-Han Tsai, Benjamin Potsaid, Yuankai K. Tao, Vijaysekhar Jayaraman, James Jiang, Peter J. S. Heim, Martin F. Kraus, Chao Zhou, Joachim Hornegger, Hiroshi

Mashimo, Alex E. Cable, and James G. Fujimoto. Ultrahigh speed endoscopic optical coherence tomography using micromotor imaging catheter and VCSEL technology. *Biomedical Optics Express*, 4(7):1119, 2013.

[50] Yeong-Hyeon Seo, Kyungmin Hwang, Hyeon-Cheol Park, and Ki-Hun Jeong. Electrothermal MEMS fiber scanner for optical endomicroscopy. *Optics Express*, 24(4):3903, 2016.

[51] Matthew Strathman, Yunbo Liu, Xingde Li, and Lih Y. Lin. Dynamic focus-tracking MEMS scanning micromirror with low actuation voltages for endoscopic imaging. *Optics Express*, 21(20):23934, 2013.

[52] Yingtian Pan, Huikai Xie, and Gary K. Fedder. Endoscopic optical coherence tomography based on a microelectromechanical mirror. *Optics Letters*, 26(24):1966, 2001.

[53] Xiumei Liu, Yuchuan Chen, Michael J. Cobb, and Xingde Li. Rapid-scanning miniature endoscope for real-time forward-imaging optical coherence tomography. *OSA Trends in Optics and Photonics Series*, 96 A(15):1659–1660, 2004.

[54] Li Huo, Jiefeng Xi, Yicong Wu, and Xingde Li. Forward-viewing resonant fiber-optic scanning endoscope of appropriate scanning speed for 3D OCT imaging. *Optics Express*, 18(14):14375, 2010.

[55] Sucbei Moon, Sang-Won Lee, Marc Rubinstein, Brian J. F. Wong, and Zhongping Chen. Semi-resonant operation of a fiber-cantilever piezotube scanner for stable optical coherence tomography endoscope imaging. *Optics Express*, 18(20):21183, 2010.

[56] Ning Zhang, Tsung-Han Tsai, Osman O. Ahsen, Kaicheng Liang, Hsiang-Chieh Lee, Ping Xue, Xingde Li, and James G. Fujimoto. Compact piezoelectric transducer fiber scanning probe for optical coherence tomography. *Optics Letters*, 39(2):186, 2014.

[57] Kristen L. Lurie, Abhijit A. Gurjarpadhye, Eric J. Seibel, and Audrey K. Ellerbee. Rapid scanning catheterscope for expanded forward-view volumetric imaging with optical coherence tomography. *Optics Letters*, 40(13):3165, 2015.

[58] Kaicheng Liang, Osman O. Ahsen, Zhao Wang, Hsiang-Chieh Lee, Wenxuan Liang, Benjamin M. Potsaid, Tsung-Han Tsai, Michael G. Giacomelli, Vijaysekhar Jayaraman, Hiroshi Mashimo, Xingde Li, and James G. Fujimoto. Endoscopic forward-viewing optical coherence tomography and angiography with MHz swept source. *Optics Letters*, 42(16):3193, 2017.

[59] Sergio Vilches, Simon Kretschmer, Cağlar Ataman, and Hans Zappe. Miniaturized Fourier-plane fiber scanner for OCT endoscopy. *Journal of Micromechanics and Microengineering*, 27(10), 2017.

[60] Lara M. Wurster, Ronak N. Shah, Fabian Placzek, Simon Kretschmer, Michael Niederleithner, Laurin Ginner, Jason Ensher, Michael P. Minneman, Erich E. Hoover, Hans Zappe, Wolfgang Drexler, Rainer A. Leitgeb, and Çağlar Ataman. Endoscopic optical coherence tomography angiography using a forward imaging piezo scanner probe. *Journal of Biophotonics*, 12(4), 2019.

[61] M. Duelk and K. Hsu. *SLEDs and Swept Source Laser Technonology for OCT in in Optical Coherence Tomography and Applications*. Springer, Switzerland, 2015 (second edition).

[62] S. Hyun and B. Bouma. *Chapter 20 Wavelength Swept Lasers in Optical Coherence Tomography and Applications*. Springer, Switzerland, 2015 (second edition).

[63] Michael A. Choma, Kevin Hsu, and Joseph A. Izatt. Swept source optical coherence tomography using an all-fiber 1300-nm ring laser source. *Journal of Biomedical Optics*, 10(4):044009, 2005.

[64] Tsung-Han Tsai, Chao Zhou, Desmond C. Adler, and James G. Fujimoto. Frequency comb swept lasers. *Optics Express*, 17(23):21257, 2009.

[65] R. Huber, D. C. Adler, V. J. Srinivasan, and J. G. Fujimoto. Fourier domain mode locking at 1050 nm for ultra-high-speed optical coherence tomography of the human retina at 236,000 axial scans per second. *Optics Letters*, 32(14):2049, 2007.

[66] Robert Huber. Fourier domain mode locking (FDML): A new laser operating regime and applications for biomedical imaging, profilometry, ranging and sensing. *Optics InfoBase Conference Papers*, 14(8):1981–1983, 2009.

[67] M. Kuznetsov, W. Atia, B. Johnson, and D. Flanders. Compact ultrafast reflective fabry-perot tunable lasers for oct imaging applications. *SPIE proceedings*, 7554:1F–1:6, Feb 2010.

[68] S. Gloor, A. Bachmann, M. Epitaux, T. von Niederhusern, P. Vorreau, N. Matuschek, K. Hsu, M. Duelk, and C. Vlez. High-speed miniaturized swept sources based on resonant MEMS mirros and diffraction gratings. *Proceedings of SPIE*, (8571):85712x–1, 2013.

[69] V. Jayaraman, J. Jiang, H. Li, P. J.S. Heim, G. D. Cole, B. Potsaid, J. G. Fujimoto, and A. Cable. OCT imaging up to 760 kHz axial scan rate using single-mode 1310nm MEMS-tunable VCSELs with >100nm tuning range. *Optics InfoBase Conference Papers*, 32(9):1888–1889, 2011.

[70] V. Jayaram, J. Jiang, B. Potsaid, M. Robertson, P. Heim, C. Burgner, D. John, G. Cole, I. Grulkowski, J. Fujimoto, A. Davis, and A. Cable. *VCSEL Swept Light Sources in Optical Coherence Tomography and Applications*. Springer, Switzerland, 2015 (second edition).

[71] M. Minneman, J. Ensher, M. Crawford, and D. Derickson. All-semiconductor high-speed akinetic swept-source for oct. *Optical Sensors and Biophotonics*, Vol. 8311, 2011.

[72] W. Drexler, M. Liu, A. Kumar, T. Kamali, A. Unterhuber, and R. Leitgeb. Optical coherence tomography today: speed, contrast, and multimodality. *Biomedical Optics*, 19, No. 7:071412:1–34, 2014.

[73] T. Klein and R. Huber. High-speed oct light sources and systems. *Biomedical Optics Express*, 8, No. 2:828–859, February 2017.

[74] Axsun Technologies. OCT Swept Laser Engines. Available at https://www.excelitas.com/product/high-speed-ss-oct-tunable-laser-engines. (Accessed: 24 May 2021).

[75] EXALOS. Swept Sources. Available at http://www.exalos.com/swept-source/. (Accessed: 24 May 2021).

[76] NTT. 200-KHz Swept Light Source for OCT Imaging. Available at https://www.ntt-at.com/product/ktn_oct/. (Accessed: 24 May 2021).

[77] Santec. Laser for Swept Source OCT. Available at https://www.santec.com/en/products/oct/lasers-for-swept-source-oct/. (Accessed: 24 May 2021).

[78] Thorlabs. 1300 nm MEMS-VCSEL Swept Source OCT Imaging System, 100 KHz. Available at https://www.thorlabs.com/. (Accessed: 24 May 2021).

[79] Superlum. Swept Wavelength Tunable Semiconductor Lasers, Broadsweepers. Available at https://www.superlumdiodes.com/broadsweepers.htm. (Accessed: 24 May 2021).

[80] Optores. Next generation FDML Laser. Available at `https://www.optores.com/`. (Accessed: 24 May 2021).

[81] InsightPhotonics. Insight Akinetic Swept Lasers Enabling OCT and SS-OCT Angiography. Available at `https://www.sweptlaser.com/`. (Accessed: 24 May 2021).

[82] M. Bonesi, M. P. Minneman, J. Ensher, B. Zabihian, H. Sattmann, P. Boschert, E. Hoover, R. A. Leitgeb, M. Crawford, and W. Drexler. Akinetic all-semiconductor programmable swept-source at 1550 nm and 1310 nm with centimeters coherence length. *Opt. Express*, 22:2632–2655, Feb 2014.

[83] Z. Chen, M. Liu, M. Minneman, L. Ginner, E. Hoover, H. Sattmann, M. Bonesi, W. Drexler, and R. Leitgeb. Phase-stable swept source oct angiography in human skin using an akinetic source. *Biomedical Opt. Express*, 7, No. 8:3032–3048, Aug 2016.

[84] M. Salas, M. Augustin, F. Felberer, A. Wartak, M. Laslandes, L. Ginner, M. Niederleithner, J. Ensher, M. Minneman, R. Leitgeb, W. Drexler, X. Levecq, U. Schmidt-Erfurth, and M. Pircher. Phase-stable swept source oct angiography in human skin using an akinetic source. *Biomedical Opt. Express*, 7, No. 8:3032–3048, Aug 2016.

[85] W. Atia, M. Kuznetsov, and D. Flanders. Linearized swept laser source for optical coherence analysis system. US Patent App., vol 12/027710. (2009).

[86] B. Johnson and D. Flanders. Laser swept source with controlled mode-locking for OCT medical imaging. US Patent App., vol 12/092290. (2012).

[87] A. Maini. *Lasers and Optoelectronics: Fundamentals, Devices and Applications*. John Wiley and Sons, 2013.

[88] Mark W. Fleming and Aram Mooradian. Spectral Characteristics of External-Cavity. *Quantum Electronics, IEEE Journal ... IEEE Journal of*, 17(1):44–59, 1981.

[89] D. Flanders, M. Kuznetsov, and W. Atia. Laser with tilted multi-spatial mode resonator tuning element. US Patent App., vol 11/158417. (2008).

[90] B. Johnson, W. Atia, M. Kuznetsov, C. Cook, B. Goldberg, B. Wells, N. Larson, E. McKenzie, C. Melendez, E. Mallon, S. Woo, R. Murdza, P. Whitney, and D. Flanders. *Chapter 21 Swept Light Sources in Optical Coherence Tomography and Applications*. Springer, Switzerland, 2015 (second edition).

[91] J. Xi, L. Huo, J. Li, and X. Li. Generic real-time uniform k-space sampling method for high-speed swept-source optical coherence tomography. *Optics Express*, 18,9:9511–9517, Mar 2010.

[92] L. Coldren. Monolithic tunable diode lasers. *J. Sel. Top. Quantum Electronics*, 6:988–999, Nov 2000.

[93] D. Choi, R. Yoshimura, and K. Ohbayashi. Tuning of successively scanned two monolithic vernier-tuned lasers and selective data sampling in optical comb swept source optical coherence tomography. *Biomedical Optics Express*, Vol. 4, No. 12:2962–2987, December 2013.

[94] J. Buus, M. Amann, and D. Blumenthal. Widely tunable monolithic laser diodes in tunable laser diodes and related optical sources. *IEEE*, pages 169–219, 2005.

[95] S. Wang. Principles of Distributed Feedback and Distributed Bragg-Reflector Lasers. *IEEE Journal of Quantum Electronics*, 10(4):413–427, 1974.

[96] B. Corbett and D. McDonald. Single longitudinal mode ridge waveguide 1.3 um Fabry-Perot laser by modal perturbation. *Electronics Letters*, (Vol. 31 No. 25), 2010.

[97] H. Carrere, V. Truong, X. Marie, R. Brenot, G. De Valicourt, F. Lelarge, and T. Amand. Large optical bandwidth and polarization insensitive semiconductor optical amplifiers using strained ingaasp quantum wells. *Applied Physics Letters*, 97(12), 2010.

[98] G. Sarlet, G. Morthier, and R. Baets. Control of widely tunable ssg-dbr lasers for dense wavelength division multiplexing. *Lightwave Technology*, 18, No. 8:3032–3048, Aug 2000.

[99] B. James. High speed wavelength tuning of sgdbr lasers for optical coherence tomography applications. Master's thesis, Electrical Engineering Department Faculty of California Polytechnic State University, San Luis Obispo.

[100] J. Engelstaedter, B. Roycroft, F. Peters, and B. Corbett. Heterodyne method for time resolved spectral analysis of fast laser wavelength switching. *IEEE Photonics Technology Letters*, 21, No. 20:1517–1519, Oct 2009.

[101] D. Baney, B. Szafraniec, and A. Motamedi. Coherent optical spectrum analyzer. *IEEE Photonics Technology Letters*, 14, No. 3:355–357, March 2002.

[102] S. R. Chinn, E. A. Swanson, and J. G. Fujimoto. Optical coherence tomography using a frequency-tunable optical source. *Optics Letters*, 22(5):340, 1997.

[103] B. Golubovic, B. E. Bouma, G. J. Tearney, and J. G. Fujimoto. Optical frequency-domain reflectometry using rapid wavelength tuning of a Crˆ4+:forsterite laser. *Optics Letters*, 22(22):1704, 1997.

[104] F. Lexer, C. K. Hitzenberger, A. F. Fercher, and M. Kulhavy. Wavelength-tuning interferometry of intraocular distances. *Applied Optics*, 36(25):6548, 1997.

[105] U. Haberland, V. Blazek, and H. Schmitt. Simultaneous measurements of three-dimensional reflectivity distributions in scattering media based on optical frequency-domain reflectometry. *Optics Letters*, 23(18):1420, 1998.

[106] Hajime Hiratsuka, Eiji Kido, and Takeaki Yoshimura. Simultaneous measurements of three-dimensional reflectivity distributions in scattering media based on optical frequency-domain reflectometry. *Optics Letters*, 23(18):1420, 1998.

[107] Zuyuan He and Kazuo Hotate. Synthesized optical coherence tomography for imaging of scattering objects by use of a stepwise frequency-modulated tunable laser diode. *Optics Letters*, 24(21):1502, 1999.

[108] J. DeBoer, R. Leitgeb, and M. Wojtkowski. Twenty-five years of optical coherence tomography: the paradigm shift in sensitivity and speed provided by fourier domain oct. *Biomedical Optics Express*, Vol. 8, No. 7:3248–3280, July 2017.

[109] Tong Wu, Zhihua Ding, Ling Wang, and Minghui Chen. Spectral phase based k-domain interpolation for uniform sampling in swept-source optical coherence tomography. *Optics Express*, 19(19):18430, 2011.

[110] S H Yun, G J Tearney, J F De Boer, N Iftimia, and B E Bouma. High-speed optical frequency-domain imaging. *Optics Express*, (22):2953–2963.

[111] J. Kalkman. Fourier-Domain Optical Coherence Tomography Signal Analysis and Numerical Modeling. *International Journal of Optics*, 2017, 2017.

[112] U. Sharma and X. Wei. *Fibre optic interferometric devices in Fiber Optic Sensing and Imaging*. Springer Publishing, Berlin, Heidelberg, 2008 (2nd edition).

[113] J. Izatt, M. Choma, and A. Dhalla. *Theory of Optical Coherence Tomography in Optical Coherence Tomography: Technology and Applications*. Springer Publishing, Berlin, Heidelberg, 2008 (2nd edition).

[114] En Bo, Xinyu Liu, Si Chen, Xiaojun Yu, Xianghong Wang, and Linbo Liu. Spectral-domain optical coherence tomography with dual-balanced detection for auto-correlation artifacts reduction. *Optics Express*, 23(21):28050, 2015.

[115] G. Hausler and M. Lindner. Coherence radar and spectral radar - new tools for dermatological diagnosis. *Journal of Biomedical Optics*, Vol. 3, No. 1:21–31, January 1998.

[116] Maciej Wojtkowski, Rainer Leitgeb, Andrzej Kowalczyk, Tomasz Bajraszewski, and Adolf F. Fercher. In vivo human retinal imaging by Fourier domain optical coherence tomography. *Journal of Biomedical Optics*, 7(3):457, 2002.

[117] Xinyu Liu, Mengyuan Ke, Xinwen Yao, Jacqueline Chua, Leopold Schmetterer, and Bingyao Tan. Stable complex conjugate artifact removal in OCT using circularly polarized light as reference. *Optics Letters*, 45(14):3977, 2020.

[118] W. Drexler, Y. Chen, A. Aguirre, B. Povazay, A. Unterhuber, and J. Fujimoto. *Ultrahigh resolution optical coherence tomography in Optical Coherence Tomography: Technology and Applications*. Springer Publishing, Berlin, Heidelberg, 2008 (2nd edition).

[119] C. Dorrer, N. Belabas, J. Likforman, and M. Joffre. Spectral resolution and sampling issues in fourier-transform spectral interferometry. *Optical Society of America*, 17(10):1795–1802, October 2000.

[120] Benjamin R. Biedermann, Wolfgang Wieser, Christoph M. Eigenwillig, Thomas Klein, and Robert Huber. Direct measurement of the instantaneous linewidth of rapidly wavelength-swept lasers. *Optics Letters*, 35(22):3733, 2010.

[121] Adolf Fercher, Christoph Hitzenberger, Markus Sticker, Robert Zawadzki, Boris Karamata, and Theo Lasser. Numerical dispersion compensation for Partial Coherence Interferometry and Optical Coherence Tomography. *Optics Express*, 9(12):610, 2001.

[122] A. F. Fercher, C. K. Hitzenberger, M. Sticker, and R. Zawadzki. Dispersion compensation for optical coherence tomography depth-scan signals by a numerical technique. *Optics Communications*, 204(April):67–74, 2002.

[123] B. Bouma, G. Tearney, S. Boppart, and M. Hee. High-resolution optical coherence tomographic imaging using a mode-locked ti:al2o3 laser source. *Optics letters*, 20(13):1486–1488, July 1995.

[124] G. Tearney, B. Bouma, and J. Fujimoto. High-speed phase- and group-delay scanning with a grating-based phase control delay line. *Optics letters*, 22(23):1811–1813, December 1997.

[125] S. Iyer, Stephane Coen, and F. Vanholsbeeck. Dual-fiber stretcher as a tunable dispersion compensator for an all-fiber optical coherence tomography system. *Optics letters*, 22(23):1811–1813, December 1997.

[126] M. Tsan, I. Hsu, C. Wei, Y. Wang, C. Sun, Y. Kiang, and C. Yang. Dispersion compensation in optical coherence tomography with a prism in a rapid-scanning optical delay line. *Optical and Quantum Electronics*, 37:1199–1212, September 2005.

[127] B. Choi, W. Baumann, E. Swanson, and J. Fujimoto. Extracting and compensating dispersion mismatch in ultrahigh-resolution fourier domain oct imaging of the retina. In *Optics Express*, volume 20, pages 1–12, 2012.

[128] Johannes F. de Boer, Barry Cense, B. Hyle Park, Mark C. Pierce, Guillermo J. Tearney, and Brett E. Bouma. Improved signal-to-noise ratio in spectral-domain compared with time-domain optical coherence tomography. *Optics Letters*, 28(21):2067, 2003.

[129] R. Leitgeb, C. Hitzenberger, and Adolf Fercher. Performance of fourier domain vs time domain optical coherence tomography. *Optics Express*, 11(8):889, 2003.

[130] Michael Choma, Marinko Sarunic, Changhuei Yang, and Joseph Izatt. Sensitivity advantage of swept source and Fourier domain optical coherence tomography. *Optics Express*, 11(18):2183, 2003.

[131] G. Boivin, K. Washington, K. Yang, J. Ward, T. Pretlow, R. Russel, D. Besselsen, V. Godfrey, T. Doetschman, W. Dove, H. Pitot, R. Halberg, S. Itzkowitz, J. Groden, and R. Coffey. Pathology of mouse models of intestinal cancer: consensus report and recommendations. *Gastroenterology*, Vol. 124:762–77, 2003.

[132] P. Treuting, S. Dintzis, and K. Montines. *Comparative anatomy and histology of a mouse, rat and human atlas.* Academic press, Washington, 2018 (2nd edition).

[133] K. Yoshimi A. Irving, M. Hart, T. Parker, L. Clipson, M. Ford, T. Kuramoto, W. Dove, and J. Amos-Landgraf. The utility of apc-mutant rats in modeling human colon cancer. *Disease models and mechanisms*, Vol. 7:1215–25, 2014.

[134] S. Hansen, M. Hart, S. Busi, T. Parker, A. Goerndt, K. Jones, J. Amos-Landgraf, and E. Bryda. Fischer-344 tp53-knockout rats exhibit a high rate of bone and brain neoplasia with frequent metastasis. *Disease models and mechanisms*, Vol. 9:1139–46, 2016.